MASTER OF SCIENCE THESIS

Evaluation of the implementation of a Flettner rotor on a Exploration cruise vessel with respect to the roll motion and rotor-superstructure interaction

---

Author:
M.P.M. STEIJGER

Supervisor:
Prof. Dr. Ir. R. VAN 'T VEER
Prof. Dr. Ir. T. TERWISGA
Ir. R. EGGERS
Ir. A. GROEFSEMA

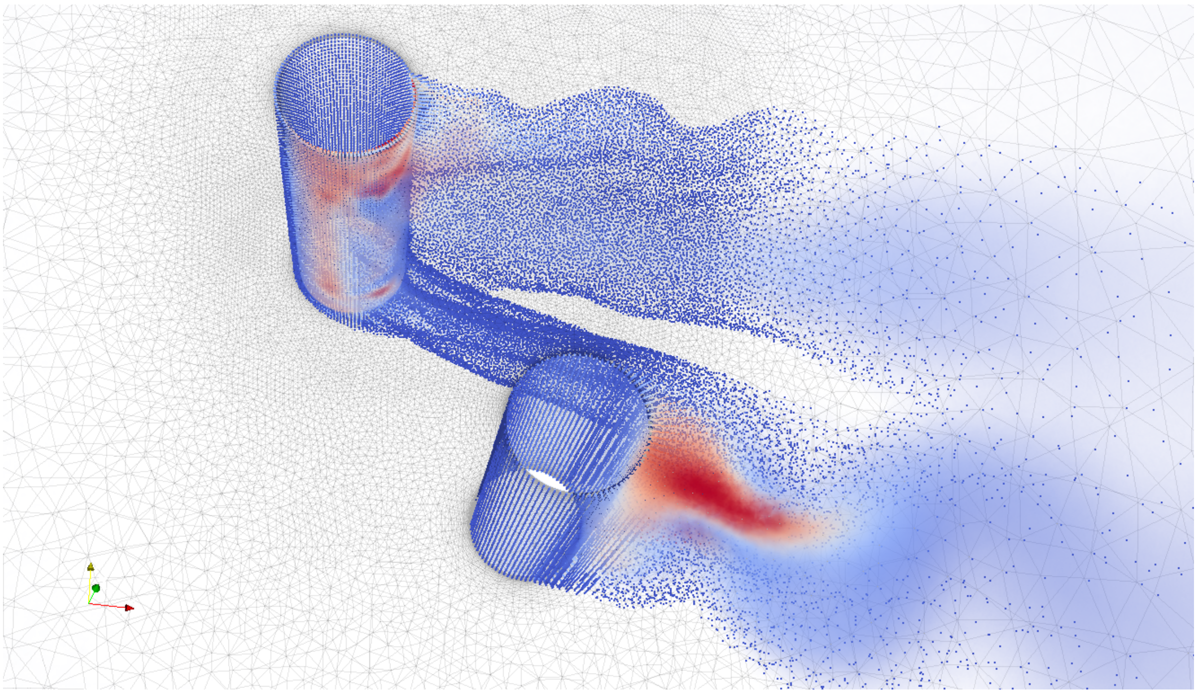

November 11, 2017

Evaluation of the implementation of a Flettner rotor on a Exploration cruise vessel with respect to the roll motion and rotor-superstructure interaction

by

Miranti Petronella Maria Steijger

to obtain the degree of Master of Science
at the Delft University of Technology,
to be defended publicly on Tuesday November 21, 2017 at 2:00 PM.

Student number:	4091779	
Project duration:	November, 2016 – November, 2017	
Thesis committee:	Prof. dr. ir. R. van 't Veer,	TU Delft, supervisor
	Prof. dr. ir. T. Terwisga,	TU Delft
	Ir. R. Eggers,	Marin
	Ir. A. Groefsema,	Ulstein Design and Solutions

This thesis is confidential and cannot be made public until November, 2022.

Preface

Ever since I was young my father always looked in every stream we came across and could answer every curious question I had. That curiosity, together with my mothers persistence, became my stimulation to pursue a masters in hydromechanics.

This thesis could not have been possible without their unconditional support, the stimulating work environment created by amazing colleagues and the helpful feedback given by my exam committee.

Thank you,

M.P.M. Steijger
Rotterdam, November 11, 2017

Vanaf dat ik klein was keek mijn vader al in elk beekje waar we langskwamen en kon altijd al mijn nieuwsgierige vragen beantwoorden. Die nieuwsgierigheid tezamen met mijn moeders doorzettingsvermogen waren mijn drijfveer tot het nastreven van een master in hydromechanica.

Mijn afstuderen was niet mogelijk geweest zonder hun onvoorwaardelijke steun, de stimulerende werkomgeving door geweldige collega's en het behulpzame commentaar van mijn examen commissie.

Bedankt,

M.P.M. Steijger
Rotterdam, November 11, 2017

Contents

List of Figures

List of Tables

Nomenclature

$'$	Differentiation *(superscript)*
$*$	Dimensionless variable *(superscript)*
$*$	Estimation *(superscript)*
$+$	Law-of-the-wall variable *(superscript)*
$-$	Time mean *(superscript)*
δ_G	Error because of the grid
δ_I	Error because of iterations
δ_I	Error because other parameters
δ_{SN}	Error of a numerical simulation
δ_T	Error because of the time step
ϵ	Rate of dissipation
Γ	Circulation $[\frac{m}{s}]$
γ	Angle between V_a and V_s $[deg]$
μ	Incoming wave and wind angle $[deg]$
μ_t	Turbulent viscosity
ν	Kinematic viscosity $[\frac{Ns}{m^2}]$
Ω	Angular velocity $[\frac{rad}{s}]$
ω	Frequency $[\frac{rad}{s}]$
ω_0	Natural frequency $[\frac{rad}{s}]$
ω_w	Wave frequency $[\frac{rad}{s}]$
Φ	Velocity potential
ϕ	Roll angle $[deg]$
ϕ_0	Velocity potential of the incident wave
ϕ_7	Potential because of the disturbance of a wave by a body
ϕ_D	Diffraction potential
ϕ_j	Amplitude radiation potential
ϕ_R	Radiation potential
ϕ_{a_s}	Significant roll angle $[rad]$
ζ_a	Wave amplitude $[m]$
ζ_j	Complex amplitude

A_{44}	Added mass coefficient of roll $[kg \cdot m^2]$
A_{bk}	Area bilge keel $[m^2]$
AR	Aspect ratio
B	Beam $[m]$
B	Stagnation point
B_c	Critical damping $[\frac{kg \cdot m^2}{s}]$
B_{44}	Damping coefficient of roll $[\frac{kg \cdot m^2}{s}]$
B_{bk}	Width bilge keel $[m]$
c	Corrected
C_D	Drag coefficient
C_L	Lift coefficient
C_T	Total coefficient
C_{44}	Restoring coefficient of roll $[\frac{kg \cdot m^2}{s^2}]$
$C_{D_{bk}}$	Drag coefficient bilge keel
CFD	Computational Fluid Dynamics
CoG	Center of gravity
D	Diameter Flettner rotor $[m]$
D	Drag $[N]$
D_e	Diameter end plate $[m]$
e	Error
F	Load $[N]$
FR	Flettner rotor
GCI	Grid Convergence Index
GM	Metacentric height $[m]$
GZ	Initial righting arm $[m]$
H	Wave height $[m]$
h	Grid spacing
h	Height $[m]$
h_0	Height of the rotor $[m]$
H_s	Significant wave height $[m]$
I_{44}	Mass inertia coefficient of roll $[kg \cdot m^2]$
k	Surface roughness
k	Turbulent kinetic energy
k	Wave number

k_t	Thermal diffusivity
kg	Kilograms
kn	Knots
L	Length $[m]$
L	Lift $[N]$
L_{bk}	Length bilge keel $[m]$
LES	Large Eddy Simulation
m	Meters
M_B	Moment vessel rotor $[Nm]$
M_{FR_a}	Amplitude of the oscillating part moment Flettner rotor $[Nm]$
$M_{FR_{constant}}$	Constant part moment Flettner rotor $[Nm]$
$M_{FR_{oscillating}}$	Oscillating part moment Flettner rotor $[Nm]$
M_{FR}	Moment Flettner rotor $[Nm]$
$MCMC$	Markov-chain-Monte-Carlo
N	Number of vertices/nodes
p	Order of convergence
$RANS$	Reynolds Averaged Navier Stokes
RAO	Response Amplitude Operator
Re	Reynolds number
s	Seconds
SR	Spin ratio
SST	Shear Stress Transport
St	Strouhal number
T	Period $[s]$
t	Time $[s]$
T_0	Natural period $[s]$
T_s	Significant period $[s]$
t_{nond}	Nondimensional time
U_∞	Undisturbed flow velocity $[\frac{m}{s}]$
U_{SN}	Numerical uncertainty
$URANS$	Unsteady Reynolds Averaged Navier Stokes
V	Velocity $[\frac{m}{s}]$
v^*	Wall friction velocity $[\frac{m}{s}]$
V_a	Apparent wind velocity $[\frac{m}{s}]$

V_m	Flow velocity because of roll motion $[\frac{m}{s}]$
V_s	Flow velocity because of sailing speed $[\frac{m}{s}]$
V_w	Wind velocity $[\frac{m}{s}]$
V_{w0}	Ambient wind velocity at h_0 $[\frac{m}{s}]$
Y_{wall}	Distance between the boundary and the first vertice $[m]$

Abstract

The implementation of a Flettner rotor on one of its cruise vessels, is seen by Ulstein as a potential contribution to its goal of gaining a vast position in the cruise vessel market segment. A Flettner rotor is implemented on vessels to serve as a complementary propulsion method. They rotate around their vertical axis and thereby induce the Magnus effect[1].

The popularity of cruisetravels has been increasing steadily since 1990. It is expected to continue growing with an annual passenger compound growrate of 6.55% [1]. This thesis supports Ulsteins goal by researching the influence of the implementation of an Flettner rotor on a CX104 Exploration cruise vessel.

The research question of this thesis is divided into two components which will be treated separately. The research question is:

'What is the influence of the implementation of a Flettner rotor on an Exploration Cruise vessel with respect to the roll motion of the vessel and the superstructure-rotor interaction?'

How the implementation influences the roll motion is assessed by determining the external moment excited by the Flettner rotor. The moment excited by the Flettner rotor is evaluated for frequencies around the natural frequency of the vessel, to evaluate its maximum effect. The moment by the Flettner rotor is determined analytically using the Kutta-Joukowski method. The flow around the rotor consists of the sailing velocity, wind velocity and the flow velocity resulting from the roll motion. The first two flow components cause a constant moment by the rotor, independent of time. This constant moment has to be counteracted by the use of, for example, ballast tanks. When the already present tanks in the vessel can not be used for this purpose, the to be installed tank volume is small enough to not cause design issues.

The moment excited by the Flettner rotor resulting from the roll motion fluctuates in time. The moment is in phase with the roll velocity and its amplitude is small compared to the effect of bilge keels. The peak of the RAO of the roll motion of the vessel (including 3% B_c) is decreased by 12.71% when the moment by the Flettner rotor is included. For the natural roll frequency, the significant roll amplitude reduced by 0.27° after the implementation of the Flettner rotor. The chance that the vessel encounters a wave with a frequency equal to the natural frequency of the vessel is however very small. The influence of the moment excited by the rotor caused by the roll motion with the most probable wave frequency is negligible for roll frequencies higher than $\approx 0.4\frac{rad}{s}$. For lower roll frequencies the Flettner rotor assists in the damping of the vessel.

To evaluate the rotor superstructure interaction, three dimensional CFD simulations are conducted, for high Reynolds numbers $\left(10^5\right)$. The domain of the CFD simulations contains a rotor with its height equal to the height of the domain. The rotor will rotate for four spin ratios. For the highest spin ratio a cylinder will be placed in the wake of the rotor, representing a funnel. The influence of the superstructure on the Flettner rotor will be quantified by the change of the flow coefficients of the rotor.

Initially the scope of this thesis did not contain a thorough evaluation of the flow around only the rotating rotor. However the observations during the thesis lead to the finding of a drag crisis, which is considered relevant for the implementation of the Flettner rotor. Therefore the scope is extended. The behavior of the flow around the rotor, with and without superstructure, shows a strong dependence on the stability of the boundary layer. Which is directly dependent on the rotational speed. For spin ratios equal to 0 and 1, the boundary layer remains laminar and the behavior of the flow over the height of the rotor remains constant. For the two higher spin ratios, 2 and 2.5, the boundary layer becomes increasingly turbulent[2]. Resulting in a drag crisis; the drag coefficient will become dependent on the shear stresses close to the surface of the rotor. The wake shows three dimensional effects for the two higher spin ratios; showing the importance of a three dimensional simulation. The higher levels of turbulent kinetic energy are located near the surface of the rotor, decreasing the influence of fluctuating properties of the wake over the rotor height on the drag coefficient. Relevant for the superstructure rotor interaction. The drag coefficient is not influenced by the interaction,

---

[1] The Magnus effect results in a sideways force on a translating and rotating cylinder or sphere [25].

[2] The levels of turbulence in the boundary justifies this assumption taking into account the laminar sub-layer

the lift coefficient however is. The influence on the lift coefficient results from pressure interaction between the wakes of both objects, decreasing the lift coefficient slightly.

An grid independence study shows the independence of the results on the grid refinement. The results fall in the range expected by comparable researches. The performance of an uncertainty assessment, of the closure coefficients of the solver, would give more certainty to the verification of the thesis.

When implementing the rotor it should be considered that the rotor slightly damps the roll motion of the vessel, but only for a sea state with a small chance of occurring. The rotor will cause a constant moment that has to be counteracted.

The superstructure causes the lift coefficient of the rotor to decrease for all spin ratios. When for spin ratios lower than two the superstructure is located closer to the rotor than three times its diameter, interaction will occur with the higher levels of turbulent kinetic energy in the wake of the rotor. This interaction results in fluctuating loads, in direction and magnitude, on the superstructure and a change in produced drag. The direction of the total load of the rotor will slightly change because of that.

Based on the presented calculation methods and conditions, no large changes need to be made to the vessel design because of the implementation of the Flettner rotor with respect to the roll motion and the superstructure interaction.

1

Introduction

During the design process of the Exploration cruise vessel by Ulstein, interest arose in the implementation of a Flettner rotor for stabilization and propulsion purposes. Publications on Flettner rotor usage and interest from schipbuilers are increasing in occurrence, partly because of the high fuel prizes and the increasing awareness of environmental sustainability. One example of recent developments and publications is the article "Fighting the windbreak" by Nelissen, D et. al. [32]. The writers compare among other things the average relative savings of Flettner rotor, wingsail, towing kite and wind turbine for different vessel types. They state that a reduction of 5% to 17% on required propulsion power can be reached [1] for different vessels types when a Flettner rotor is included in the vessel design.

Figure 1.1: Vessel Baden-Baden.

The Flettner rotor is a rotor that is implemented on vessels to serve as a complementary propulsion method. Flettner rotors can have a height between 10-20 meters and a diameter between 2-3 meters. They rotate around their vertical axis and thereby induce the Magnus effect[2]. The Flettner rotor produces a thrust that can be used complementary to a vessels existing propulsion method. A Flettner rotor is considered a "green" propulsion option, because no emissions are produced by the rotor. The first vessel with a Flettner rotor was built in 1920 and was a converted schooner. This vessel was designed by Anton Flettner and built by the German Germenia Werft. Flettner's goal was to replace fabric sails by rigid sails. During that process Flettner heard about Ludwig Prandtl and his research group, who had performed experiments on rotors that achieved higher aerodynamic force coefficients than sails, with equal reference areas. Flettner was the person that saw the advantage in using rotors for vessel propulsion. The vessel that was built by Flettner was renamed to Baden-Baden (Figure 1.1) and made, unfortunately, only one trip across the Atlantic Ocean.

---

[1] On their AIS-recorded voyage profiles.

[2] The Magnus effect results in a sideways force on a translating and rotating cylinder or sphere [25].

1.1. Problem statement

As stated before, this thesis concerns the implementation of a Flettner rotor on a cruise vessel. The two parts of the implementation that will be researched are:

1. The influence of the Flettner rotor on the roll motion
2. The influence of a superstructure located near the rotor on the performance of the Flettner rotor

The influence of the Flettner rotor on the roll motion is researched to see if the Flettner rotor could also be used as a roll-stabilizer. Morisseau presents a list of marine applications of the Magnus effect in his article "Marine applications of magnus effect devices"[29]. Roll stabilizer is one of them and together with the observation that a Flettner rotor can cause an increased heeling moment [34], there was cause to determine the order of magnitude of the external moment caused by the Flettner rotor. The influence of that moment on the RAO of the roll motion will show the stabilizing properties of the Flettner rotor.

The rotor-superstructure interaction is researched since performed researches on tandem cylinders show the potential decrease in drag and lift coefficients compared to a singular cylinder [40] [33]. Small changes in the drag and lift coefficient of the rotor can have large effects on the overall performance of the Flettner rotor. The direction of the total load acting on the rotor, can change together with its magnitude. Furthermore the vortex shedding properties of the rotor can vary. The current body of knowledge on tandem cylinders in a high Re flow is limited, especially concerning 3D simulations. There were no researches found concerning a rotating cylinder with a still standing cylinder in its wake, in a high Re flow. This thesis will therefore add to the body of knowledge regarding simulations of rotating rotors in 3D besides researching the effects of the implementation of a Flettner rotor. Leading to the following main research question of this thesis:

'What is the influence of the implementation of a Flettner rotor on an Exploration Cruise vessel with respect to the roll motion of the vessel and the superstructure-rotor interaction?'

1.2. Research goal

Based on the main research question formulated in the previous section, the goals and purpose of this research will be introduced. The the three goals, which also give an indication of the way in which the research will be set up, are:

1. Compare the RAO of the vessel with and without the moment caused by the implementation of the rotor in order to determine the influence on the roll motion
2. Determine the load, expressed in lift and drag coefficients, excited by a rotating cylinder for different spin ratios using CFD simulations
3. Determine, using a CFD simulations, the interaction between the rotating cylinder and a superstructure by comparing lift and drag coefficients

1.3. Research method

In order to attain the previously described research goals and subsequently to answer the main research question, the used approach will be described in this section. Furthermore, the scope with which this research is performed will be defined.

First the load on the Flettner rotor will be estimated by applying the Kutta-Joukowski theorem on a rotor representing the Flettner rotor. After that estimation the load acting on the Flettner rotor will be determined by using CFD simulations. The Kutta-Joukowski calculation will result in a lift force that acts on the rotating rotor and the CFD simulations will deliver C_D and C_L plots.

With the determined loads acting on the rotor, the RAO of the roll motion of the vessel with and without rotor will be determined. The differences between the RAO's will indicate the influence of the Flettner rotor on the roll stability of the vessel. The effect of the superstructure-rotor interaction will be determined by comparing C_D and C_L coefficients established with simulations of a rotor with and without an superstructure in its wake.

This research will add to the body of knowledge by performing 3D, high Re $\left(\sim 8 \cdot 10^5\right)$ CFD simulations of a rotating rotor with and without a second cylinder in its wake. The flow in the different simulations will be analyzed and related to the expected behavior of the Flettner rotor. The amount of availible simulations of rotating cylinders in this Re range ($8 \cdot 10^5$) is limited. The research on a 3D rotating rotor that most closely resambles this research has been peformed by Zhang at. al. [46]. This research simulates the flow past a rotating cylinder with a finite length. The maximum Re for which simulations are performed is $4 \cdot 10^4$, which is not representative for a Flettner rotor used for maritime propulsion purposes. The research by Karabelas et. al. [24] performs simulations for Re $\sim 5 \cdot 10^5 - 10^6$ but these are however 2D. The necessity of a 3D simulation will be explained in this thesis.

1.4. Content thesis

The thesis will start by presenting the background to the main research question. The background contains the properties and characteristics of the cruise vessel and Flettner rotor together with the environmental conditions set to answer the research question.

After the background a review of the current state of the art concerning Flettner rotor implementation and CFD simulations will be presented. The goal of this chapter is to show the relevance of this thesis and where it adds to the body of knowledge.

The methodology of this thesis, containing the methods used to answer the research question, is divided into two parts. Each presenting the method used to answer the corresponding part of the research question. One of those methods contains the usage of CFD simulations, chapter 6 contains the verification and validation of those simulations.

The chapter "Results" contains the results of the numerical and analytical calculations. They will be described and their relevance will be discussed. This chapter only presents the results, the conclusions drawn from the results are presented in the chapter "Conclusions".

2
Background

In this chapter the properties of the exploration cruise vessel used in this research will be presented. Moreover, the concept behind the Flettner rotor, the way it is implemented on the vessel and its properties will be introduced. Additionally, the relevant environmental conditions will be presented.

2.1. Exploration cruise vessel

The Flettner rotor will be implemented on an Exploration cruise vessel designed by Ulstein [43]. The Exploration cruise vessel is designed with an X-BOW hull line design, improving the on-board comfort, lowering speed loss and reducing spray. The particular vessel that will be used in this research is of the type CX104, its properties are shown in table 2.1.

Length	120	m
Beam	21	m
Depth to main deck	7.5	m
Design drought	5.3	m
Displacement	7269	t
Gross Tonnage	10,000	
PAX	120-130	
CoG_V	10	m
CoG_L	53	m
GM ($T = 5$)	0.756	m
k_{xx}	7.2	m

Table 2.1: Properties of the CX104 Exploration Cruise vessel.

To determine the motion characteristics of the CX104 diffraction, calculations are performed in HydroD. The settings for the HydroD calculations are presented in Appendix A and the calculation methods used by HydroD will be explained in chapter 4. The output produced by HydroD is presented in table 2.2 for one wave frequency. The output of HydroD consists out of coefficients of the equation of roll motion for 59 wave numbers. The determination of these waves is explained in section 2.3.1. The equation of motion of the vessel will be discussed in section 4.2.

I_{44}	$3.7472 \cdot 10^8$	$kg \cdot m^2$
A_{44}	$1.27 \cdot 10^8$	$kg \cdot m^2$
B_{44}	$4.74 \cdot 10^3$	$\frac{kg \cdot m^2}{s}$
Bc_{44}	$3.79 \cdot 10^8$	$\frac{kg \cdot m^2}{s}$
C_{44}	$5.0578 \cdot 10^7$	$\frac{kg \cdot m^2}{s^2}$
ω_0	0.325	$\frac{rad}{s}$

Table 2.2: Data retrieved from the HydroD calculation for ω_0.

At the time of writing, the design process of the CX104 is still in an early stage, for this reason the hull shape available to determine the RAO of roll was coarse. Because of the coarseness of the hull shape the motion coefficients may differ for the final vessel. This can be seen in figure 2.1.

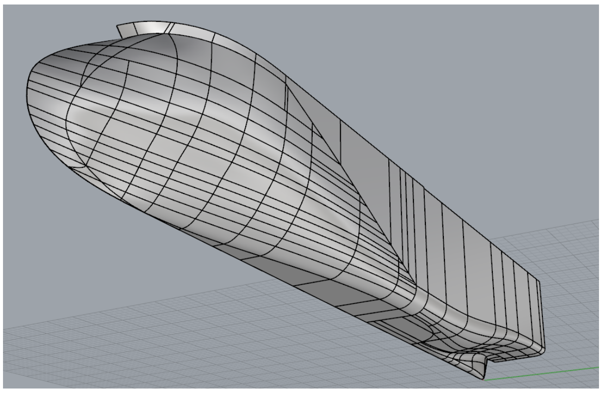

Figure 2.1: Hull of the CX104 presented in Rhino.

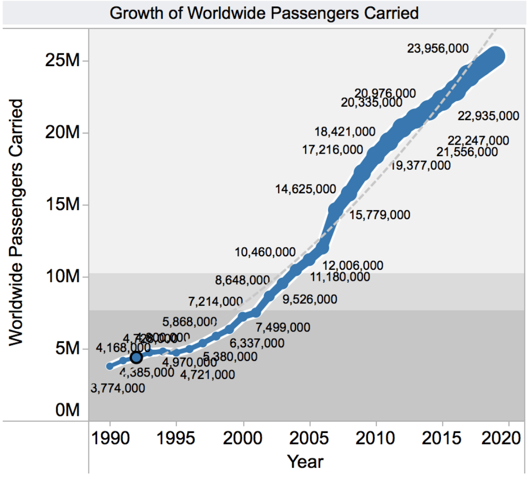

Figure 2.2: The grow of the annual passenger compound for cruise travels [1].

The implementation of a Flettner rotor on its cruise vessel is seen by Ulstein as a potential contribution to its goal of gaining a vast position in the cruise vessel market segment. The popularity of cruise travels has been increasing steadily since 1990. It is expected to continue growing with an annual passenger compound grow rate of 6.55% [1], which can be seen in figure 2.2. Strategies to stimulate this growth have been to increase the capacities of new build ships and to increase the diversification of the vessels. This can be done by increasing the destinations, visit more local ports and to specify the on-board and on-shore activities to the demands of the customers. A new segment in the cruise market are the cruises to the Arctics, for which the CX104 Exploration cruise vessel, designed by Ulstein, can be used.

2.2. Flettner rotor

Here the concept behind the Flettner rotor will be explained together with the reasons for implementing a Flettner rotor on a vessel. The dimensions of the used Flettner rotor will be presented afterwards.

2.2.1. Reasons for implementation

The Flettner rotor is included in vessel designs mainly for the following two reasons:

1. Creation of a green image for the vessel owner
2. Propulsion assistance

The concern for a green image, by cruise companies, partly comes forth out new set environmental regulations, the growing cruise market (section 2.1) and the growing environmental awareness under customers. Speares states in her article "Everything's gone green" in The Navel Architect [38] that the CLIA commissioned a new study highlighting developments resulting in new environmental legislation. A lot of CLIA members are however not waiting on the new legislation's and are implementin innovative ideas and solutions for energy recovery and to reduce the overall environmental impact. These ideas and solutions range from, energy production systems recovering the diesel engine's waste heat to LNG powered vessels. Retrofitting entire cruise vessels for LNG is not viable because of design issues relating to the necessary large quantities of LNG on board. Like with LNG, a cruise vessels needs to be alternated to implement a Flettner rotor. An electric motor is necessary to provide the rotor of enough power to rotate. The motor needs to be located right underneath the rotor. So the original vessel design needs to be redesigned to include a rotor with respect to layout and stability. The positioning of a Flettner rotor on a cruise vessel (2.2.3)is considered not as difficult as retrofitting a vessel for LNG [38].

The magnitude of the potential propulsion force delivered by Flettner rotors has been the subject of several researches, verified real world data is nearly not available. This is because of the high competition between marine companies and that there are only two vessels sailing with a Flettner rotor at the moment. The data of one of the vessels, equipped with a Flettner rotor, and two articles, discussing the efficiency of Flettner rotor implementation, will be discussed to show the relevance of Flettner rotor application.

In 2010 a Flettner rotor powered ship was launched by Enercon, called E-ship. On E-ship four Flettner rotors were placed, resulting in a reduction in fuel consumption of 30% [7]. This percentage is however presented by the owner of the vessel and no particular problems about the Flettner rotor are mentioned. De Marco et. al. [12] have composed two equitation's to predict the performance of Flettner rotors in relation to their spin ratio and aspect ratio (explained on page 29). With those equations they determined that for a 205 meter long, 74983 t product tanker equipped with two Flettner rotors, a thrust reduction was achievable between 0.3 to 0.2 time the resistance of the vessel, at 10 kn and 12 kn respectively. These equations are however estimated based on CFD simulations that are considered less reliable (section 3.1.2).

	Rotor	Wingsail	Towing kite	Wind turbine
Large bulk carrier	17%	18%	5%	2%
Small bulk carrier	5%	5%	9%	1%
Large tanker	9%	9%	3%	1%
Small tanker	5%	5%	9%	1%

Table 2.3: Average relative savings, as a % proportion of the normal power requirement, across the AIS-recorded voyage profiles - higher speed [32].

Nelissen et. al. in their article "Fighting the windbreak" [32] have estimated the market and emission savings potential of wind propulsion technologies for 2030. The types of wind propulsion systems that were modeled are rigid/wing sails, towing kites, Flettner rotors and wind turbines. These wind propulsion systems were modeled on six types of vessels; a 7,200 dwt bulker, 90,000 dwt bulker, 5,400 tanker, 90,000 dwt tanker, 1,000 TEU container and a 5,000 TEU container. The savings per AIS-recorded voyage profile, at higher speeds, are shown in table 2.3. Only the vessels for which Flettner rotor data was available are shown. Important conclusions in the article are that "ships do not need to slow down for at least some wind propulsion systems to become cost efficient"[32]. The relative savings of Flettner rotors and wing sails on the larger ships exceed relative savings on the smaller ships.

2.2.2. Properties

The properties of the Flettner rotor used in this thesis are chosen similar to the properties of the Flettner rotors on the Estraden (2014) shown in the paper by De Marco et al. [12]. The Flettner rotor dimensions of the Estraden are chosen because the properties of the vessel are similar to that of the Exploration cruise vessel. The height of the rotor is decreased by 1 meter to 18 meters. By doing so, the aspect ratio[1] becomes 6, which makes it easier to compare results to other researches. The properties of the Flettner rotor can be seen in table 2.4.

Property	Magnitude	
Height	18	m
Diameter	3	m
Aspect ratio	6	m
End plate	No	
Average RPM	160	
Max RPM	250	

Table 2.4: Flettner rotor properties.

The ratio between the diameter of the end plate (D_e) and the diameter of the rotor (D) varies typically between 2 and 3 [11]. The idea of using an end plate for the Flettner rotor was first suggested by Prandtl [35] and has been thoroughly researched since [42] [2]. The endplates can be seen on the top of the rotors in figure 1.1. The effect of the end plate appears to be strongly dependent on the spin ratio[2]; the magnitude of the

---

[1] Ratio between the height of the rotor and its diameter.

[2] Ratio between the undisturbed flow velocity and the rotational velocity of the rotor.

lift increases and its maximum is reached at higher spin ratios. By not including the end disk the viscous effects of the tip geometry are not included. The tip geometry influences the detachment of the instabilities in the boundary layer. Including the end plate in the determination of the drag and lift coefficients of the Flettner rotor will increase them [12]. The lift will increase until a $\frac{D_e}{D}$ of 3 but after that stays nearly constant [9]. More interesting is the development of the drag coefficient. The drag coefficient can become zero and even negative when $\frac{D_e}{D}$ is increased to 3 and multiple disc are placed on the rotor with an inter-spacing of $0.5D$ [21]. The research question of this thesis is answered without including the end plate. The choice is made to create a 3D CFD simulation, which could not be created with an end plate at the end of the rotor. Three dimensional simulations are created to capture the three dimensional viscous effects in the wake. The total height of the rotor could not be simulated, considering the available computational resources. The simulations are performed for a rotor with infinite length. Because of that assumption a cylinder is simulated which properties can be integrated over the actual height of the rotor. The consequences of assuming an infinite long rotor are discussed on page 35.

2.2.3. Implementation

To position the rotor on the cruise vessel there is first looked at the arrangement of the vessel shown in figure 2.3. The Flettner rotor will deliver a load that might influence the heeling moment of the vessel, therefore it is important that the rotor is located near the center of effort of the lateral surface. Ideally the vessel would have been designed with the Flettner rotor in mind. Typical cruise vessels do not have the stability properties to position a Flettner rotor on their superstructure. The images of vessel (designs) including a Flettner rotor have nearly no superstructure, which is probably for the same stability reasons. As it is not the goal of this thesis to redesign the CX104 vessel so that it is stable with a Flettner rotor, the vessel hull will not be changed. However it should be taken into consideration, that the order of magnitude of the influence of the Flettner rotor on the roll RAO, will change when the design is changed to include the Flettner rotor. In the current design funnel and radar equipment are located on top of the superstructure. The rotor will be located in between both, as can be seen in figure 2.4. Where the location of the Flettner rotor is indicated with a black cylinder. To move a funnel in a vessel design is hard. The radar and the lower placed emergency generator room are easier to relocate. The implementation of multiple slimmer Flettner rotors is also an option. As can be seen in figure 2.3 not a lot of places are ideal to locate a rotor with a 3 meter diameter and a 18 meter height. Beside places to locate the rotor, the height of the vessel needs to be taken into account. Limitations to the air draught are often the case for larger cruise vessels. Sailing underneath bridges to, for example, access city harbors should not be a problem.

Figure 2.3: The CX104 Exploration cruise vessel by Ulstein.

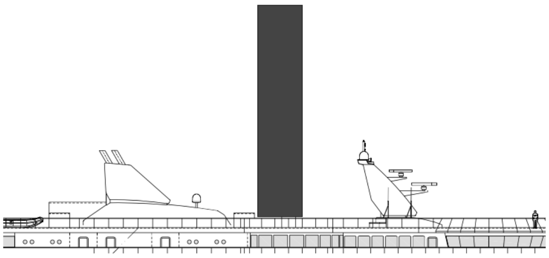

Figure 2.4: Position of the rotor on the CX104.

The main research question states that the influence of the superstructure on the Flettner rotor performance will be evaluated. This comprehends that the funnel will be included in a CFD simulation, where it is represented by a cylinder with similar dimensions. In section 5.3 the set up of the CFD simulations will be presented.

2.3. Research conditions

The goal of this section is to present the conditions for which the main research question will be answered. These conditions are divided into environmental conditions and sailing conditions.

2.3.1. Environmental conditions

In this section the environmental conditions for the calculations to answer the research question will be presented.

Waves

As discussed, only the roll motion of the vessel will be considered. The roll motion will be caused by incoming beam waves. Each evaluated roll motion is excited by a single harmonic wave, with a frequency ranging from $0.1\frac{rad}{s}$ to $1.85\frac{rad}{s}$. A harmonic wave is used because these waves can be superimposed to create a irregular sea [22] [17]. The significant wave height is determined using "Open Ocean Annual Sea State Coddurences from Bales (1983) for the North Atlantic and the North Pacific" (p. 5-51) [22]. The area of the North Atlantic is chosen because is corresponds the most with the operational area of the vessel. The most probable sea state has a significant wave height range of 1.25 - 2.50 meter. The selected significant wave height is 2.5 meter with a probability of occurrence of 28.7%. The choice of the wave height is important because for a linear equation of roll motion, the amplitude of the motion is linear dependent on the wave amplitude. This amplitude has a large contribution to the magnitude of the load excited by the Flettner rotor. The waves that are used as input are presented in appendix B.

Wind

The wind is considered to be fully developed and comes in from the same direction as the waves; 90 degrees from the sailing direction. The cosidered waves are created by the wind and are thus related to each other. The wind speed presented to the most common wave height by Journee [22] is equal to 19 kn (V_{w0}). This wind speed is the ambient wind speed at 19.5 meter (h_0) above the surface, to generate fully developed seas. The magnitude of the wind speed, dependent on the height (h), is given by equation 2.1.

$$V_w = V_{w0} \cdot \left(h/h_0\right)^{\frac{1}{7}} \tag{2.1}$$

An estimation of the relevant height for the wind velocity is the height of the vessel mines the draught. Resulting in a relevant height of 17.3 to $17.3+18 = 35.3$ meter. With 18 meter the height of the rotor. The velocity profile is shown in figure 2.5.

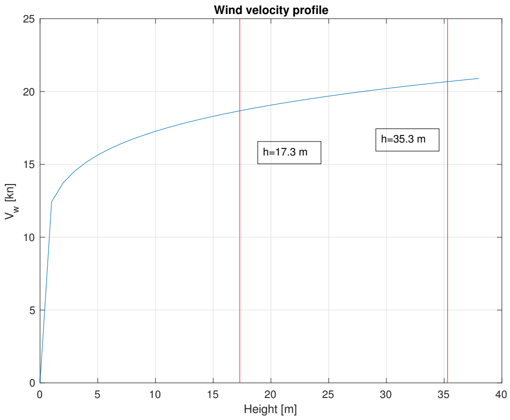

Figure 2.5: Wind profile expressed against the height above sea level.

V_w varies in between $18.5 - 20.5$ kn for the given relevant height, this is a small range. The extra computational effort, for the CFD simulations, to make the wind velocity vary over the height is too large. Thereby will the flow profile change with the wind velocity (Re). The distinction between changes in the flow profile because of a varying wind velocity or because of rotor-superstructure interaction, are hard to separate because of the non-linearity of the flow. The height of the rotor is assumed to be infinite high, so that the results of the CFD simulations can be integrated over the actual height of the Flettner rotor. When a wind profile is used the calculations become height dependent. To keep the calculations, with CFD or to determine the RAO, independent of the height, no velocity profile is used.

In figure 2.6 the directions of the environmental conditions are presented. With in table 2.5 their magnitudes.

Significant wave height	2.5	m
Wave period	8.8	s
Wave length	86	m
Wave number	0.0108	$\frac{rad}{m}$
Incoming angle (μ)	90	degrees
Wind velocity (V_w)	19	kn
Sailing velocity (V_s)	15	kn

Table 2.5: Properties of the environmental conditions.

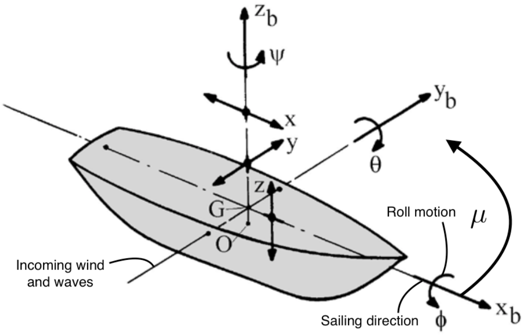

Figure 2.6: Axis definition and environmental conditions.

2.3.2. Sailing conditions

The cruise vessel is sailing with a constant speed of 15 knots. The flow that the rotor will experience while sailing is the apparent wind (V_a). The apparent wind is build up by the sailing velocity, wind velocity and the velocity of the roll motion (V_m). This is shown in figure 2.7.

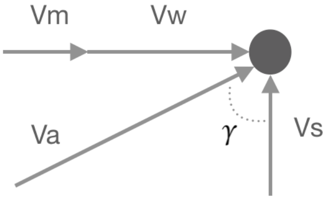

Figure 2.7: Flow velocities experienced by the Flettner rotor.

The angle between the apparent wind and the sailing velocity is denoted by γ.

3

Review state of the art

In this chapter the current state of the art will be evaluated. After which an evaluation will be presented where the current research adds to the body of knowledge and why. First the relevant researches will be summarized. They are divided into four categories:

1. Application of Flettner rotors
2. Rotating cylinder simulations and experimental studies
3. Non-rotating cylinder simulations and experimental studies
4. Tandem cylinder simulations

In the summaries the relevance of the performed research and/or simulations will be discussed for this thesis, together with their reliability. This chapter will also be used for the validation of the research (chapter 6 on page 41).

During this review of the state of the art, special attention will be paid to the CFD simulations of the researches with as goal to evaluate the behavior of the Flettner rotor. Beside that they are necessary for the validation of the simulations performed for this thesis, they can also indicate whether this thesis will add to the body of knowledge on the subject of CFD simulations in three dimensions and for high Reynolds numbers (Re).

3.1. Application of Flettner rotors

In this section researches will be discussed concerning the usage of Flettner rotors; they are not just considered as cylinders for CFD calculations. Evaluations are made on their efficiency, application and specifications.

3.1.1. Re-examination of Flettner-Thom rotors for marine propulsion

The first paper that will be discussed is the paper *"Back to the future? A re-examination of the aerodynamics of Flettner-Thom Rotors for Marine propulsion"* by Craft et. al. [9]. This paper is chosen because of the three dimensional simulations performed for cylinders with and without Thom disks at high Re. Thom disks are disks placed on the Flettner rotor as end-plate or evenly distributed along the rotor height. A recent design for a sailing vessel with distributed Thom disks is shown in figure 3.1.

Figure 3.1: Distributed Thom disks included in a sailing vessel design [28].

The goal set by Craft et. al. is to re-evaluate the potential of the Flettner rotor for low-cost propulsion and to compare their CFD simulations, using URANS and LES, to available experimental data.

They use an unstructured grid throughout the whole domain and perform simulations for two different turbulence models. The two turbulence models are the commonly used $\kappa - \epsilon$ model and a two-component-limit (TCL) stress-transport closure model, developed by Craft et. al. [10]. They use a two dimensional model at a Re of 200 to validate the, coarser then for the three dimensional models, grid.

Craft et. al. conclude that the comparison between simulations including and excluding end-plates show that the influence on the lift coefficient is small. Craft et. al. state that the slight increase in lift does not compensate for the increase in torque acquired by the end-plate. However the influence of the end-plate on the three dimensional flow movements near the end of the cylinder makes the end-plate vital [9].

Craft et. al. emphasize the the necessity of three dimensional simulations to correctly display the flow field around a rotor at a high Re. Turbulent flow does not allow for a two dimensional simulation of the boundary layer and wake development.

Evaluation of the used CFD model

The performed validation of the grid is not considered to be a valid validation. Especially after they explain the difference between high and low Re simulations and two dimensional and three dimensional simulations.

The usage of a domain height of $1D$ is justified in the same way; only cross sections in the xy-plane are presented and discussed. It can not be concluded that a full correlation length [1] of the flow coefficients is reached. In figure 3.2 the blue volumes depict the Q-Criterion (the second invariant of the velocity gradient tensor) equal to -0.5, representing the turbulence behind the cylinder.

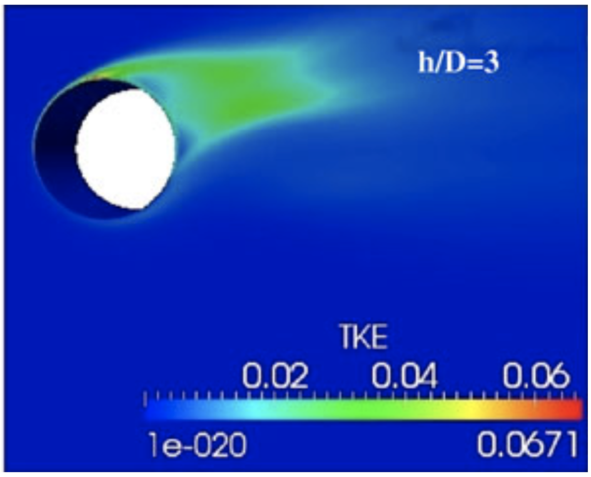

Figure 3.2: Three dimensional flow around a rotating cylincer $SR \sim 2$, with a height of 3D and $Re \sim 1.4 \cdot 10^5$ [9].

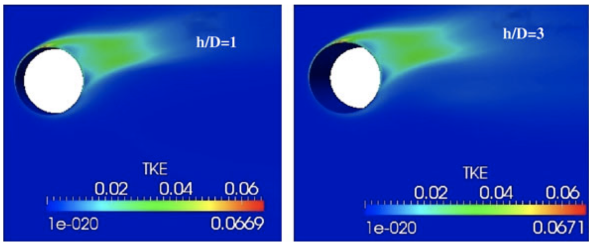

Figure 3.3: Turbulent kinetic energy for two $\frac{h}{D}$ ratios at a Re of $1.4 \cdot 10^5$ and a $SR \sim 2$ [9].

---

[1] Explained on page 35

In figure 3.3 only cross sections in the xy-plane are shown to justify the similarity between wake development at different heights. A more interesting image would have been the cylinder for $Re \sim 8 \cdot 10^5$ for the two different heights. With the figures showing the xz-plane. Then the fluctuations of the vortex formation in two dimensions would haven been captured together with the turbulent boundary layer.

Interesting for this research are the variations of the lift coefficient against the SR. In one figure experiments and simulations with different Re and rotor heights are plotted, shown in figure 3.4. Making the comparison strange especially because this is the Re range in which the drag crisis should occur. The individual values are however interesting and indicate the range the lift coefficient should result in. The height of the rotor is expected to not influence the lift coefficient as much as the drag coefficient, making this data useful.

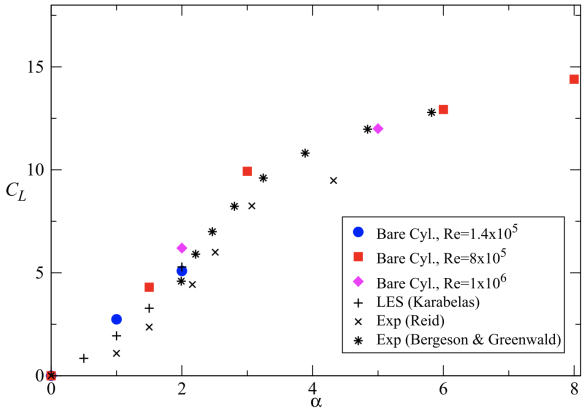

Figure 3.4: Lift coefficient of different simulations and experiments with varing Re [44].

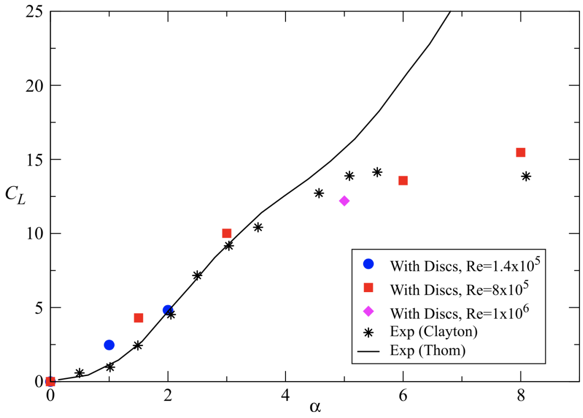

Figure 3.5: Lift coefficient of different simulations and experiments with varing Re including end-plates [9].

Unfortunately Craft et. al. did not present drag coefficient plots.

3.1.2. Flettner rotor concept for marine applications

De Marco et. al. [11] [12] have published two papers concerning the Flettner rotor concept. The first paper was published in 2014 and is called *"Preliminary analysis for Marine Application of Flettner rotors"*, this paper is a preliminary analysis for the final article *"Flettner rotor Concept for Marine Applications; A Systematic Study"*. The research by De Marco et. al. is more applied to the actual implementation and usage of a Flettner rotor than the research by Craft et. al.. De Marco et. al. performed simulations to study the efficiency of the Flettner rotor, and conclude with a test case where a Flettner rotor is implemented on a 205 meter long product tanker.

They expressed their results in different parameters, to show their sensitivity thereon. Form these results it was concluded that the lift production and aerodynamic efficiency of the Flettner rotor is higher than the values given by wings of comparable aspect ratio. The potential of the Flettner rotor as a marine propulsion device was concluded to be maximum 30% of the ship resistance in the range of operational speeds. The evaluation of the aerodynamic efficiency is stated to be less significant than the evaluation of each force component; the drag gives a positive contribution to the trust in a wide range of apparent wind angles.

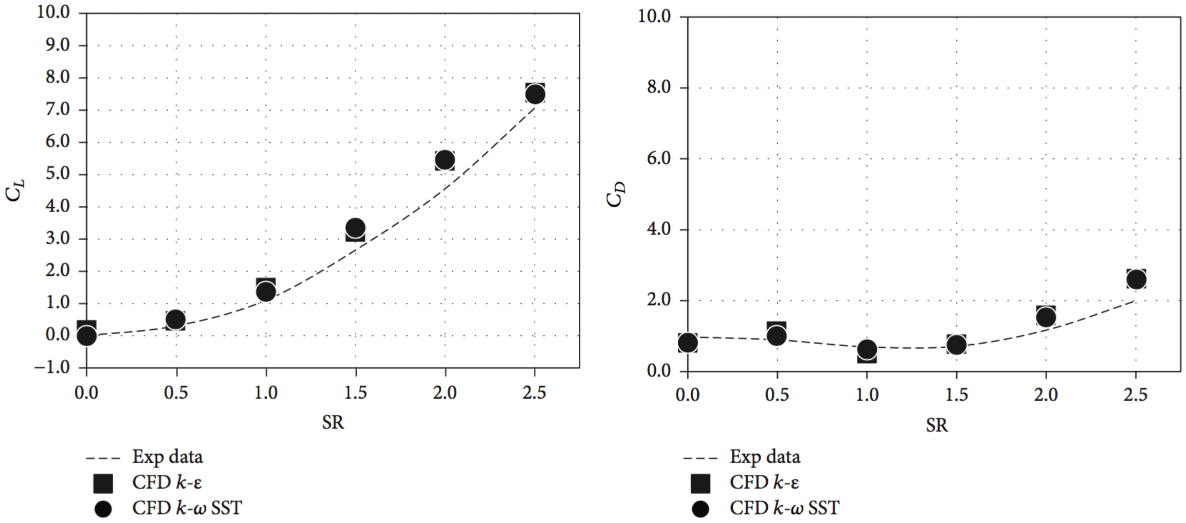

Figure 3.6: Experimental data, and two turbulence models [12].

The CFD simulations are computed using URANS and two turbulence models which are compared. The simulations are performed in three dimensions for different AR and SR. The Re for which the research is performed was not presented by De Marco et. al.. An numerical uncertainty assessment was performed concluding that the results are reliable for $SR < 1.5$. For all the simulations the comparison error (E) was much larger then the numerical uncertainty. The numerical uncertainty they determined arose from uncertainties caused by the grid, iterations, time step and other parameters.

Evaluation of the used CFD model

De Marco et. al. have mirrored the domain in the x-axis. In the uncertainty assessment the grid refinement ratio is not presented. The mirroring of the domain should be taken into account by evaluating the flow coefficients. Depending on the rotational direction of the rotor the flow coefficients will be higher or lower than a simulation considering the whole domain.

Interesting is the comparison of the two turbulence models. It shows a slight difference in results around the SR where the drag crisis is expected. The Re is not found for the simulations so this observation can not be made with great certainty. Very informative is figure 3.7, showing the influence of SR, AR and end-plate inclusiveness or not. The influence of the SR increases when the AR increases. The effect of the end-plate decreases the effect of the SR on the flow coefficients.

Figure 3.6 shows the flow coefficients determined by De Marco et. al. for the exact same SR range used in this thesis ($AR = 6$).

3.1.3. Flettner rotor in efficient ship design

Another paper that was consulted about the implementation of Flettner rotors in ship design is the paper *"The use of Flettner rotors in efficient ship design"* by Pearson [34]. This paper is not discussed in depth in this research because it captures more the design aspects of the Flettner rotor. However is does discuss the effect of the Flettner rotor on the vessel motions shortly. Its prediction is that the influence of the Flettner rotor on the heel angle is small.

Evaluation of the used CFD model

That the error (E) was much larger then the numerical uncertainty indicates the necessity of verification, of the simulations performed by de Marco et. al. and for the current thesis. In the uncertainty determination they did not include that the domain is mirrored in the x-axis. This makes it difficult to compare the results to the current research with the current thesis and causes the results to deviate of the truth; the flow around a rotating rotor is highly asymmetrical.

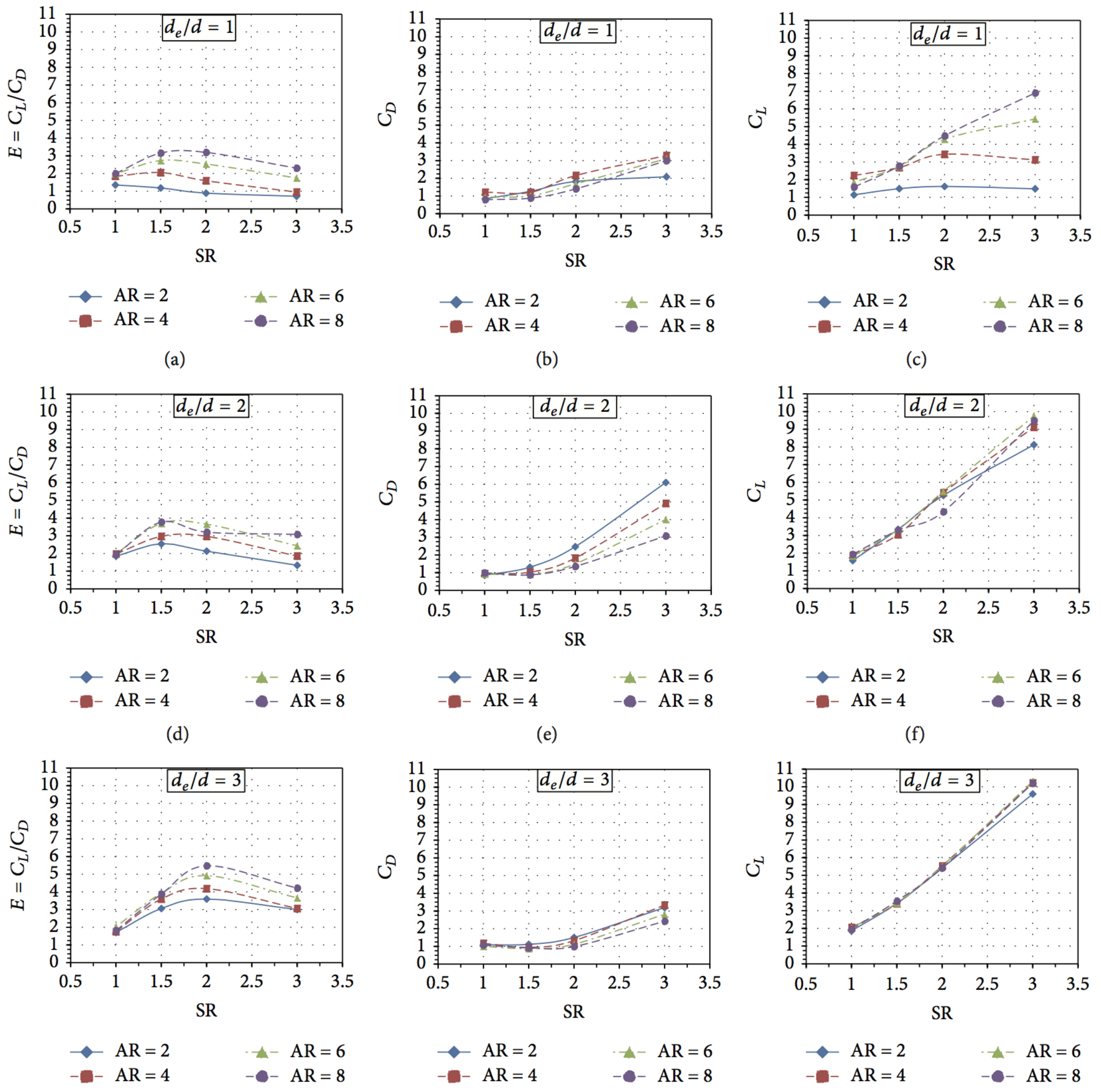

(a) (b) (c)

(d) (e) (f)

Figure 3.7: Experimental data, and two turbulence models [12].

3.2. Rotating cylinder

In this section a research will be discussed that simulates a rotating cylinder with CFD. This paper is selected based on Re, SR, dimensions of the domain and the simulation methods. Papers on rotating cylinders in a high Re flow are hard to find. The following paper is considered to be of high quality and will be used to validate the CFD simulations in chapter 6.

3.2.1. High Re turbulent flow past a rotating cylinder

The article by Karabelas et. al., titled *"High Re turbulent flow past a rotating cylinder"*, is often referred to in other researches and is consulted multiple times during this thesis.

Karabelas et. al. have investigated a high Re flow around a rotating cylinder using two dimensional CFD simulations. They have used a modified $\kappa - \epsilon$ turbulence model. The performed simulations are for a SR range between 2 and 8 and Re between $5 \cdot 10^5$ and $5 \cdot 10^6$. Other numerical data and experimental results were used to verify and validate the simulations. At high SR the loads acting on the rotor appeared to be more stable and have suppressed vortex shedding characteristics. The article contains an discussion on existing literature that was very valuable in obtaining an image of the, at that moment, available knowledge.

Evaluation of the used CFD model

Karabelas et. al. states that two dimensional modeling is accurate to describe the three dimensional behavior of the flow behind the Flettner rotor. They come back to that statement by stating that the loads will differ only a small amount by using a three dimensional simulation compared to a two dimensional one. Later in the article, while comparing their research to thee dimensional experiments, they conclude that the drag coefficient is over predicted by their two dimensional simulations. This conclusion is based on simulations performed for a Re of $6 \cdot 10^4$.

Karabelas et. al. discuss a URANS simulation for a $SR \sim 2$ and a Re of $5 \cdot 10^5$. Their goal is to show that the flow around the cylinder is stable and form there on in the research the usage of RANS simulations are justified. The results of the simulation are shown in figure 3.8. The flow appears to become steady. The steadiness of the flow show that there are no more instabilities in the wake for a $SR \sim 2$ and a Re of $5 \cdot 10^5$ and higher values for both parameters. This is something that can be checked with the current thesis, even though the current thesis is performed for a Re of $8 \cdot 10^5$. Karabelas et. al. compare visual images of simulations for increasing SR and different Re. Streamlines are presented in the xy-plane, only the visualizations that are considered relevant for this thesis are shown in figure 5.4 on page 30. Figure 5.4 shows the change of stagnation points that is also discussed in appendix C. Karabelas et. al. conclude that the flow patterns are all the same for $SR > 4$ in turbulent flow. In a laminar flow the stagnation point is continuing to shift to the outer region, shown by L in figure 3.9. Figure 3.9 shows a rotating cylinder with a SR of 8 and a Re equal to 200. This image is made using RANS whereby the time dependent flow effects are harder to evaluate. The interaction between the flow and the cylinder is induced by a no-slip condition on the cylinder surface. They have made no observations on how they included the laminar sub-layer in the observations of turbulent or laminar boundary layers.

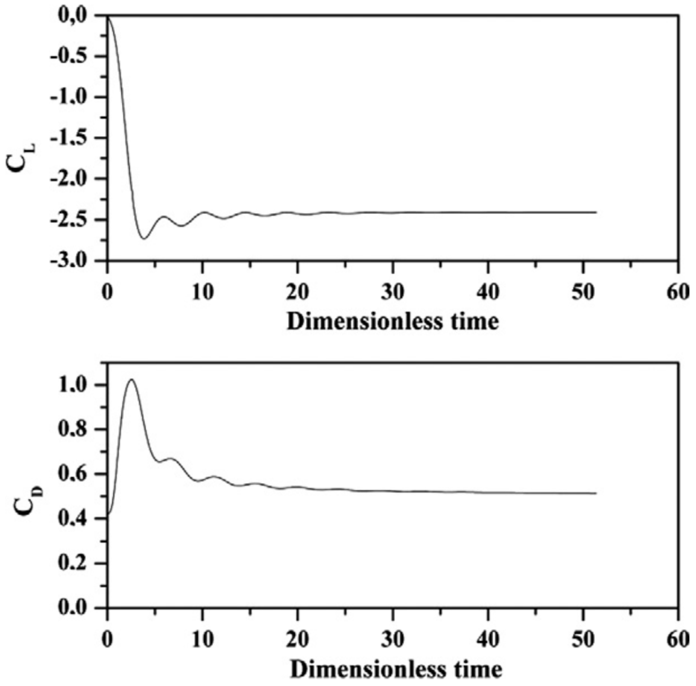

Figure 3.8: URANS simulation for a flow past a rotating cylinder for $SR \sim 2$ and a Re of $5 \cdot 10^5$ [24].

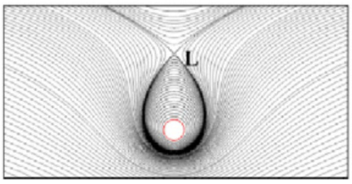

Figure 3.9: RANS simulation for a flow past a rotating cylinder for a $SR \sim 8$ and a Re of 200 [24].

3.3. Non-rotating cylinder

Non-rotating cylinder simulations are not as interesting as rotating cylinder simulations for this research. Still, four researches were used during this thesis. Only the article by Singh et. al. [37] will be discussed in depth because they elaborate on the flow phenomena for a large range of Re. That information is very useful for the evaluation of the flow around the rotors simulated during this thesis.

The content of the other three researches will briefly be discussed at the and of this section.

Singh and Mittal [37] researched the shear layer instability and drag crisis by simulating a cylinder in a Re range of 100 to 10^7. They used URANS to capture the instabilities in two dimensional simulations. All the stages of flow development around a cylinder are discussed for the considered Re range, with an in dept description of the flow patterns and their origins. The research contains very clear visualizations of the drag crisis and the (unstable or detached) shear layer. This article explains the behavior of the drag based on the Re of the flow and the influence of turbulence, at a wide range of Re. For example, the vortex street is displayed and discussed for different Re; figure 3.10.

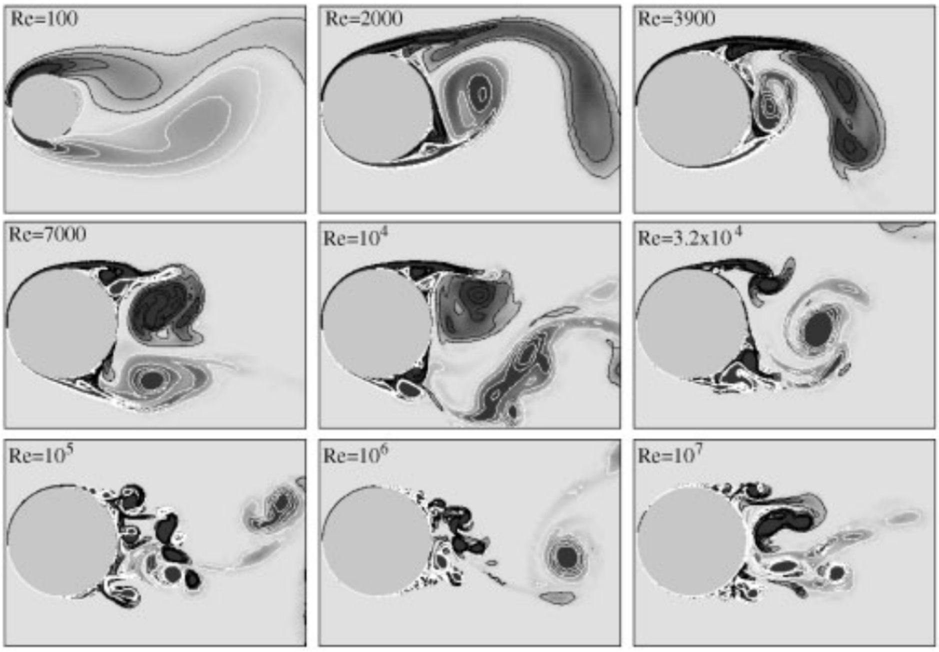

Figure 3.10: Vortex street for different Re[37].

This research combines other researches to explain in depth what occurs in the flow behind a cylinder for different Re. That information is important when theoretical simulations/models are to be used in practice. Phenomena can then be used or avoided when desirable. *Singh et. al. state that beyond a Re* ~ 200 *two dimensional simulations are unable to predict the correct value of a drag coefficient.* Using two dimensional simulations the flow phenomena are not captured precisely but the Re value for which the drag crisis will occur can be estimated accurately [37]. When the Re becomes larger than 2000 the instability of the shear layer starts to occur. Setting requirements for the grid near an object to resolve the boundary layer and its interactions with the shear layer to capture these instabilities[37].

The other three papers were by Breuer [4], Catalano et. al. [5] and Moussaed et. al. [31]. The paper by Breuer has as goal to evaluate the applicability of LES for high Re flows. He investigated the influence of subgrid scale models and grid resolution on the quality of the predicted results. By describing the influence of the subgrid scale models Breuer explains the flow principles around the cylinder thoroughly, which is interesting for evaluating the results of the simulations performed during this thesis.

Catalano et. al. have performed simulations in two dimensions of a cylinder in a high Re flow. They show the relevance of LES compared to RANS simulations. They evaluate the flow based on the boundary layer separation and the reduced drag coefficient. The Re dependence of the flow is not captured. Karabelas et. al. [24] did capture a slight Re dependence of the results for the same order of Re. But they considered it negligible for $SR > 4$.

The goal of the last article, by Moussaed et. al. [31], is comparable to that of Catalano et. al. and Breuer. RANS and variational-multiscale LES models are compared as methods to simulate a two dimensional cylinder in a high Re flow.

3.4. Tandem cylinders

In this section an article on tandem cylinder simulations is discussed to serve as a reference for the rotor-superstructure simulation, which consists out of two cylinders. Only one article was found on three dimensional simulations of two tandem cylinders for a $Re \sim 10^2 - 10^3$.

The article by Papaioannou et. al. [33] called *"Thee dimensionality effects in flow around two tandem cylinders"* discusses simulations of a laminar and early turbulent flow, around two tandem cylinders. They state that the three dimensional results differ a lot from two dimensional results for increasing Re. Reattachment of the shear layer ceases for two dimensional simulations, for smaller distances between the cylinders than in tree dimensional simulations. A spacing factor is discussed for which wake stabilization occurs. This factor is irrelevant for the current research because of the Re range difference. However the occurrence of wake stabilization by a tandem positioning of cylinders is of interest.

3.5. State of the art current research

The existing researches on the Flettner rotor, contain an in depth evaluation of the usage of Thom disks and the efficiency of the Flettner rotor. To that body of knowledge this research will not add. However, the implementation of the rotor is only discussed once by Pearson [34]. Pearson uses linear estimations of the load excited by the rotor and does not include the effects of the roll motion. Showing the added value of this thesis compared to Pearson's and the corresponding body of knowledge.

The simulations created during this thesis are run in a three dimensional domain. To this domain no alternations are made to reduce the necessary computational resources. Therefore they capture the whole three dimensional effect on the flow behind the (rotating) rotor. No other research, discussed in this thesis, complies to the same conditions. A flow evaluation, like the one given by Singh and Mittal[37], in combination with those three dimensional simulations, will deliver insight in the flow around the rotor that is not been presented before.

This research does not include wall laws or compares different turbulence models while the aim of this thesis is to evaluate the implementation of a Flettner rotor. Other researches have presented in depth material on those subjects..

4

Methodology; Evaluating the effect on roll motion by analytically determining RAO's

This chapter contains the methodology used to compute the Response Amplitude Operators (RAO's) of the roll motion of the vessel with and without an implemented Flettner rotor. The goal of this chapter is to show how the first part of the research question is answered; *"What is the influence of the implementation of a Flettner rotor on an Exploration cruise vessel with respect to the roll motion?"*.

The RAO's for the roll motion will be determined for three conditions which are presented in figure 4.1. The RAO of the Exploration cruise vessel will be compared to the RAO of the vessel including an Flettner rotor to answer the research question, as will be discussed in the results on page 51. The bilge keels are included in this chapter to show the magnitude of the effect of the Flettner rotors on the RAO of the vessel.

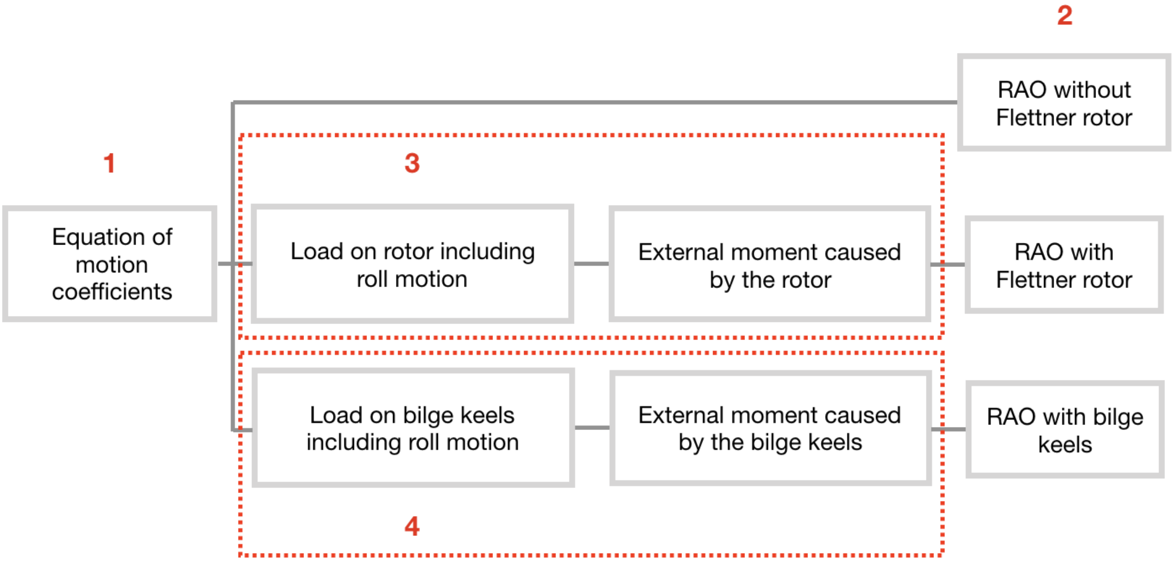

Figure 4.1: Steps undertaken to determine the RAO of the Exploration cruise vessel with and without Flettner rotor/bilge keels.

First the equation of motion will be discussed including the alternations made to the coefficients to obtain the different RAO's. When the equation of motion is clear the loads excited by the Flettner rotor and bilge keels will be explained.

The RAO's that result out of the steps explained in this chapter will be discussed in chapter 7.

4.1. Description of vessel motions

The research question of this thesis concerns the roll motion of the vessel and the influence of the Flettner rotor thereon. The roll motion is chosen because, together with pitch, it causes the most discomfort to passengers related to the inclination of the vessel [13]. One major discomfort to passenger is seasickness. Seasickness is caused by a sensory conflict induced by the vertical acceleration of the ship. The pitch motion is more stable because the position of the center of effort has a larger arm in x-direction. Therefore the influence of the Flettner rotor is considered the largest in roll direction. The roll motion will be represented by the uncoupled roll motion equation. In appendix E the linear and nonlinear equations of motions are explained.

4.2. Equation of motion

The first step, as shown in figure 4.1, is to determine the coefficients of the equation of motion. HydroD is used to determine these coefficients. HydroD determines the influence of harmonic waves on rigid bodies using potential theory applied to a panel model. A wave with the properties as described in section 2.3.1 together with the hull shape shown in figure 2.1 served as input.

To show the methodology of HydroD, first the potential theory will be discussed, where after the determination the coefficients of the equation of motion.

4.2.1. Potential theory

Potential theory uses the assumption of potential flow, where the flow velocity is defined by the gradient of the flow potential (Φ). The gradient of the flow potential satisfies the Laplace equation in the fluid domain; $\nabla^2\Phi = 0$.

HydroD determines the equation of motion for an harmonic wave system. The harmonic time dependence is used as well by defining the velocity potential; $\Phi = Re\left(\phi e^{i\omega t}\right)$. The velocity potential of the incident wave is given by equation 4.1.

$$\phi_0 = \frac{igA}{\omega}\frac{\cosh\left(kz+H\right)}{\cosh\left(kH\right)}e^{-k(x\cos\mu+u\sin\mu)} \tag{4.1}$$

Here k is the real root of the dispersion equation.

To explain how potential theory a wave describes its components are briefly explained. Because of the linearity of the equation the velocity potential can be decomposed into a radiation and a diffraction component:

$$\phi = \phi_R + \phi_D \tag{4.2}$$

$$\phi + R = i\omega\Sigma_{j=1,6}\xi_j\phi_j \tag{4.3}$$

$$\phi_R = \phi_0 + \phi_7 \tag{4.4}$$

ξ_j represents the complex amplitudes of the body oscillatory motion in its six rigid-body degrees of freedom [14], and $\phi_j$is the unit amplitude radiation potential that corresponds to ξ_j. The disturbance of the incident wave by the body is represented by ϕ_7.

4.2.2. Equation of motion coefficients

HydroD uses the linear equation of motion to evaluate the motion of the cruise vessel excited by an harmonic wave. The linear equation of motion is shown in equation 4.5.

$$I_{44}\ddot{\phi} + B_{44}\dot{\phi} + C_{44}\phi = M\left(\phi\right) \tag{4.5}$$

The inertia coefficient(I_{44}), damping coefficient(B_{44}) and restoring coefficient(C_{44}) are all independent of the roll angle. No external conditions are considered beside the exciting waves and wind.

A general description of the coefficients of the motion equation will be presented in the next sections. Together with how they are determined with HydroD.

Inertia coefficient

The inertia coefficient consists out of the mass inertia of the vessel and the added mass $\left(A_{44}\right)$. The mass inertia is composed by specifying the CoG and the radii of gyration of the vessel together with the total mass. The added mass is determined using potential theory.

Damping coefficient

HydroD determines the roll damping coefficient which includes the following hydrodynamic effects:

1. Potential damping from surface wave radiation
2. Linearised viscous damping from skin-friction of the hull

Using linear theory the potential damping effect is included in the radiation potentials. The linearised viscous roll damping effects from eddy-making, due to the naked hull, is computed based on empirical data [14]. These viscous effects are nonlinear from origin but are linearized so that they can be included in the harmonic equation of motion[1]. The potential damping and skin friction contributions are derived using a strip model which is generated from the panel model.

In HydroD the quadratic roll damping is stochasticly linearised. The damping is considered to be linear for the harmonic equation of motion, and thus independent of the considered sea state. The quadratic drag is represented in the following form:

$$F_{44} = -B_{44}^{(2)}|\dot{\phi}_4|\dot{\phi}_4 \tag{4.6}$$

Where $B_{44}^{(2)}$ is the quadratic damping coefficient. When $B_{44}^{(2)}$ is substituted by $B_{44}^{(1)}$, a linear damping coefficient, the estimated error should be assessed. The error random process due to linearization is given in equation 4.7.

$$e(t) = B_{44}^{(2)}|\dot{\phi}_4|\dot{\phi}_4 - B_{44}^{(1)}\dot{\phi}_4 \tag{4.7}$$

In the frequency range, for which the damping coefficient will determined, an estimation can be made for each ϕ. When equation 4.7 is rewritten for $B_{44}^{(1)}$, $\dot{\eta_4}^2$ can be expressed in its expected value. As shown in equation 4.8.

$$B_{44}^{(1)} = \frac{B_{44}^{(2)} E\left(|\dot{\phi}_4|^3\right)}{E^2\left(\dot{\phi_4}^2\right)} \tag{4.8}$$

The criteria for each iteration is that the expectation value of the squared error has a minimum, as shown in equation 4.8. $\dot{\eta}_4$ is assumed to be normally distributed and half of that distribution is presented in equation 4.9 for $|\dot{\eta}_4|$.

$$E\left(|\dot{\eta}_4|^3\right) = \frac{\sqrt{8}}{\pi}\sigma_{\dot{\eta}_4}^3 \tag{4.9}$$

With σ the standard deviation; $E\left(\dot{\eta_4}^2\right) = \sigma_{\dot{\eta}_4}$. Equation 4.9 together with the formulation of the standard deviation, can be substituted in equation 4.8. Resulting in the stochastic linearization of the quadratic damping coefficient (equation 4.10).

$$B_{44}^{(1)} = \frac{B_{44}^{(2)}\frac{\sqrt{8}}{\pi}\sigma_{\dot{\eta}_4}^3}{\sigma_{\dot{\eta}_4}^2} = \frac{\sqrt{8}}{\pi}\sigma_{\dot{\eta}_4}B_{44}^{(2)} \tag{4.10}$$

Restoring coefficient

The restoring coefficient determined by HydroD is also linear and determined for small roll angles. From the model geometry an initial transverse metacentre height ($\overline{GM_i}$) can be determined. The initial righting arm ($\overline{GZ_i}$) can then be determined using $\overline{GZ_i} = \overline{GM_{Ti}} \cdot \phi_4$.

The determined coefficients of the equation of motion are presented in table 2.2 on page 7.

4.3. Load on the rotor

The load on the rotating Flettner rotor is estimated using the Kutta-Joukowski theorem. The Kutta-Joukowski theorem only considers the fluctuation of the local air pressure close to the boundary layer and neglects all viscous influences. The Kutta-Joukowski theorem is shown in equation 4.11.

$$L = \rho\left(\Gamma \times U_\infty\right) \tag{4.11}$$

---

[1] The relation between the empirical data and the roll velocity is linearized

Where the circulation (Γ) is given by equation 4.12. The determination of Γ here uses the velocity of the outer fiber of the rotor. The lift caused by the rotation of the rotor is not a potential system as described here, there are viscous effects needed to create the pressure difference out of which the lift is derived. Γ also could and/or should include viscous effects. They are not included here because the Kutta-Joukowski theorem is used as an method to estimate the lift load.

$$\Gamma = \oint V ds = 2\pi \Omega R^2 \tag{4.12}$$

Ω stands for the angular velocity of the rotor and R for the radius. The lift is then represented by equation 4.13.

$$L = 2\pi \rho U_\infty \Omega R^2 \tag{4.13}$$

The lift caused by the pressure distribution is determined in the xy-plane and needs to be integrated over the height of the rotor. The height of the rotor is divided into parts of $1m$ whereon the lift will be determined.

The velocity used to determine the lift acting on one height segment is determined in the middle of each height segment. The flow velocity around the rotor consists out of the components shown in figure 2.7, the flow velocity because of the wind, the sailing speed and the motion of the vessel. Together they are expressed in the apparent wind. In equation 4.11 the flow velocity U_∞ is replaced for the apparent wind V_a.

Moment around the vertical center of gravity

The influence of the Flettner rotor on the roll motion is evaluated in this thesis, therefore only the load on the rotor in the y-direction is of interest (figure 2.6). The load on the rotor determined by the Kutta-Joukowski theorem is only the lift component, the drag component corresponding to the determined lift is calculated using the ratio between both presented by De Marco et. al. [11][2]. The ratio is kept constant over the height of the rotor because of the slight change in SR over the rotor height. With the drag and lift determined, for each height segment of the rotor, the total load acting on that height segment can be determined. The moment caused by the Flettner rotor in roll direction is calculated by determining the y-component, of the total load acting on the height segment, and multiplying that load by the distance between the center of the height segment and the CoG_v of the vessel.

4.4. RAO

An Response Amplitude Operator (RAO) shows the ratio between the amplitude of the, here, roll motion and the amplitude of the harmonic wave $\frac{\phi_a}{\zeta_a}$ expressed in their rotational frequency. The roll motion of the cruise vessel is evaluated for 59 wave numbers (k), shown in appendix B. The RAO of the vessel will be plotted against the RAO's including:

- Damping moment caused by two bilge keels
- Damping moment caused by one Flettner rotor

This is done to quantify the influence of the implementation of the Flettner rotor on the RAO. The moments caused by the Flettner rotor and the bilge keels will be included in the equation of roll motion, and thus the RAO, as external moments. Typically defined on the right hand side; $M\left(\dot{\phi}\right)$[3]. They are both considered damping terms and thus dependent on the angular velocity of the roll motion.

The RAO will be determined using equation 4.14.

$$\frac{\phi_a}{\zeta_a} = e^{kT} \sqrt{\frac{\left(C_{44} - A_{44}\omega^2\right)^2 + \left(B_{44}\omega\right)^2}{\left(C_{44} - I_{44}\omega^2\right)^2 + \left(B_{44}\omega\right)^2}} \tag{4.14}$$

The mass of the rotor and its influence on the inertia term in equation 4.5 $\left(I_{44}\right)$ of the vessel is assumed to be small enough to be neglected.

---

[2] De Marco et. al. present in the paper "*Flettner Rotor Concept for Marine Applications: A Systematic Study*" for a $SR \sim 2.5$ a ratio between the lift and drag of 2.5.

[3] Following from equation 4.13 the load and thus moment excited by the Flettner rotor are dependent on V_a

4.5. Bilge keel damping

As a method to evaluate the damping of the Flettner rotor its damping properties can be compared with the damping caused by a set of bilge keels. The moment caused by one bilge keel is estimated using the Morison equation where the inertia component is neglected; $M_{bk}\left(\dot{\phi}\right) = \frac{1}{2}\rho C_d A\dot{\phi}|\dot{\phi}|$. The estimated position and dimensions of a bilge keel are shown in figure 4.2.

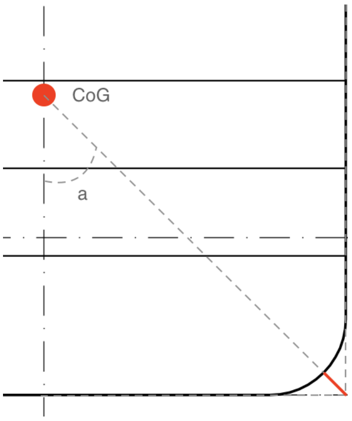

Figure 4.2: Estimated position and dimensions of a bilge keel.

The angle (a) of the bilge keel is estimated in equation 4.15.

$$\tan^{-1}\left(\frac{\frac{Beam}{2}}{CoG_v}\right) = \frac{10.5}{10} \approx 45° \tag{4.15}$$

The estimated dimensions of the bilge keel are presented in table 4.1.

Length (L_{bk})	$\frac{1}{2}L = 52$	m
Width (B_{bk})	$\sqrt{\left(\frac{1}{32}B\right)^2 + \left(\frac{1}{16}CoG_v\right)^2} \approx 0.9062$	m
Area (A_{bk})	151	m^2

Table 4.1: Estimated bilge keel dimensions.

The drag coefficient of the bilge keel Cd_{bk} is estimated using the method proposed by Ikeda et. al. [20] shown in equation 4.16.

$$\begin{aligned} Cd_{bk} &= \frac{45}{KC\,f} + 2.4 \\ f &= 1 + 0.3\exp\left(-160\left(1-\sigma_A\right)\right) \end{aligned} \tag{4.16}$$

Where σ_A is the sectional area coefficient.

5

Methodology; Evaluating superstructure-rotor interaction using CFD

The aim of this chapter is to show how the second part of the research question; *"What is the influence of the implementation of an Flettner rotor on a Exploration cruise vessel with respect to the superstructure-rotor interaction?"* is answered. To answer that part of the research question Computational Fluid Dynamic (CFD) simulations are performed to determine the load excited by the rotor for different spin ratio's (SR's) and the interaction between the superstructure and the Flettner rotor. A domain is made including a rotor that will rotate. That same domain is remade but adjusted so that it contains a cylinder, representing the superstructure. For both domains simulations are run with the same solver settings.

The undertaken steps are shown in figure 5.1.

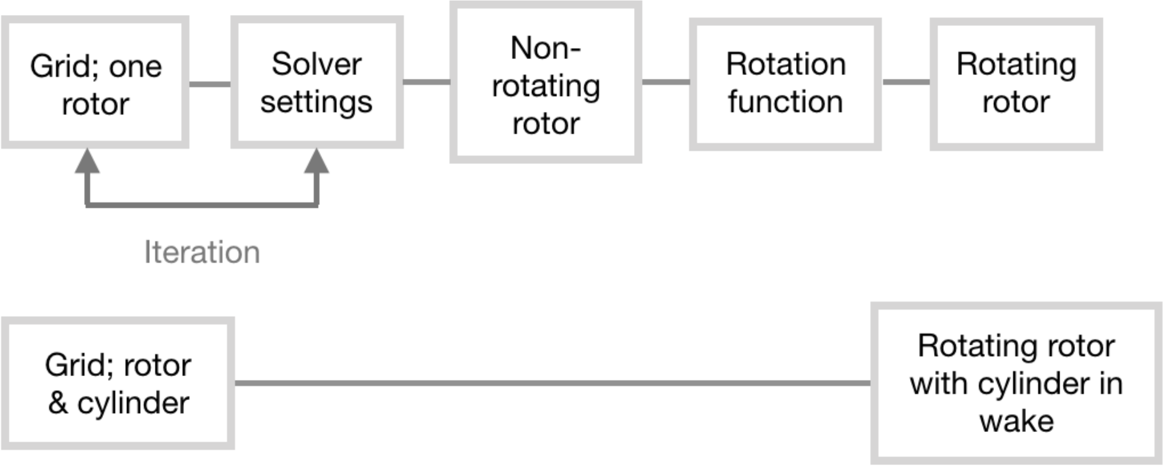

Figure 5.1: Steps undertaken to create the CFD simulations used to answer the second part of the research question.

First the flow regimes that can be expected around a rotating rotor will be presented in this chapter. This serves as background and will be used to determine the grid and solver settings of the CFD simulations. The flow description will also be used to explain the behavior of the determined flow coefficients. That discussion and the results will be presented in chapter 7.

After the flow description around a rotating rotor a general description of CFD simulations will be presented. Where after the creation process of the performed CFD simulations will be set out.

5.1. Flow regimes

The flow regimes around a (rotating) rotor are critical for the description and determination of the loads acting on the rotor. In this section the different regimes and their Reynolds numbers will be discussed where after the influence of the flow on the (rotating) rotor.

The flow around an rotor is complex. Three shear layers; a boundary layer, separating shear layer and a wake interact with each other and dictate the flow around the rotor. They interact with each other in the three dimensional domain and their behavior is typified by the Reynolds number (Re) shown in equation 5.1.

$$Re = \frac{U_\infty \cdot D}{\nu} \tag{5.1}$$

The flow regimes are divided by the behavior of the three shear layers and indicated with a Re range. Williamson [45] has performed an in depth research on the different flow regimes. Sing et. al. [37] used Williamson's work in the paper "Flow past a cylinder: shear layer instability and drag crisis". From that paper the indications of the flow regime, here presented, are used.

Steady flow	Two steady symmetric vortices on each side of the wake center line	Re~0-47
Unsteady laminar	Flow remains laminar but becomes unsteady and asymmetric	Re~47-160
Turbulent	Three dimensional instabilities appear	Re~190
	Turbulent with unstable separated shear layer	Re>190
Drag crisis/critical flow	Boundary layer on the cylinder goes from laminar to turbulent	Re~ $2 \cdot 10^5$

Table 5.1: Flow regimes, their description and Re for a non-rotating cylinder [37].

Important to note is that the free-stream turbulence and surface roughness influence the transition Re values significantly. After the drag crisis (explained in appendix C) the drag coefficient starts to increase again because of the shear stresses in the now fully turbulent boundary layer. The drag crisis can be seen in figure 5.2 where it is shown as the drop in the drag coefficient. The significant influence of the surface roughness can also be seen in this figure expressed with $\frac{k}{D}$, with k the surface roughness.

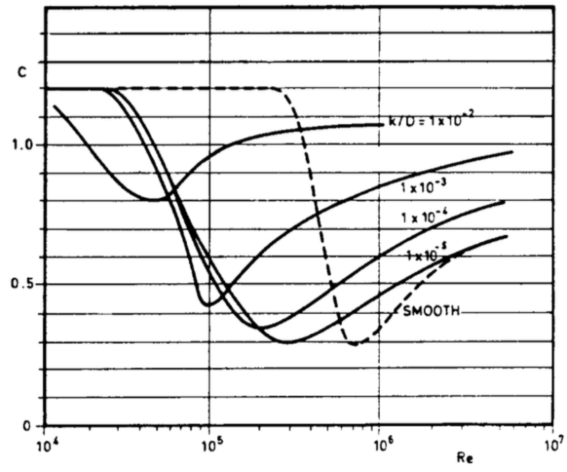

Figure 5.2: Drag coefficient for different wall roughness's [15] .

The differences in flow behavior for different Re, also indicates the necessity to compare researches with the same Re to, for example, validate.

This thesis embodies a flow around a (rotating) rotor with a Re of $8 \cdot 10^5$. Which is post-critical following table 5.1. As shown in figure 5.2 the drag crisis for a smooth cylinder occurs at higher Re, compared to cylinders with a rougher surface. The roughness of the surface influences the location of the detachment of the shear layer and the level of turbulence in the boundary layer. Thereby it influences the Re for which the drag crisis occurs. *The calculations in this thesis are performed for a cylinder with a completely smooth surface.* Therefore the drag crisis might be seen in the results of this thesis with this Re. The drag coefficients of simulations with increasing SR's, will then not increase as expected.

Flow around an (rotating) cylinder

In this section the flow around a non-rotating cylinder will be described. The flow is described in this section so that the principles that will be used to explain the results, are already explained. The flow around a rotating cylinder will be elaborated on afterwards.

The expected flow around a cylinder, for the Re used in this thesis, is presented by the research of Catalano et. al.. Catalano et. al. [5] have performed a two dimensional simulation of a cylinder in a super-critical Re range. Their goal was to evaluate the usage of the Large Eddy Simulation (LES) model to simulate a cylinder at these high Re. Their image of the magnitude of the instantaneous vorticity around a cylinder at Re$\sim 1 \cdot 10^6$ for a LES and a URANS simulation is shown in figure 5.3.

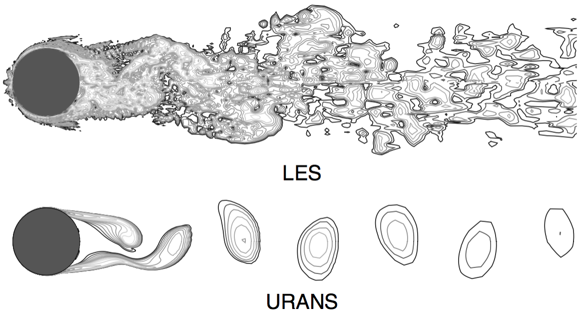

Figure 5.3: Instataneous vorticity magnitude for 25 countourlevels $\left(\frac{\omega D}{U_\infty} = 1 \text{ to } 575\right)$ [5] .

The boundary layer close to the cylinder is thin, fully laminar and attached. The turbulence that can be seen in the LES image in figure 5.3, near the boundary layer, are small but are necessary to display the wake shape. A large and wide wake increases the drag coefficient where a slim wake causes a lower drag coefficient. Sup- and super-critical Re flows cause vortex shedding behind a cylinder forming the Karman street. In the URANS image in figure 5.3 the vortex street is more clear than in the LES image. The vortex shedding is important to describe, it causes a fluctuation in the total load in the xy-plane but also in z-direction on the cylinder surface. These fluctuations of the load can cause vibrations that need to be taken into account when implementing a Flettner rotor on a cruise vessel. The vortex creation is typified by the Strouhal number. The Strouhal number (St) depicts the flow oscillation determined by equation 5.2.

$$St = \frac{fD}{U_\infty} \tag{5.2}$$

The expected St for a non-rotating cylinder at Re$\sim 8 \cdot 10^5$ lies inbetween 0.2 and 0.3 [5][24]. As stated before the modeling of the wall of the cylinder has large influence on the St.

To represent the rotational properties of a rotating cylinder the spin ratio is used. The spin ratio (SR and α) is the ratio between the velocity of the outer fiber of the cylinder and the free stream velocity. The SR and the Re are used to represent the flow around a rotating rotor. The dimensional charachteristics of a Flettner rotor are depicted by the Aspect ratio (AR). The AR is the ratio between the height of the rotor and its diameter.

Because of the rotation of the cylinder, one side will move along with the flow velocity around the cylinder and one side will move against the flow velocity. The differences in flow velocity around the cylinder causes a pressure drop on the cylinder surface. The flow bends towards the lower pressure area and is no longer symmetrical. Until a critical SR is reached the rotor will continue to shed vortices but no longer around the symmetry axis. Karabelas et. al. [24] have performed two dimensional simulations around a rotating cylinder for high Re. They created figure 5.4 showing the flow around a rotating cylinder for Re$\sim 5 \cdot 10^5$, $\sim 1 \cdot 10^6$ and $\sim 5 \cdot 10^6$.

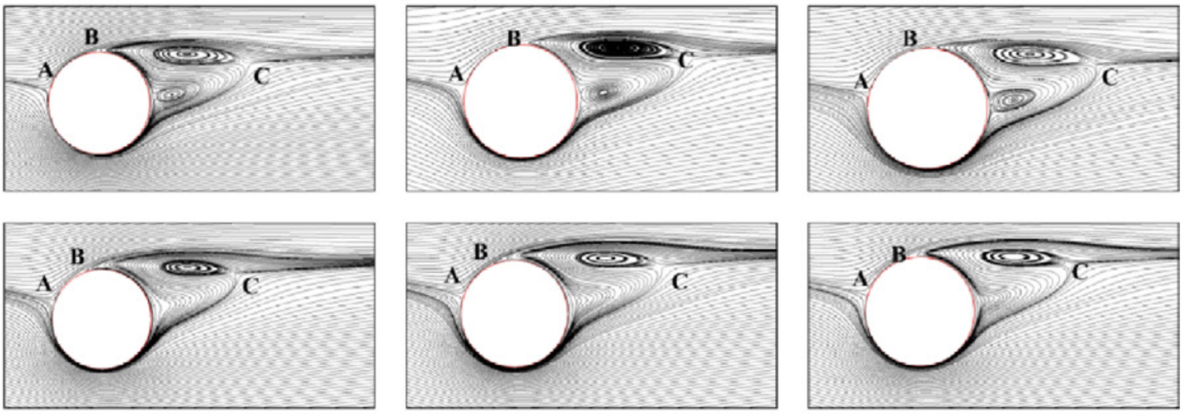

Figure 5.4: Rotating cylinders with their streamlines for Re~ $5 \cdot 10^5$, ~ $1 \cdot 10^6$ and ~ $5 \cdot 10^6$ [24] .

The top row is for a SR of 2 and the second row is for a SR equal to 3. The reason that in this thesis the figures are only shown for a minimum SR of 2 is that Karabales et. al. state in their research that the flow becomes steady at spin ratio's higher than 2 and Re higher than $5 \cdot 10^5$. They have used a RANS simulation to create these figures where vortex shedding would not have been visible at lower SR.

In figure 5.4 the two vortices that were shed now stay near the cylinder in shape of detached instable shear layers. The stagnation point (B) moves more to the front of the cylinder because of the increasing pressure difference induced by the rotation. The first row of figures for a SR~2 show the reattachment of the lower vortex. With in the second row for SR~3 the lower vortex is nearly completely reattached. The lower vortex can only reattach when the laminar boundary layer is becoming more turbulent. The flow of the lower vortex can then mix with the boundary layer.

With these observations the behavior of the drag coefficient can be explained.*The drag coefficient quantifies the drag or resistance of an object in a flow.* For example, a wider wake near the boundary of the rotor, including an (unstable) shear layer, will increase the drag coefficient. When the unstable, shedded, shear layer implodes further away from the rotor, the drag coefficient will increase. The unstable shear layer imploding away from the rotor, does not increase the resistance on the rotor, as an attached unstable shear layer does.

These kind of behavioral aspects are important to evaluate because they directly influence the magnitude of the drag coefficient. A change in the drag coefficient may cause a change in vortex shedding intensity and frequency, and total load direction and magnitude. When the behavior can be predicted based on SR and Re the rotor usage can be optimized.

5.2. General description of CFD simulations

The Kutta-Joukowski theorem does not take the viscous effects of the flow around the Flettner rotor into account. To gain a more realistic image of the load acting on the Flettner rotor the drag, caused by the viscous properties of the flow, needs to be included. The most accurate way to do this is to set up Computational Fluid Dynamic (CFD) simulations. With these simulations the true physics are captured of the flow around the rotor.

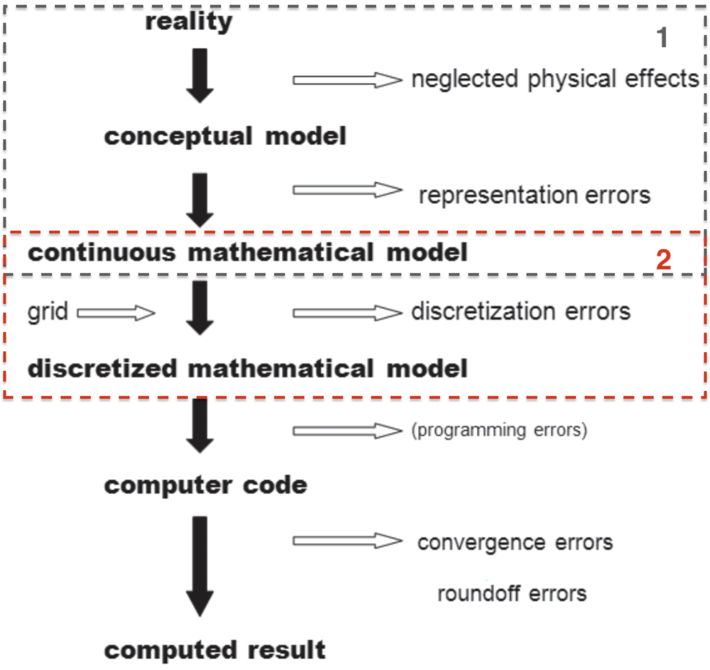

Figure 5.5: Sources of errors in computed results [27].

In figure 5.5 the steps are presented to go from reality to computed results. Larsson et. al. [27] show where estimations are made of the physical truth, and accordingly, where errors appear. Most of the errors appear because of limited computational resources; meaning that the simulation time should be realistic and the simulation needs to be stable to be reliable. The reliability of the simulations will be discussed in chapter 6. Here only a clarification of what the CFD simulations represented will be given. The actual settings of the simulations will be presented in section 5.3.

The CFD simulations simulate the actual flow around an object by determining the Navier Stokes (NS) equations on grid points. That grid represents the domain where the flow properties are determined for. The NS equations represent in that domain the properties of the flow. The steps representing the switch between the physical flow to the NS equations are denoted by 1 in figure 5.5. The representation of the domain by the grid is the discretization of the mathematical model, denoted by 2 in figure 5.5. When the model is discretized the simulation needs to be run on a computer. The software that performs the calculations in all the grid points needs to be programmed.

The continuous NS equations are explained in appendix D.1. As mentioned before the continuous NS equations represents the flow in the considered domain. The considered domain sets boundary conditions that can be applied to the NS equations. Those boundary conditions are represented by slip and no-slip conditions. With the no-slip condition velocity differences are considered zero; the air "sticks" to the surface of the rotor.

A result of the no-slip condition is that the flow velocity has to decrease to the velocity of the boundary of the rotor. Causing the Reynolds number to decrease and resulting in a very thin laminar layer very close to the boundary of the rotor. Because of this the shear stresses on the wall of the rotor can not be measured.

5.2.1. Model tests to estimate the flow

The most accurate way of determining the loads acting on the Flettner rotor would be by performing real size experiments. The Flettner rotor is only too expensive and large to perform, controlled, measurements. The solution for that would be to perform model tests. To be able to perform the model tests for the same Re as the flow around the Flettner rotor the flow velocity would have to be very high. The wall effects of the wind tunnel test location or towing tests need to be small as well. Therefore large facilities would be needed to perform accurate model tests. In chapter 6 model tests will be elaborated on more.

5.3. Performed CFD simulations

In this section the CFD simulations to determine the flow around a (rotating) rotor will be elaborated. After this section the used grid, domain and solver settings should be clear for the reader.

The goal of the simulations are to determine:

1. The lift and drag coefficients of a rotating Flettner rotor for three spin ratio's
2. The change in the lift and drag coefficients of a rotating Flettner rotor for one spin ratio when a superstructure is placed downstream
3. The behavioral aspects of the flow around the rotating rotor for different spin ratio's

The simulations are performed in three stages as shown in figure 5.6.

During stage 1 three simulations are run with the exact same solver settings, but with three progressing finer grid refinements. Grid 1 has the coarsest refinement level and grid 3 has the finest level of refinement. The goal of this stage is to select a grid refinement for which the result of the simulation is independent of the grid refinement. The selection of this grid is called a grid refinement study. The grid refinement study is considered part of the verification process of the CFD simulations and will be discussed in chapter 6.

In stage 2 a function is applied to the boundary of the cylinder to make it rotate (appendix G). The goal of this stage is to create simulations with different rotational speeds, which later can be compared. For one of the rotational speeds, out of stage 2, a cylinder will be placed in the wake to evaluate the interaction between both (stage 3).

The creation of the performed simulations consists out of two steps that are iterated until the calculations run smoothly and the results converge. First the grid is computed and second the solver settings are chosen. The creation of the simulations will be discussed in the same order in this section.

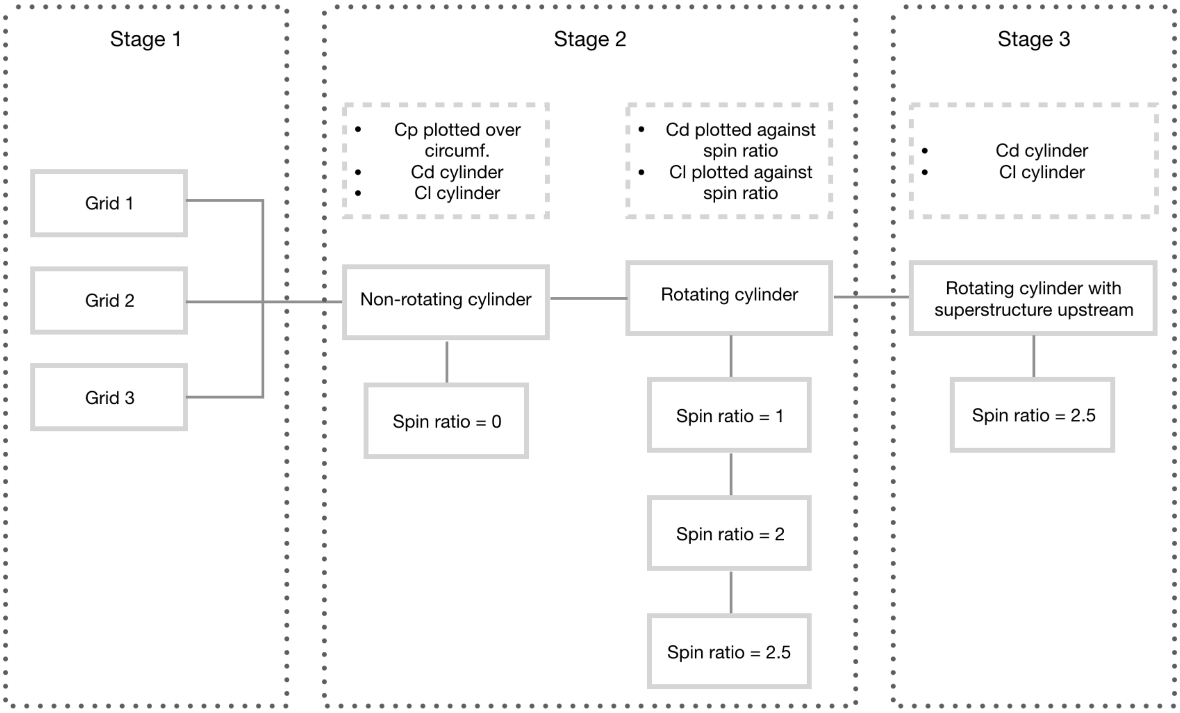

Figure 5.6: Performed simulations.

5.3.1. Grid creation

To clarify the grid creation, first will be explained what exactly is simulated.

The Flettner rotor will be represented in the simulations by a cylinder in a square domain. The domain in this research represents a voluminous grid defined by boundaries at its edges. The Flettner rotor is represented by a rotor, which rotates when a function is applied to its boundary. The height of the rotor is equal to that of the domain. The influence of the flow around the top of the rotor is thereby not included in this simulation. A cross section of the domain with rotor is presented in figure 5.7. This is a cross section of the domain in x- and y-direction. All dimensions are expressed in the diameter of the rotor. This is done so that the grid, and results, can be compared to other researches.

In figure 5.7 there are five boundaries and one domain. The domain goes from the boundary of the Flettner rotor to the four boundaries that represent the edges of the domain. As can be seen in figure 5.7 the domain consists out of three different grids, in order of refinement and orientation. The different grids are numbered in red numbers in figure 5.7. The Flettner rotor is only represented by its boundary. The three different grids represent:

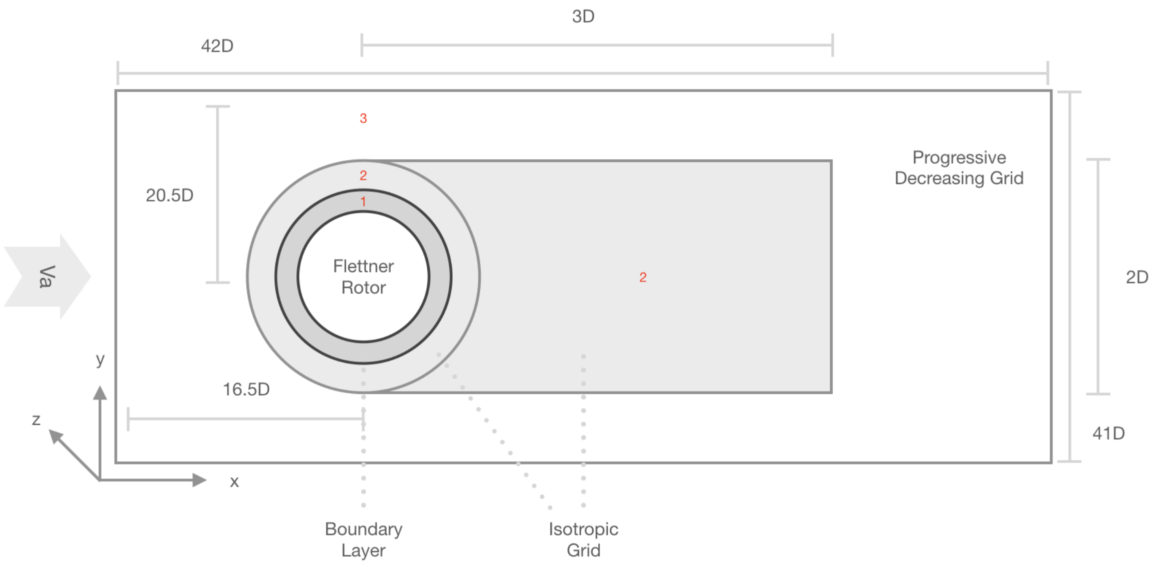

Figure 5.7: Cross section in the xy-plane of the domain.

1. The boundary layer
2. The refinement zone
3. The environmental grid

They will be discussed in the same order as mentioned above.

5.3.2. Grid properties

The boundary layer is displayed in figure 5.7 with the red number 1. It is connected to the boundary of the cylinder. The boundary of the cylinder consists out of a number of vertices equally distributed on the circumference. The number of vertices on the boundary of the cylinder represents the refinement of the whole domain. The three different grids are transitioning smoothly into each other. The settings of the next grid propagate from a zone of equal grid spacing, between the previous and the next grid. A changing refinement of a grid occurs with a constant factor, thereby when the number of vertices change on the circumference of the cylinder the refinement of the whole domain changes.

The boundary layer

The boundary layer develops because of the no slip condition, given to the boundary of the cylinder. White shows in his book "Viscous Fluid Flow" [44] plots for velocity profiles in a turbulent flow near a wall. What stands out is that these velocity profiles drop linearly to zero within a thickness too small to be seen near the wall. The behavior of the velocity profiles is separated into three layers by Ludwig Prandtl and Theodore von

Karman. The inner layer, the layer closest to the wall, is following their division dominated by viscous shear. Another important statement by Prandtl is that the profile in the inner layer is dependent on wall shear stress, fluid properties, and distance y from the wall, but not upon the freestream properties. The profiles shown by White are determined after dimensional analysis, therefore the variables in the formulation of the profiles can be reduced to two dimensionless parameters, shown in equation 5.4. Using the definitions in equation 5.3.

$$\frac{\bar{u}}{v^*} = f\left(\frac{yv^*}{\nu}\right), \; v^* = \left(\frac{\tau_w}{\rho}\right)^{\frac{1}{2}} \tag{5.3}$$

$$y^+ = \frac{yv^*}{\nu}, \; u^+ = \frac{\bar{u}}{v^*} \tag{5.4}$$

Here v^* is the wall friction velocity. Very near the wall the turbulence is damped out and the boundary layer is dominated by viscous shear. For very small y the velocity profile is linear; $u^+ = y^+$. This very thin layer near the wall is called the viscous sublayer. To capture the flow properties near the wall the space between the boundary of the cylinder and the first vertice is determined for $y^+ = 1$. By using $y^+ = 1$ the viscous sublayer is included in the simulation. The distance between the boundary of the cylinder and the first vertice, Y_{wall}, is determined by equation 5.5.

$$Y_{wall} = 6\left(\frac{V_{ref}}{\nu}\right)^{-\frac{7}{8}}\left(\frac{L_{ref}}{2}\right)^{\frac{1}{8}} Y_1^+ \tag{5.5}$$

Here the reference length is the diameter of the Flettner rotor (D) and the reference velocity is determined by $V - \omega \times \left(\frac{D}{2}\right)$. The first layer wall thickness is $8.78 \cdot 10^{-5}$ m. With the first layer wall thickness the boundary layer is grown, with a growth ratio of 1.15, until it reaches the total thickness equal to the circumference of the rotor divided by the number of vertices placed on it.

The boundary layer shown in figure 5.7 is shown in the xy-plane in figure 5.8 and in the xz-plane in figure 5.9. In appendix G the excel used to determine the boundary thickness of grid 2 is added.

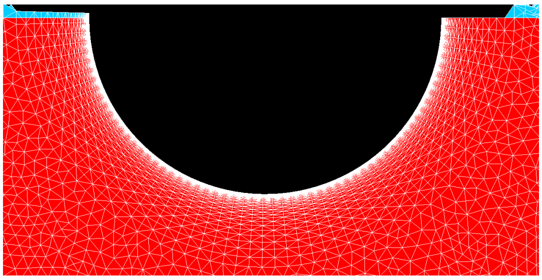

Figure 5.8: Boundary layer in the xy-plane.

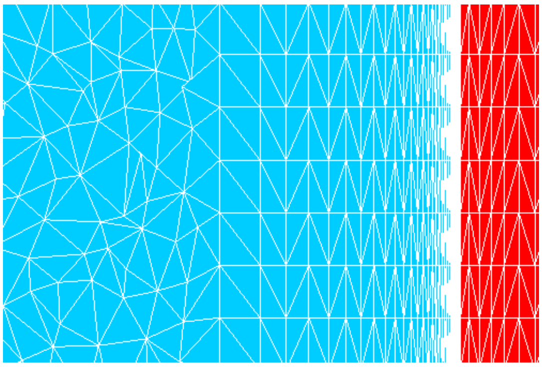

Figure 5.9: Boundary layer in the xz-plane.

In figure 5.8 the boundary of the layer of the rotor can be clearly seen with a linear cell growth until the determined boundary layer thickness is reached. The refinement of the grid near the boundary of the rotor is significant, with respect to the rest of the grid in the domain. Beside the linear growth of the distance between consecutive vertices in the xy-plane, the *structured* grid orientation in the xz-plane can be seen in figure 5.9. The spacing of the vertices along the boundary of the cylinder in z direction is 66 vertices for the total height of 3D meter, resulting in a distance between two consecutive vertices of 0.04545D meter. This is coarse with respect to the dimensions of the boundary layer but fine enough to capture the three dimensional effects in the wake. A fine distribution of vertices in z-direction on the boundary of the cylinder is very costly on the heaviness of the grid. The height of 3D meter is the minimal height of the cylinder to capture the three dimensional effects. Papaioannou et al [33] uses a height of 4D meter for a flow with a Reynolds number of $Re = 10^2 - 10^3$. Greco [18] stated, in a lecture at the Norwegian University of Science and Technology, how long a cylinder for a three dimensional simulation should be expressed in the correlation length. Figure 5.10 shows a plot drawn based on the lecture by Greco [18].

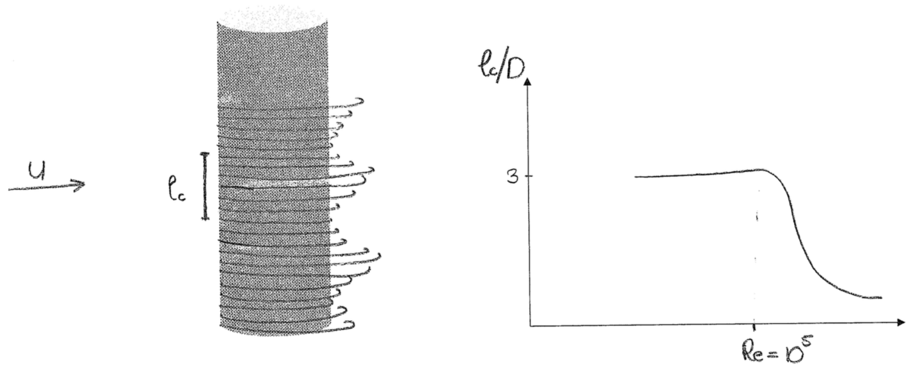

Figure 5.10: The correlation length of a cylinder expressed against the Reynolds number.

The correlation length is the length of the rotor where over the drag force fluctuates one period. The drag load can be higher or lower when two dimensional simulations are used. Depending on where in the fluctuation of the load the two dimensional cross section is located. The correlation length is, naturally, dependent on the Reynolds number. Because the flow around the rotor becomes super critical at high Reynolds numbers the correlation length decreases after $Re = 10^5$. Therefore the height of $3D$ meter used in this research, is high enough to capture the full three dimensional effects and to make the assumption that the simulated rotor has an infinite height.

Rotation of the rotor

To make the rotor rotate a function is applied to the boundary of the cylinder. This function applies a velocity in x- and y-direction to the vertices on the boundary, representing the rotation of the cylinder. Two python scripts were written to apply these velocities and they are both added in Appendix G.

Refinement zone

As can be seen in figure 5.9, after the boundary layer the grid changes in orientation of the vertices. The grid is *unstructured* in the whole domain except in the boundary layer. The computational time would become too significant when the whole domain would contain a structured grid. A refinement zone is computed around the rotor to correctly simulate the wake and to decrease computational time; the grid refinement is coarser outside the refinement zone.

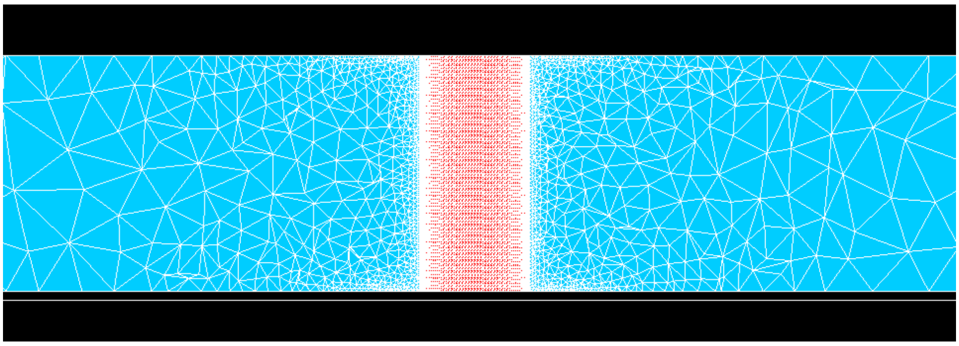

Figure 5.11: Refinement zone before 1st metric (yz-plane).

The dimensions of the refinement zone are derived from other researches. The purpose of the refinement zone is that the result of a simulation does not change with a refinement zone compared to a simulation with the fine grid throughout the whole domain. The dimensions of the refinement zone can be seen in figure 5.7, it can also be seen that the refinement zone consists out of a cylinder around the rotor merging with a box around the wake. The refinement zone is achieved by applying a metric to the grid in the zone with the dimensions of the refinement zone. In figure 5.11 the cylinder (red) is shown in the domain (blue) before a metric is applied. It can be seen that the mirror planes, the top of the domain and the bottom of the domain, already contain the two dimensional metric. The grid progresses randomly from the two dimensional metric and the grid refinement outside the boundary layer to the coarse grid refinement at the boundaries of the domain.

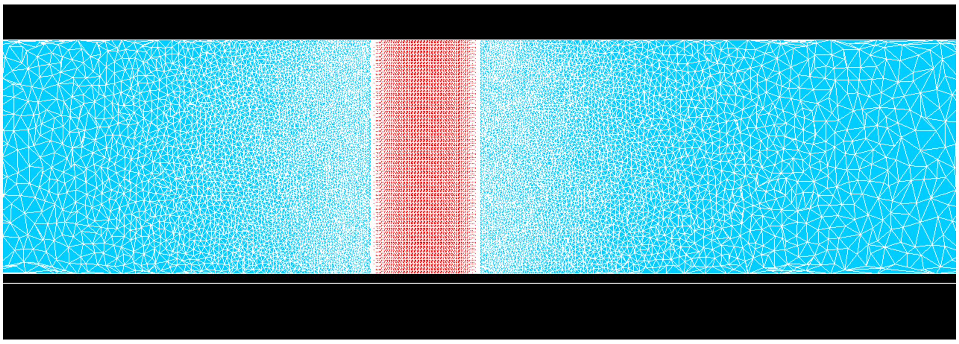

Figure 5.12: Refinement zone before 2nd metric (yz-plane).

In figure 5.12 the metric is applied for the first time, resulting in a finer grid throughout the domain. After the first metric the refinement satisfies the first purpose of the refinement zone; to refine the grid to simulate the wake correctly. However the grid in the whole domain seems to be finer, which is not beneficial for the computational time.

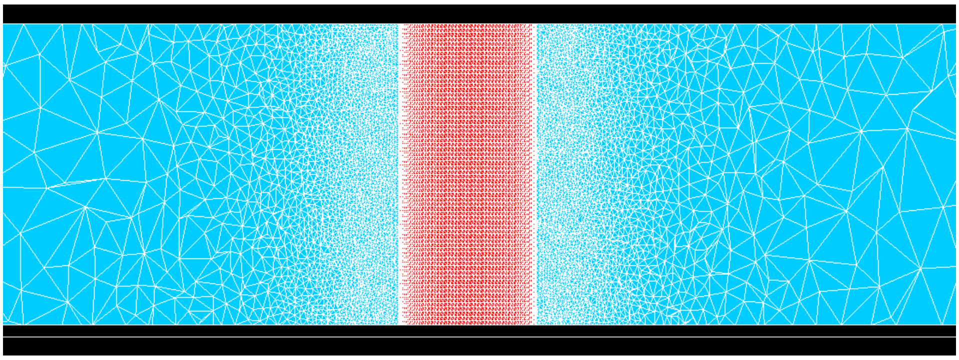

Figure 5.13: Refinement zone before 3rd metric (yz-plane).

After the second application of the metric the grid seemed fine enough in the refinement zone and the decreasing refinement near the boundaries of the domain was more profound. The difference between the result after the second metric application and the third metric application was small. The two time application of the metric was therefore considered enough to create the refinement zone.

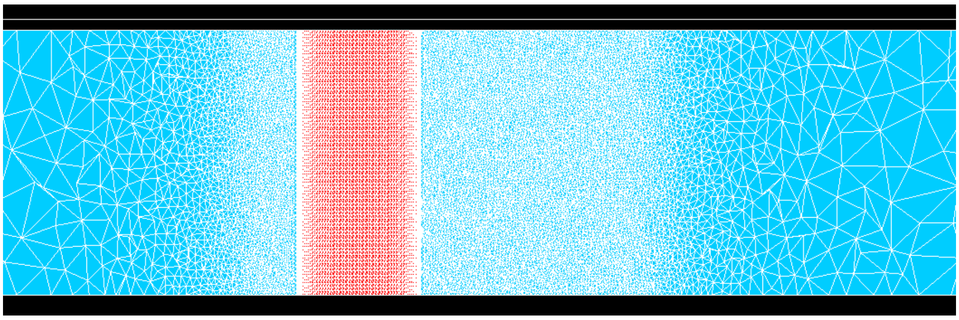

Figure 5.14: Refinement zone before 3rd metric (xz-plane).

In figure 5.14 the same grid is shown as in figure 5.13 only in the xz-plane. It can be seen that the refinement zone continues in the x direction after the rotor to capture the wake. The refinement zone is isotropic as can be seen in figure 5.14.

The environmental grid

In figures 5.11-5.14 it can be seen that the isotropic refinement zone transitions in a less refined and unstructured grid. The grid refinement deduces until the distance between the vertices on the edges of the domain is equal to D. The mesh is unstructured and coarse because the data that is determined in these mesh points is less relevant. The domain has to have a certain size to neglect wall effects and approach the physical truth.

Cylinder in wake

Beside simulations of non-rotating and rotating rotors, there will also be a simulation performed including a cylinder in the wake of a rotating rotor. The grid of that simulation is shown in figure 5.15.

As can be seen in figure 5.15, the rotor has the exact same grid properties as the simulation of only a rotor. The non-rotating cylinder has the boundary layer properties of the coarsest grid from the grid refinement study. An extra refined grid has been merged with the original refinement grid. The new refined grid is slightly coarser than the initial one. This is because only the loads acting on the rotating cylinder are captured.

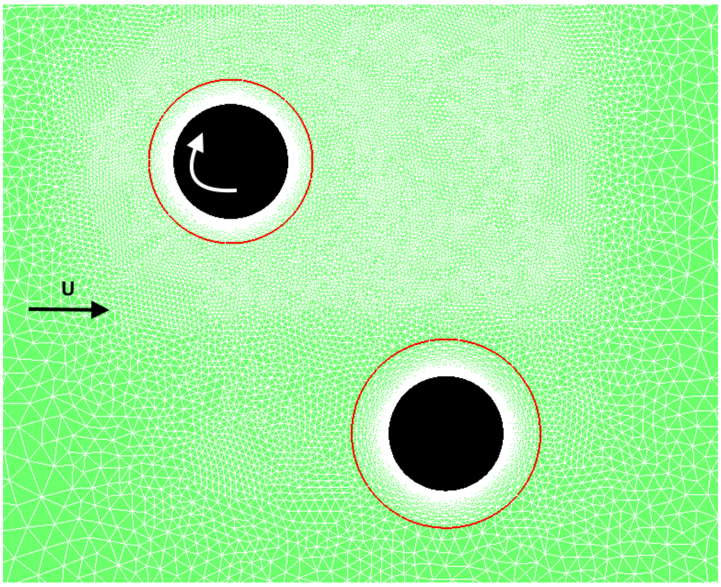

Figure 5.15: Grid for the simulation containing a rotating cylinder and a non-rotating cylinder (xy-plane.

5.3.3. Solver settings

In this section the solver settings, that are used to determine the NS equations in each grid point will be explained. First the definition of turbulence is presented with afterwards the different methods of simulating it. At the end of this section the chosen solver and model will be presented.

A laminar flow is stable where turbulent flows are diffusive, time dependent, and involve three dimensional vorticity fluctuations with a broad range of time and length scales [30]. An description of turbulence is given by Kolmogorov [26]; *turbulence consists out of eddies of different sizes each possessing and amount of energy dependent on their size.* Larger eddies break up into smaller eddies and transfer their energy to them. This occurs for every eddy scale. This continues to occur until eddies are formed that are so small that the molecular viscosity, for that scale of eddy, is very effective at dissipating the turbulent kinetic energy into heat.

To simulate a turbulent flow the discrete NS equations can be solved directly by a Direct Numerical Simulation (DNS). To solve the discrete Navier Stokes equations on a grid point, the time steps that needs to be used should be very small and the grid should be very fine. Otherwise not the entire spectrum of temporal and spatial eddies can be resolved. The computational costs for such a simulation are too expensive to be used in this thesis.

A method to reduce the computational costs is the Large Eddy Simulation (LES). With that method the larger eddies are directly simulated and the smaller eddies are modeled with sub-grid scale models. To use LES the determination needs to be made which scales can be modeled and which scaled need to be directly simulated. The direct simulation of eddies is more expensive, in terms of computational effort, then modeling. The selection of eddies is performed by a spatial statistical filter. Moukalled et al. state that the flow is still accurately simulated using LES because the smaller eddies can be considered isotropic and independent of the flow [30].

The most popular method to replace DNS is by solving Reynolds Averaged Navier Stokes (RANS) equations. Here the NS equations are averaged only based on time. The Reynolds decomposition is used to divide the flow properties into mean and fluctuating components as shown in equation 5.6. Where x is a position and t a time. The redefined flow properties are implemented in the NS equations and time averaged.

$$\phi(\mathbf{x},t) = \bar{\phi}(\mathbf{x},t) + \phi'(\mathbf{x},t) \tag{5.6}$$

The mean ($\bar{\phi}$) can be determined by three techniques:

1. Time averaging; averaging over a time interval and only suitable for stable turbulent flows
2. Spatial averaging; averaging over a space or volume interval and suitable for homogeneous turbulence
3. Ensemble averaging; a average of many identical quantities at a certain time; suitable for any type of turbulent flow and dependent on position and time

For an incompressible flow, like the flow in this thesis, the variables that will be rewritten using RANS are the velocity, pressure and temperature. The Reynolds averaged equations have, in addition to the discreet NS equations, a Reynolds stress tensor and turbulent heat fluxes. The Reynolds stresses are not solved in the RANS equations and can be solved by turbulence modeling.

Turbulence models directly model the Reynolds stress and are based on the Boussinesq hypothesis [3]. This hypothesis assumes that the Reynolds stress is a linear function of the mean velocity gradients. The formulation for the Reynolds stress is given in equation 5.7, for an incompressible flow.

$$-\rho\overline{\mathbf{v}'\mathbf{v}'} = \mu_t\left(\nabla\mathbf{v} + (\nabla\mathbf{v})^T\right) - \frac{2}{3}\rho k\mathbf{I} \tag{5.7}$$

In equation 5.7 k is the turbulent kinetic energy, defined as $k = \frac{1}{2}\overline{\mathbf{v}'\mathbf{v}'}$. μ_t represents the turbulent eddy viscosity. The purpose of turbulence models is to determine those two variables of the Reynolds stress.

There are a lot of turbulence models but only the two most popular models will be discussed; the $\kappa-\epsilon$ model and the $\kappa-\omega$ model. Both models are two-equation models, of which the idea lies in the name. They necessitate the solution of two transport equations to determine μ_t. In all the turbulence models μ_t is expressed in terms of $\left(\sqrt{k}\right)$ and length scales l.

The $\kappa-\epsilon$ model uses the turbulent viscosity μ_t and thermal diffusivity k_t presented in equations 5.8 and 5.9.

$$\mu_t = \rho C_\mu \frac{k^2}{\epsilon} \tag{5.8}$$

$$k_t = \frac{C_p \mu_t}{\mathbf{Pr}_t} \tag{5.9}$$

In equation 5.8 ϵ represents the rate of dissipation of turbulent kinetic energy per unit mass, due to viscous stresses. In the standard $\kappa-\epsilon$ model the flow is assumed to be fully turbulent and the effects of molecular viscosity to be negligible. This turbulence model can be used for fully turbulent free shear flows. Using this model near solid walls, like the wall of the rotor, is not recommended. As the low Re effects that occur near walls, are not rightly captured by the turbulent viscosity. A solution is to damp the turbulent viscosity with respect to the distance to the wall. Where at the wall the turbulent viscosity goes to zero.

A Turbulence model that can be integrated all the way to the wall is the $\kappa-\omega$ model. The ω represents the rate at which turbulence kinetic energy is converted into internal thermal energy per unit volume and time. This model is better in predicting separated flows. Even though the goal is to simulate the flow around the rotor, the focus lies not only on the shear layer around the rotor. The $\kappa-\epsilon$ model is a better model for the complete flow, especially to capture the turbulence in the wake. A drawback of both models is that the stagnation point anomaly causes a over-prediction of the turbulence kinetic energy production[30]. Moukalled et al. state that this occurs when a moderate level of k is subjected to a large rate of strain. This will be considered when a fully turbulent boundary layer is evaluated with respect to the drag crisis. For the drag crisis the position of the stagnation points is important. As a fully turbulent boundary layer increases the strain on the cylinder surface.

The $\kappa - \epsilon$ model can be modified to include the Shear Stress Transport (SST) model. This model improves the adverse pressure gradient performance. It combines the $\kappa - \epsilon$ model and the $\kappa - \omega$ model. The properties of the $\kappa - \omega$ model are used near the wall of the cylinder so that the right levels of turbulent viscosity are captured.

Another way to save computational effort is by combining LES and RANS. The best known method using this principle is the Detached Eddy Simulation (DES). DES switches between LES and RANS dependent on the Reynolds number. Regions with a more turbulent flow will be simulated with LES. The switch between RANS and LES is dependent on the domain dimensions and the global size of the mesh. Thereby only one mesh can be used which is dependent on the geometries of the domain. When the exact location of the separation point of the flow on, for example the rotor's boundary, is not precisely known, a Delayed Detached Eddy Simulation (DDES) can be used. This solves the problem that a switch from RANS to LES occurs too soon whereby the RANS mesh is not preserved.

As explained above, the RANS equations divide the flow properties in a mean and fluctuating component. This is done for a fixed time step which should be small enough for the simulation to be stable and converge. By using this method the unsteadiness of the flow is not entirely captured because there is averaged over time. For the unsteady RANS (URANS) equations an additional unsteady term is added to the momentum equation. Resulting in a result expressed with a variable time. The time step that is used in the URANS equations can vary where for the RANS equations a fixed time step is used.

The simulations performed for this thesis will be unstable because of the Re of the flow; vortices might be shed by the cylinder. To capture those fluctuations a URANS simulation is created with an $\kappa - \epsilon\ SST$ turbulence model. Capturing the turbulence behavior of the boundary layer of the cylinder. As explained an other option for the simulations would have been an combination of DDES and RANS. With the LEMMA software simulations with these principles have not been performed yet. Therefore there is chosen to use the less computational recourse consuming, but still reliable, combination of URANS and the $\kappa - \epsilon\ SST$ turbulence model. In the chapter "Review state of the art" 3 researches using URANS and the $\kappa - \epsilon\ SST$ turbulence model are reviewed.

In figure 5.2 on page 28 it can be seen how much influence the roughness of an object can have on the drag coefficient. In CFD simualations the roughness of an object are represented by a wall law. *The CFD simulations for this thesis do not include a wall law.* The effect of not having a wall law influences the position of the the transition point, where the laminar boundary layer becomes turbulent, on the cylinder boundary. The stagnation point of the flow on the cylinder boundary is also influenced by a wall law. The stagnation point of the flow, on the cylinder boundary, influences together with the transition point, the formation of the wake and the St of the flow. The turbulent properties of a flow can also be artificially changed by changing the surface roughness of an object. As is often done in windtunnel tests when a certain Re flow cannot be created because of high flow velocities and wall effects. These two arguments show how important a wall law is but also how large and uncertain the effect of changing the surface roughness is. Because the main goal of this research is not to simulate the flow around the Fettner rotor with the most precision, but to evaluate its behavior on a cruise vessel, no wall law is used.

6

Verification and validation of CFD simulations

Computational resources are used to evaluate physical reality and to determine the characteristics of events under varying conditions. Physical reality will be represented by a simulation to make the computational calculations. By using an simulation the accuracy of that simulation needs to be determined. The accuracy is the agreement between the reality and the simulation. That accuracy is expressed by the error; the difference between a simulation value or an experimental value and the truth [39]. For the simulations performed in this thesis the true properties are not known and experiments hard to perform. Therefore the error needs to be estimated. The uncertainty (U) is an estimate of the error such that the interval $\pm U$ contains the true value of the error (δ) 95 times out of 100 [39]. The processes of evaluating the accuracy are called verification and validation

Verification and validation are two independent processes and should be considered as such. AIAA shows the difference in their definition, verification considers the "correctness" of the process leading to the results. Where validation considers if the right process is performed [8].

In this chapter verification and validation are divided, first the verification will be discussed. The verification of this research consists out of a:

1. Uncertainty assessment
    (a) Grid convergence study

The grid convergence study verifies the discretization of the domain and researches the independence of the simulation thereon. The validation consists out of:

1. Comparison to literature
2. Multiple runs of the same simulation
3. Proposal for windtunnel tests

The literature will be discussed in chapter 3 on page 13, in this chapter only the results will be compared to validate this research. The difficulties will be discussed, that arise from comparing different simulation methods. Wind tunnel tests have not been performed explicitly for this research. There is however, in collaboration with Peutz, a wind tunnel test set up proposed.

6.1. Verification

In the verification the simulation numerical uncertainty (U_{SN}) is evaluated. This uncertainty is mostly dependent on the input parameters that are chosen. The error corresponding to the simulation numerical uncertainty is denoted by δ_{SN} presented in equation 6.1.

$$\delta_{SN} = \delta_I + \delta_G + \delta_T + \delta_P = \delta_I + \Sigma_{j=1}^{J} \delta_j \tag{6.1}$$

δ_{SN} consists out of errors because of:

- Iterations δ_I
- Grid size δ_G
- Time step δ_T
- Other parameters δ_P

The estimation of the error δ_{SN} is presented by δ^*_{SN} and is given in equation 6.2.

$$\delta^*_{SN} = \delta^*_I + \Sigma^J_{j=1}\delta^*_j \tag{6.2}$$

The simulation result corrected by the determined uncertainty is then presented by:

$$S_c = S - \left(\delta^*_I + \Sigma^J_{j=1}\delta^*_j\right) + T + \delta_{SM} + \epsilon_{SN} \tag{6.3}$$

With S_c the corrected simulation value, T the truth, δ_{SM} the simulation modeling error and ϵ_{SN} the error in δ^*. The uncertainty corresponding to the corrected simulation result is presented by $U^2_{S_CN} = U^2_{I_C} + \Sigma^J_{j=1}U^2_{jC}$. The definition of verification can be expressed based on equation 6.3; $S = S_C + \left(\delta^*_I + \Sigma^J_{j=1}\delta^*_j\right)$.

6.1.1. Iteration uncertainty

The iteration uncertainty is reviewed by looking at the fluctuations of the time history of the results in the last few periods. The time steps of the URANS simulations are nearly equal there, but this method is still more unreliable for URANS than for RANS simulations. The uncertainty because of the iteration is expressed as $U_I = \left|\frac{1}{2}\left(S_U - S_L\right)\right|$. With S_L and S_U the lower and upper results of the simulation. The uncertainty because of the iteration was smaller than that of the grid size (next section). Because of that the iteration uncertainty was concluded to be negligible with respect to the grid size uncertainty.

6.1.2. Grid convergence study

A grid convergence study (or grid refinement study) is used to determine the discretization error of a simulation by examining the spatial convergence (δ_G). To perform this study, three grids are created with an increasing refinement, shown in table 6.1. Where the finest grid is preferably limited by the tolerance for grid generation or computational time before converging.

	N_{c_n}	$\frac{H^1_n}{D}$	Number of layers	$\frac{H_n}{D}$
Grid 1	80	$8.78 \cdot 10^{-5}$	45	0.31
Grid 2	120	$8.78 \cdot 10^{-5}$	42	0.21
Grid 3	180	$8.78 \cdot 10^{-5}$	39	0.14

Table 6.1: The three grids that will be used.

For this research the reference grid spacing, that spacifies the grid refinement, is the number of nodes on the circumference of the cylinder $\left(N_{c_n}\right)$. The grid spacing is denoted by h_n with n the grid number. So h_1 for the coarsest grid and h_5 for the finest grid. As shown in table 6.1 the factor between the successive N_{c_n} is 1.5. This factor is called the refinement ratio (r) for the grids. The value of r is higher than the value of 1.1 as recommended by Roache in the book "Verification and validation in computational science and engineering" [36]. When $r > 1.1$ the discretization error can be differentiated from other error sources. The values for h_n can be expressed in h_1 and r by equation 6.4. Where h_1 is determined by $\frac{4\pi D}{N_1}$.

$$h_n = \frac{h_1}{r^{n-1}} \tag{6.4}$$

For the three grids the determined C_d is expanded by a second order asymptotic expansion. This expansion is shown in equation 6.5 per grid. Including the functions a and b, which are independent of the grid spacing h_n.

$$\begin{aligned} C_{d_1} &\sim C_{d_0} + a \cdot h_1 + b \cdot h_1^2 + ... \\ C_{d_2} &\sim C_{d_0} + a \cdot h_2 + b \cdot h_2^2 + ... \\ C_{d_3} &\sim C_{d_0} + a \cdot h_3 + b \cdot h_3^2 + ... \end{aligned} \tag{6.5}$$

Higher order expansion terms are neglected in equation 6.5. C_{d_0} is considered the continuum value at zero grid spacing, here representing the exact value of C_d. The difference between C_{d_0} and C_{d_n} results in the error (E_n) between the exact and the discrete solution.

$$E_n \approx C_{d_n} - C_{d_0} \tag{6.6}$$

Equation 6.6 is an approximation because of the neglect of the higher order terms in equation 6.5 and round of errors. To come to a solution for the second Richardson, the method used to determine C_{d_0}, a is chosen to be 0. Resulting in equation 6.7. To come to equation 6.7 each equation is multiplied by $\frac{1}{h_n^2}$ on both sides. Where the equation for C_{d_3} is also multiplied by -2 on both sides.

$$\begin{aligned} \frac{1}{h_1^2}C_{d_1} &\sim \frac{1}{h_1^2}C_{d_0} + b \\ \frac{1}{h_2^2}C_{d_2} &\sim \frac{1}{h_2^2}C_{d_0} + b \\ -2\cdot\frac{1}{h_3^2}C_{d_3} &\sim -2\cdot\frac{1}{h_3^2}C_{d_0} - 2b \end{aligned} \tag{6.7}$$

The summation of the equations in 6.7 results in equation 6.8 and in the expression for C_{d_0}, in equation 6.9.

$$\frac{1}{h_1^2}C_{d_1} + \frac{1}{h_2^2}C_{d_2} - 2\cdot\frac{1}{h_3^2}C_{d_3} \sim C_{d_0}\left(\frac{1}{h_1^2} + \frac{1}{h_2^2} - 2\cdot\frac{1}{h_3^2}\right) \tag{6.8}$$

$$C_{d_0} \sim \frac{\frac{1}{h_1^2}C_{d_1} + \frac{1}{h_2^2}C_{d_2} - 2\cdot\frac{1}{h_3^2}C_{d_3}}{\frac{1}{h_1^2} + \frac{1}{h_2^2} - 2\cdot\frac{1}{h_3^2}} \tag{6.9}$$

Roache [36] provides a grid convergence index (GCI) to report the result of grid convergence studies. This index can also provide an error band on the grid convergence of the solution. The GCI shows the percentage the computed value of C_d is away from C_{d_0} and thereby shows how the grid would change with further refinement. A small value of the GCI shows therefore that the computation is within the asymptotic range [36]. To determine the GCI the finest grid (h_3) is used, shown in equation 6.11. That the finest grid is used follows from the relative error shown in equation 6.12. In equation 6.11 the order of convergence (p) is not equal to the order of the asymptotic expansion. A fixed value is determined using the Cd values, shown in equation 6.10.

$$p = \frac{ln\left(\frac{Cd_3 - Cd_2}{Cd_2 - Cd_1}\right)}{ln(r)} \tag{6.10}$$

$$GCI_{32} = \frac{F_s|\epsilon_{32}|}{r^p - 1} \tag{6.11}$$

With ϵ the relative error shown in equation 6.12 and F_s a factor of safety recommended by Roache [36] with a value of 1.25.

$$\epsilon_{32} = \frac{C_{d_2} - C_{d_3}}{C_{d_3}} \tag{6.12}$$

Each level of grid refinement should be in a asymptotic range of convergence for the computed solution. The asymptotic range can be checked by evaluating GCI values of multiple grid refinements. For example the two finest grids (6.13).

$$GCI_{32} = r^p GCI_{21} \tag{6.13}$$

The drag coefficients of the three plots are plotted in figure 6.1 together with their filtered values. The Matlab script used to determine the filtered drag coefficient and the GCI values is added in appendix H.

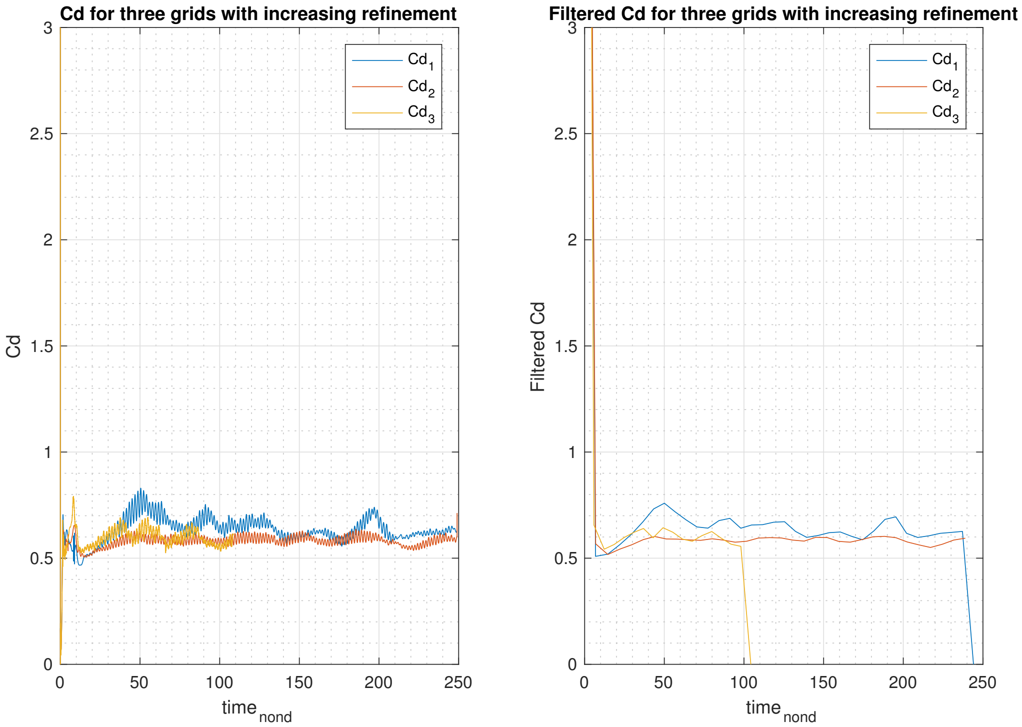

Figure 6.1: Drag coefficients of three grids with increasing refinement; non-filtered and filtered.

The simulation time of grid 3 is shorter then for the other two. This is because the simulation was abruptly stopped after the cluster crashed. Still the data is assumed long enough to be usable. The difference in convergence level is caused by a different number of cores that was used for grid 2. At that time there were 128 cores available where the other two grids were run on 24 cores. A higher number of cores for a simulation results in a more stable simulation. This situation is less ideal to determine the grid convergence but the converged Cd values are not effected, they are only less easy to read. The same solver settings are used for each simulation only the partitioning for each core to run the simulation is different.

The Cd values for each grid are presented in table 6.2.

	$Cd_{converged}$
Grid 1	0.62
Grid 2	0.60
Grid 3	0.59

Table 6.2: Converged Cd for each grid.

The results from the grid convergence study are presented in table 6.3.

p	1.7095
ϵ_{32}	3.23%
ϵ_{21}	1.67%
GCI_{32}	4.03%
GCI_{21}	2.08%

Table 6.3: Results of the grid convergence study.

The solutions are in the asymptotic range of convergence; $GCI_{32} - r^p GCI_{21} < 0.0015$. Therefore the solution may be assumed independent of the grid. The Richardson extrapolation is plotted in figure 6.2.

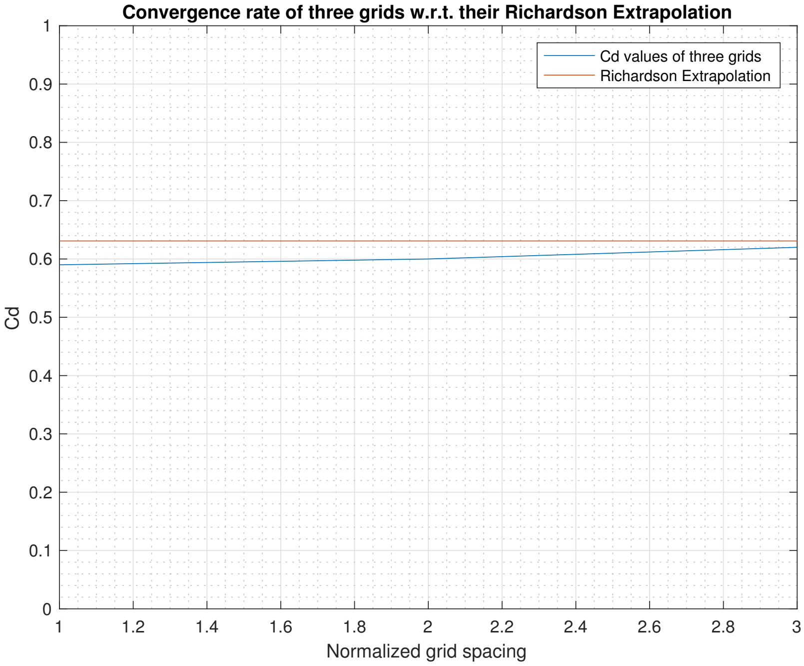

Figure 6.2: Richardson extrapolation and the three tested grids.

The GCI method is used extensively [12] and is recommended by the American Society of Mechanical Engineers (ASME) [6] and the American Institute of Aeronautics and Astronautics (AIAA) [8].

6.1.3. Uncertainty from turbulence modeling

The turbulence model used in this thesis causes uncertainties that are captured in U_{SN}. The uncertainties come forth out of using the right turbulence model for the behavioral aspects of the flow and the choice of the closure parameters. Unfortunately simulations for different turbulence models were not run because of available time on the cluster.

The $\kappa - \epsilon$ turbulence model solves transport equations of the turbulent kinetic energy k and the turbulence dissipation ϵ. Both these parameters determine the eddy viscosity ν_t and replace the Reynolds stresses. For the input parameters of the turbulence model (closure coefficients) commonly accepted values are chosen, this causes uncertainty because of lack of knowledge of the input coefficients. An approach to evaluate this uncertainty is by applying the Markov-chain Monte-Carlo (MCMC) method to i.a. the Bayesion calibrations of the closure coefficients of the turbulence model. The low number of coefficients disregards the issues because of dimensionality. This method is not applied because of time restrictions, the MCMC method is coded but the necessary CFD runs were not executed[1].

6.1.4. Infinite long rotor

During the simulations an infinite long rotor is assumed. As stated on page 35 the height of the rotor should be equal to one correlation length between the lift and drag coefficient. The usage of the right rotor height can be verified by evaluating the three dimensional flow behind the (rotating) rotor for each simulation condition. A periodic flow pattern is expected in the vertical (z) direction. When this is the case the flow coefficients will cancel each other partly out and they will not be over-predicted.

In figure 6.3 the behavior of the flow around a rotor with a height of 3D meter and a spin ratio equal to 2.5 is presented. The flow property in which the flow behavior is expressed is the turbulent kinetic energy (TKE), presenting the turbulent behavior of the flow.

---

[1] The knowledge used for this approach is gained from the lectures of AE4138 *CFD 4: Uncertainty Quantification (2016-2017 Q4)* by R.P.Dwight, TU Delft (2017).

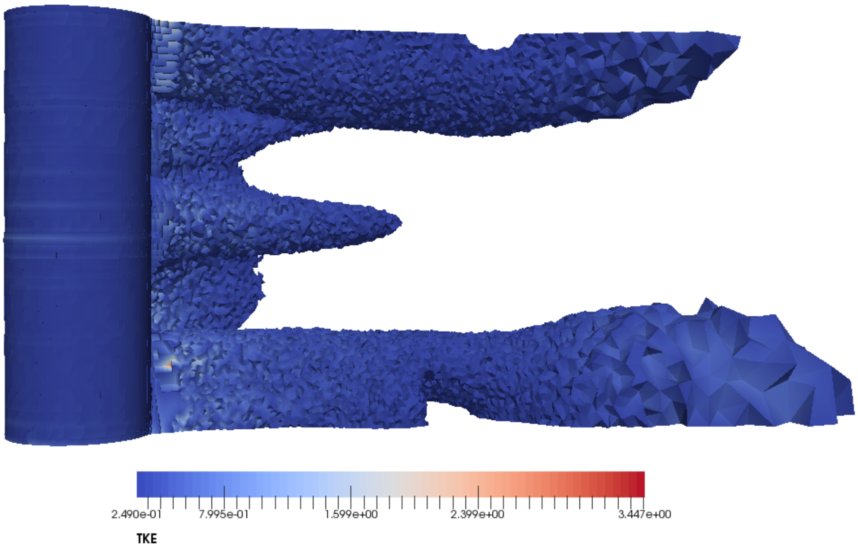

Figure 6.3: Behavior of the flow expressed in TKE around a rotating rotor $SR \sim 2.5$ $t = 4.4s$.

As can be seen in figure 6.3 does the flow nearly have one oscillation period over the rotor height. To validate the correct rotor height simulations need to be performed with the exact same solver and grid settings but a higher rotor. Such a simulation can confirm that the oscillation in figure 6.3 is indeed a full period.

6.2. Validation

The CFD simulations are validated by comparing the resulting flow coefficients to literature and to make an proposal for wind tunnel tests. Validation is defined as a process for assessing simulation modeling uncertainty U_{SN}. The validation based on comparison to other research results is expressed by: $D - \delta_D = S - \delta_S$. With D the data and δ_D the difference between the data and the truth. The comparison error E based on the difference between S and D is expressed as: $E = D - S = \delta_D - \delta_S = \delta_D$. Exact values for E are not presented here because δ_{SMA}, the modeling assumptions, are too different between the compared researches and this thesis.

6.2.1. Literature comparison

The performed CFD simulations can be validated by comparing the flow coefficients of this research to the flow coefficients of already performed researches. Important is to consider the conditions under which the simulations are performed and what their influences on the flow conditions might be.

While evaluating the results of earlier performed researches the following aspects will be taken into account:

1. Dimensionality of the simulation; 2D simulations over-predict the drag coefficient
2. Mirroring of the domain in an axis; the asymmetric flow will be over or under-predicted based on the rotational direction
3. Reynolds number of the performed simulation
4. Spin ratio of the rotor
5. Reliability of the simulation in terms of grid refinement, solver settings and dimensions

The first research to which the results of this thesis are compared is the research by Karabelas et. al. [24].

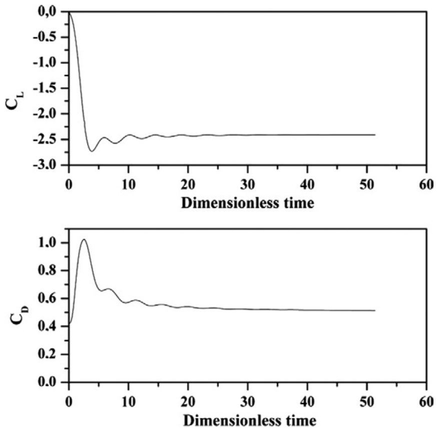

Figure 6.4: Flow coefficients for $SR \sim 2$ and $Re \sim 5 \cdot 10^5$ [24].

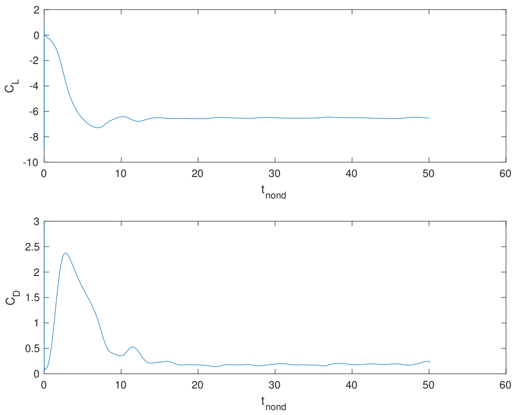

Figure 6.5: Flow coefficients determined for this thesis $SR \sim 2$ and $Re \sim 8 \cdot 10^5$.

The results from this thesis differ from the results of the simulations run by Karabelas et. al. There are a few explanations for these differences and they are listed below.

- The simulations by Karabelas et. al. are performed in 2D; resulting in an overestimation of the drag coefficient
- Karabelas et. al. have included a wall treatment in their simulations; decreasing the Re for which the drag crisis occurs resulting in a higher drag coefficient
- The simulations of Karabelas et. al. are performed for a lower Re ($Re \sim 5 \cdot 10^5$); resulting in a lower lift coefficient

The behavior of the flow is similar, the settling period is the same and for both simulations vortex shedding is eventually suppressed. The peak representing the shedding of the first vortex is slimmer and more symmetrical for the results presented by Karabelas et. al.. Indicating that the detachment of the first vortex occurs smoothly and the drag crisis has occurred for lower SR values. Where for the current research the drag crisis has just occurred. This increases the magnitude of the drag coefficient compared to the drag coefficient obtained in this research. The low values for the lift coefficients obtained by Karabelas et. al. are compared to the research by Craft et. a.[9]. Craft et. al. compare the results of their simulations, for two different turbulence models, to the results by another research by Karabelas[23]. Craft has performed 2D and 3D simulations. The 3D simulations are performed for two different rotor heights, namely 1D and 3D. The results of the research by Craft et. al. are presented in table 6.4.

Simulation	C_L	C_D
2D	5.68	0.150
3D, $\frac{h_{rotor}}{D} = 1$	4.80	0.186
3D, $\frac{h_{rotor}}{D} = 3$	4.80	0.188

Table 6.4: Results of the research by Craft et. al. for a $Re \sim 1.4 \cdot 10^5$ and $SR \sim 2$ [9].

The lift and drag coefficients determined during this thesis are presented in table 6.5. Showing that the results obtained during this thesis differ largely from the 2D URANS simulation results by Karabelas et. al. The over prediction of the drag coeffcient by Karabelas et. al. in figure 6.4 is confirmed by the results of Craft et. al. in table 6.4. Presenting a drag coefficient very similar to the drag coefficient determined in this research for a SR equal to 2.

SR	C_L	C_D
0	0	0.6
1	-2.68	0.31
2	-6.52	0.18
2.5	-8.92	0.22

Table 6.5: Lift and drag coefficients per SR determined during this thesis.

The lift coefficient determined during this thesis is still larger than the lift coefficient determined by Craft et. al.s That is because the values obtained by Craft et. al., presented in table 6.4, are for a rotor with a finite length and an end plate. The lift coefficient for an infinite long rotor resulting from the research by Craft et. al. is presented in figure 6.6. In that figure the results of the current research are plotted with green stars. The lift and drag coefficients obtained during the current thesis are alose presented in figure 6.7.

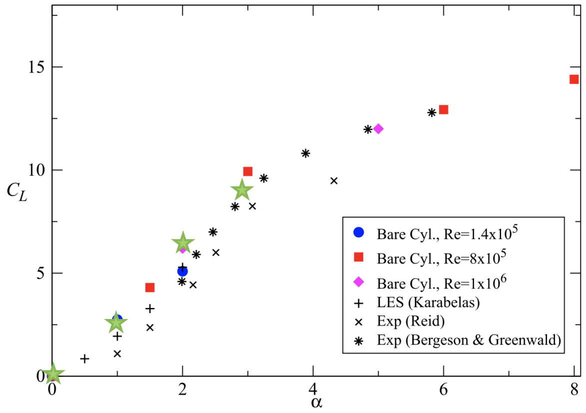

Figure 6.6: TKE of the flow $SR \sim 2$ fully developed flow determined by Craft et. al. [9].

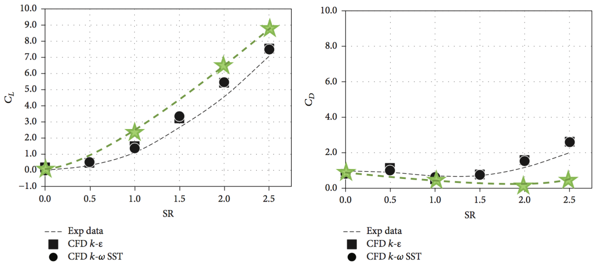

Figure 6.7: TKE of the flow $SR \sim 2$ fully developed flow.[11]

In figure 6.7 the results by the research of De Marco [11] are presented, including the results from the current research. De Marco shows the influence of two turbulence models. The Reynolds number used by De Marco lies around 10^6[2] locating the results after the drag crisis. Explaining why the results presented in this thesis have a lower drag coefficient.

In figure 6.8 and figure 6.9 the flow, expressed in the turbulent kinetic energy, around a rotor with a SR equal to 2 are compared for the same range of TKE.

---

[2] A Reynolds number was not presented by De Marco,. An description of the used spin ratio's contained a flow velocity and diameter, those are used to determine this Re.

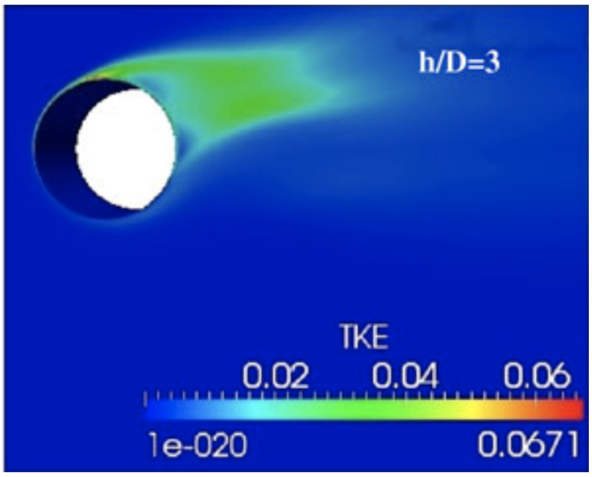

Figure 6.8: TKE of the flow $SR \sim 2$ fully developed flow determined by Craft et. al. [9].

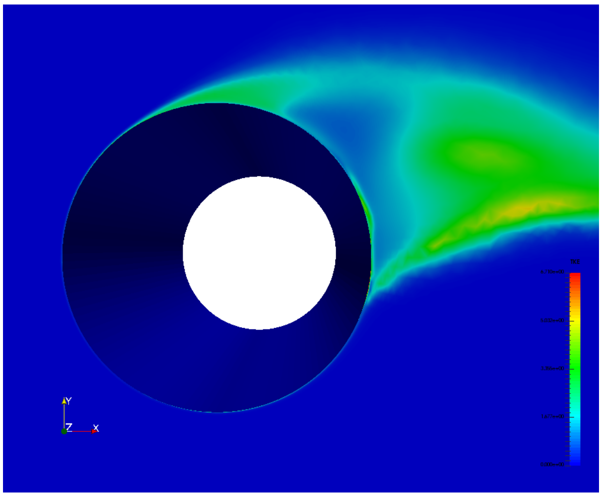

Figure 6.9: TKE of the flow $SR \sim 2$ fully developed flow.

The direction of the wake is different because the moment in time at which the image created by Craft et. al. is not known. The level of TKE corresponds and the behavior of the flow close to the rotor surface does as well.

The results presented in this thesis lay within an acceptable range with respect to the results by Craft et. al., the experimental data from Reid, Bergeson & Greenwald and the results by De Marco. Concluding that there are no reasons to not accept the results by the CFD simulations.

6.2.2. Proposal for wind tunnel tests

The importance of wind tunnel tests to validate the simulations is that it is the only way to test the physical truth before actually building a Flettner rotor. Flettner rotors have been build but performance data is not made available. The proposal is added in Apendix I on page 121.

6.2.3. Multiple simulation runs

To assure that there were no mistakes during the execution of the simulations all simulations are rerun on anther day. The simulations were not rerun for their complete time interval but only for the first 1.6 seconds, when the flow coefficients show converged behavior. There was not enough computational time to rerun all the simulations for their full time span. The results differed with a maximum of 0.5% of the initial run and were therefore accepted.

7

Results

In this chapter the results will be presented so that in the next chapter (page 95) the research question, introduced on page 3, can be answered. Like the methodology the results will be presented in two parts, one for each part of the research question.

First the results will be presented that are used to answer the question *"What is the influence of the implementation of a Flettner rotor on an Exploration cruise vessel with respect to the roll motion?"*. To answer this part of the research question the external moment by the Flettner rotor and RAO plots will be presented and discussed.

Thereafter the results to answer the question *"What is the influence of the implementation of a Flettner rotor on a Exploration cruise vessel with respect to the superstructure-rotor interaction?"* will be presented. Those results contain the flow coefficients and flow behavior around the (rotating) rotor, determined with CFD simulations. While performing CFD simulations the resulting flow coefficients indicated the occurrence of a drag crisis. This was considered to be relevant enough for the implementation of a Flettner rotor to step outside the scope and be discussed in this chapter. The observations leading to the finding of the drag crisis are included in this part of the results and will be presented per rotational speed, before discussing the rotor superstructure interaction.

7.1. Influence Flettner rotor on roll motion

In this section the following external and damping moments are presented:

- External moment by one Flettner rotor
- External moment by two bilge keels determined in two ways:
  1. Estimated as explained on page 25
  2. Determined as 3% of the critical damping
- Damping moment of only the hull of the vessel; resulting from the HydroD calculations
- Critical damping moment of the vessel; resulting from the HydroD calculations

The external moment caused by the Flettner rotor is added to the damping moment of the vessel to evaluate the influence of the implementation of a Flettner rotor. The same is done for the two bilge keels. These moments are examined for the natural frequency of roll of the vessel, where resonance can occur.

When the potential of the Flettner rotor to damp the vessel is estimated its effect will be quantified and evaluated for all wave frequencies.

7.1.1. Influence of the Flettner rotor on the damping moment

In chapter 4 is explained that only the external moment by the Flettner rotor dependent on the roll velocity; $M_{FR}\left(\dot{\phi}\right)$ is considered. The roll velocity of the vessel is determined for the 59 wave frequencies that are also used to calculate the equation of roll motion in HydroD. The roll angle and velocity equations are presented by equation 7.1, where $\phi_a = 5°$.

$$\begin{aligned}\phi &= \phi_a \cos\left(\omega_w \cdot t\right) \\ \dot{\phi} = \frac{\partial \phi}{\partial t} &= -\phi_a \omega_w \sin\left(\omega_w \cdot t\right)\end{aligned} \tag{7.1}$$

.

For each wave frequency the harmonic external moment, caused by the Flettner rotor (M_{FR}), and the damping moment of the vessel (M_B) can be determined. The M_{FR} and M_B are presented in figure 7.1. These plots are made for the wave frequency nearly equal to the natural frequency of the vessel; $\omega_w = \omega_0 = 0.325 \frac{rad}{s}$.

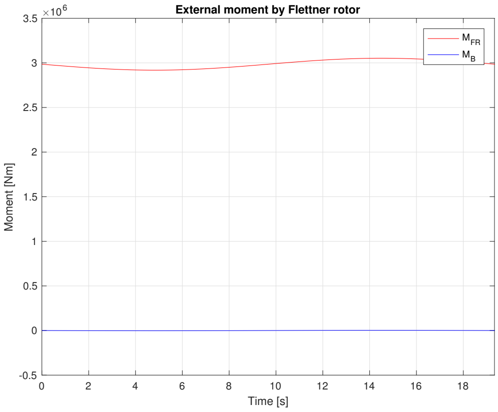

Figure 7.1: External moment by the Flettner rotor and the damping moment of the vessel for $\omega_w = 0.325 \frac{rad}{s}$ and $\phi = \phi_a = 5°$ at $t = 0$.

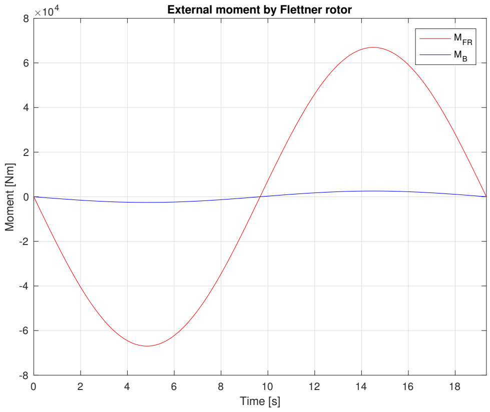

Figure 7.2: External moment by the Flettner rotor minus its mean and the damping moment of the vessel for $\omega_w = 0.325 \frac{rad}{s}$ and $\phi = \phi_a = 5°$ at $t = 0$.

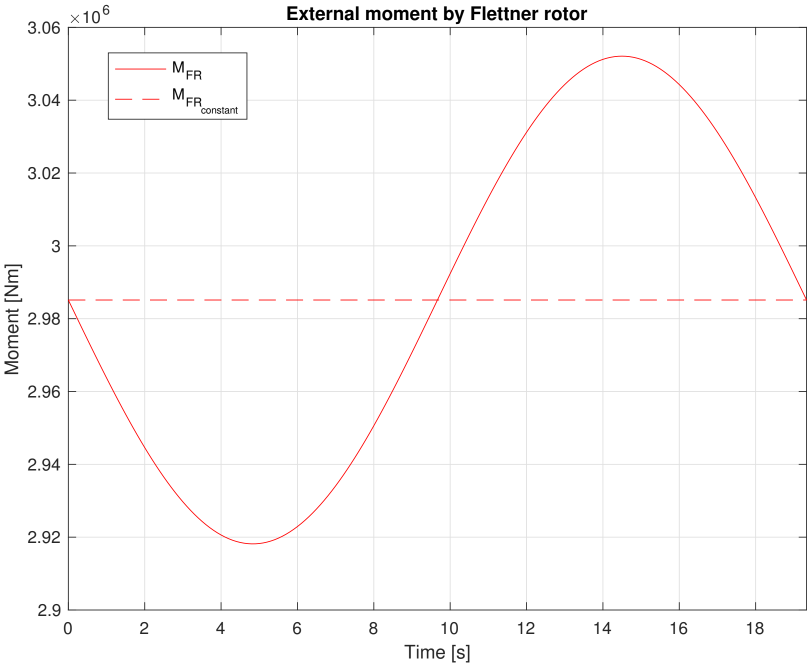

Figure 7.3: External moment of the Flettner and its constant component for $\omega_w = 0.325 \frac{rad}{s}$ and $\phi = \phi_a = 5°$ at $t = 0$.

From figure 7.1 it can be seen that M_{FR} consists out of a constant moment $\left(M_{FR_{constant}}\right)$ and a oscillating component$\left(M_{FR_{oscillating}}\right)$. This is because the flow around the Flettner rotor is build up out of the sailing velocity, wind velocity and the velocity because of the roll motion. These velocities and their directions are explained on page 12. The sailing and wind velocity are constant over time and cause the constant component in M_{FR}. This constant moment is equal to $2.99 \cdot 10^6\ Nm$ at the natural frequency. In figure 7.2 M_{FR} is subtracted by $M_{FR_{constant}} + M_{FR_a}$[1] so that it oscillates around zero. In that way other properties of M_{FR} can be evaluated with respect to the damping moment of the vessel. M_{FR} does not have a phase difference with respect to the damping moment of the vessel because both their oscillations are dictated by the roll velocity of the vessel. The amplitude of the oscillating component of the external moment by the Flettner rotor is 6.8 times larger than that of the damping moment of only the vessel hull.

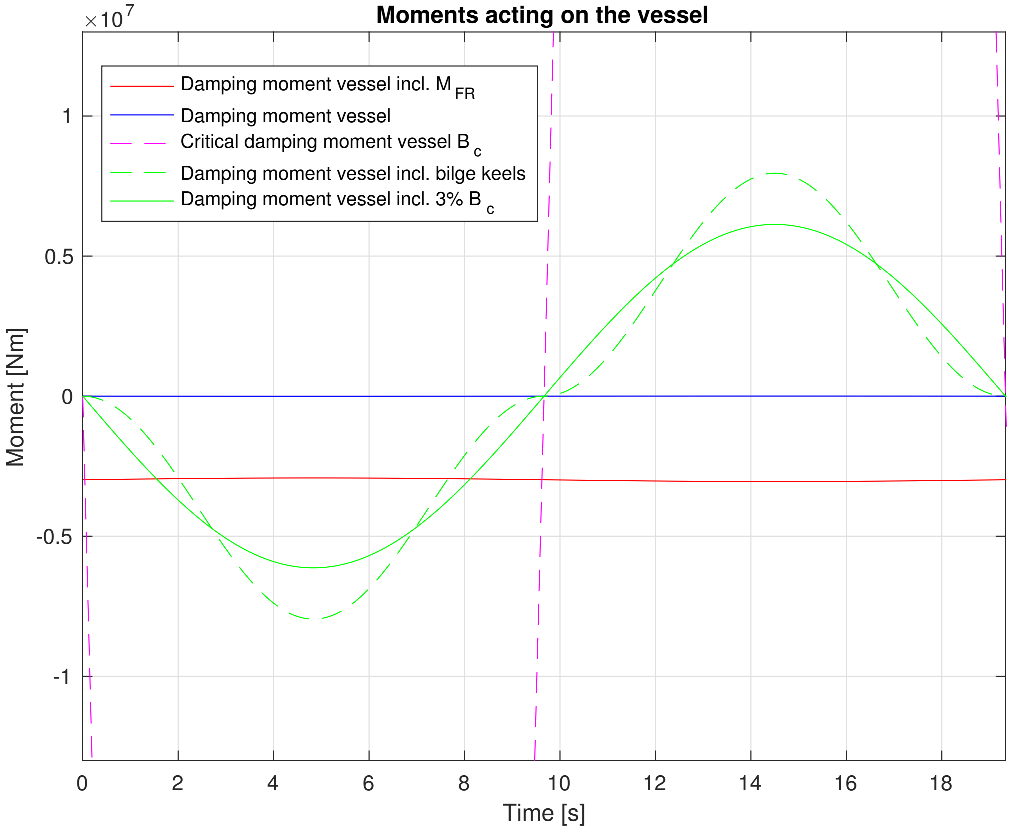

Figure 7.4: Damping moment vessel incl. external moment of the Flettner, the critical damping moment of the vessel and the damping moment vessel incl. two bilge keels for $\omega_w = 0.325 \frac{rad}{s}$ and $\phi = \phi_a = 5°$ at $t = 0$.

In figure 7.4 all the external moments are shown that are considered in this thesis together with the critical damping of the vessel. The critical damping of the vessel is so large that not its complete amplitude is captured in the image. Figure 7.4 shows the relative magnitude of the oscillation of M_{FR}, which is small. The amplitude of M_{FR} is larger than the amplitude of M_B but small compared to the amplitude of the damping moment by the bilge keels.

In the determination of the load on the bilge keels the absolute flow velocity because of the roll motion is squared. Explaining the difference in shape w.r.t. the other moments (dashed green line in figure 7.4).

---

[1] M_{FR_a} represents the amplitude of the oscillation of the external moment caused by the Flettner rotor displayed in figure 7.9.

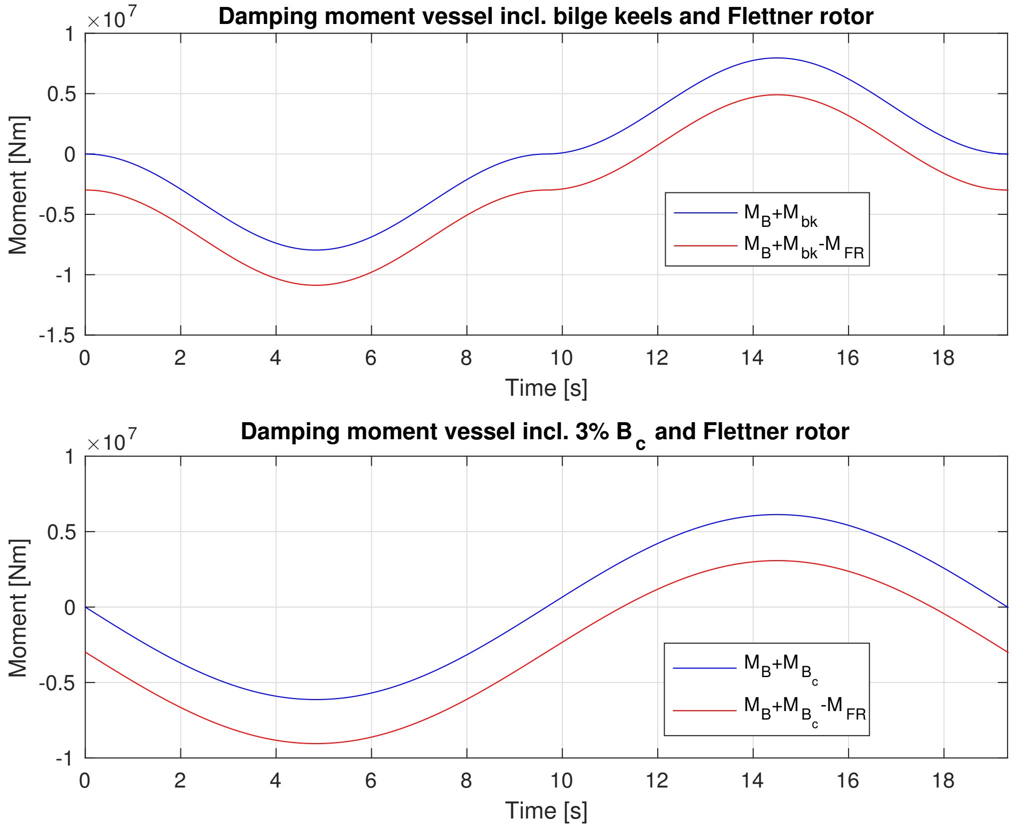

Figure 7.5: Damping moment vessel incl. external moment of the Flettner rotor and two bilge keels for $\omega_w = 0.325\frac{rad}{s}$ and $\phi = \phi_a = 5°$ at $t = 0$.

The external moment by the Flettner rotor cannot be considered to be a damping moment. When it would be considered as an damping moment it would always be positive and fluctuate in magnitude. As is tried to display using figure 7.3; the fluctuation in magnitude is expressed by M_{FR} and the constant moment by $M_{FR_{constant}}$.

In figure 7.5 the damping moment of the vessel is presented together with the damping moments of the bilge keels (M_{bk}). The influence of the Flettner rotor is shown with the dashed lines. The influence of the oscillating component of M_{FR} is small and only the constant component is visible. In figure 7.6 the amplitudes of $M_{FR_{oscillating}}$ and $M_B + 3\% B_c$ are presented to show their relative magnitude.

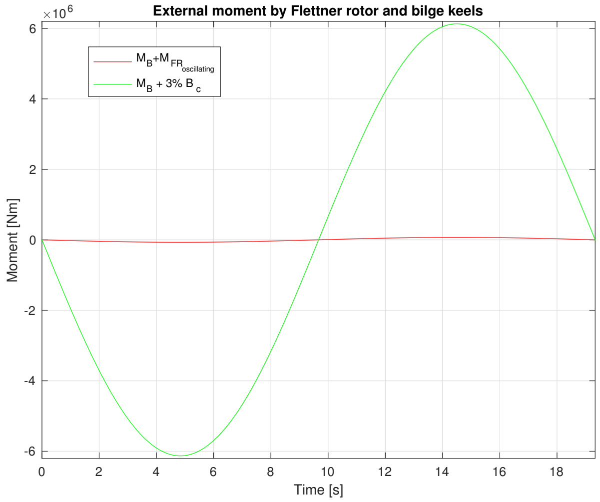

Figure 7.6: Damping moment vessel incl. external moment of the Flettner rotor and 3%B_c for $\omega_w = 0.325\frac{rad}{s}$ and $\phi = \phi_a = 5°$ at $t = 0$.

The independence of the constant component of M_{FR} on the roll velocity/acceleration makes it possible to compare it to the restoring moment of the vessel (equation 7.2). The constant component of M_{FR} does not act as an restoring moment rather as an constant moment acting on the vessel.

$$C_{44}\phi = M_{FR_{constant}} \tag{7.2}$$

For the natural frequency and $\phi_a = 5°$ this results in a $\phi \sim 3.30°$ because of $M_{FR_{constant}}$.

Conclusion

The influence of the Flettner rotor on the damping moment of the vessel is dictated by the wind velocity and sailing speed. Those flow velocities cause a constant moment by the Flettner rotor on the vessel. This constant moment is dependent on the magnitude of those flow velocities and on their direction. In figure 7.7 the dependence of the external moment by the Flettner rotor is shown dependent on the direction of the incoming wind velocity μ (defined in figure 2.6 on page 12).

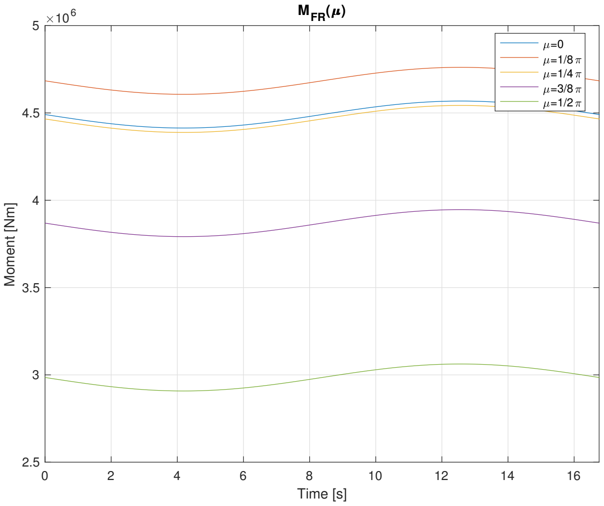

Figure 7.7: External moment of the Flettner rotor dependent on μ for $\omega_w = 0.325\frac{rad}{s}$ and $\phi = \phi_a = 5°$ at $t = 0$.

The flow velocity around the Flettner rotor because of the roll motion causes an oscillation of its magnitude, which is small compared to the influence of bilge keels. There is no phase difference w.r.t. the damping moment of the vessel.

By implementing the Flettner rotor on the cruise vessel the constant moment should be considered. Based on the sailing and wind velocity countermeasures can be taken such as creating an counter-moment by ballast tanks.

The ballast tanks needed to create this counter-moment need to present on both sides of the vessel. The size of the tanks are estimated to be 3 meter long, broad and high. When the ballast tanks present in the vessel cannot provide this volume, the volume is considered small enough to not deliver design problems.

In the next section only the oscillating part of M_{FR} is considered. When a Flettner rotor is implemented on a cruise vessel and causes a constant heeling angle this angle will always be compensated. To evaluate the implementation of the Flettner rotor a realistic situation needs to be researched.

7.1.2. Influence of the Flettner rotor on the RAO of roll

The Response Amplitude Operators (RAO's) presented in this chapter display the ratio between the amplitude of the roll motion and the amplitude of the waves. The RAO's are expressed per wave frequency, 59 waves are used. An RAO plot is made by connecting its discrete values, presented for each wave frequency. This results in a plot that can differ significantly when more wave frequencies are used.

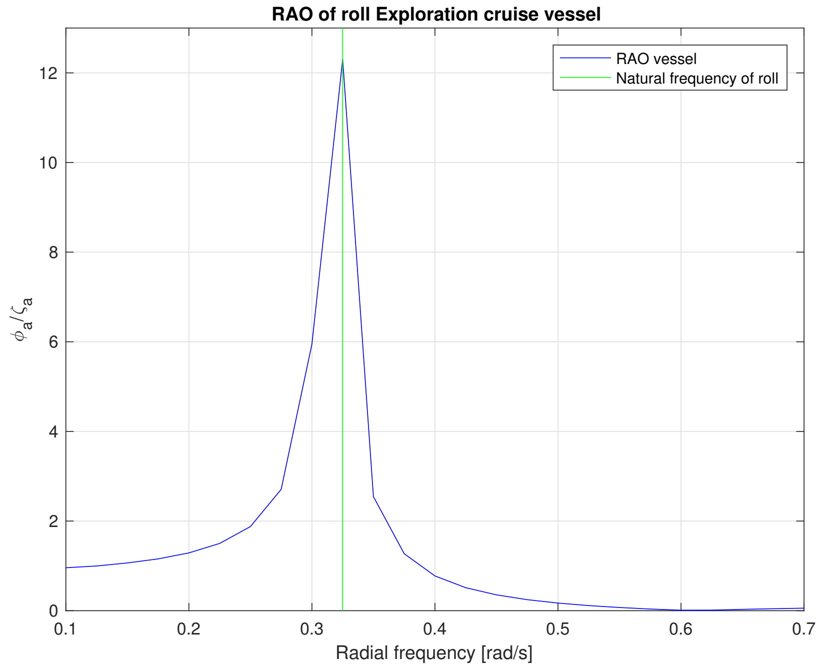

Figure 7.8: RAO of the Exploration cruise vessel.

The RAO of roll of the Exploration cruise vessel is plotted in figure 7.8 together with the natural frequency of the vessel. The peak of the RAO is located around the natural frequency of the vessel, to avoid resonance for the roll motion. Around the natural frequency of the vessel the damping term of the equation of motion has the largest influence.

In this section the influence of the Flettner rotor implementation will be evaluated based on the RAO of the cruise vessel with and without the external moment by the Flettner rotor. Of M_{FR} only the oscillating component is included, as presented in figure 7.9. The oscillating component is determined using equation 7.3.

$$M_{FR_{oscillating}} = M_{FR} + M_{FR_a} - M_{FR_{constant}} \tag{7.3}$$

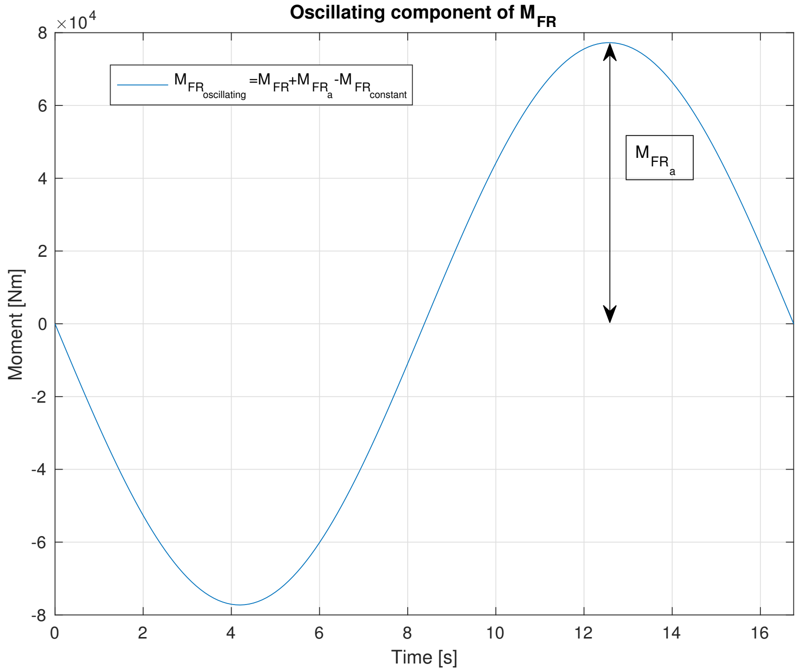

Figure 7.9: The oscillating component of the external moment by the Flettner rotor (M_{FR}) for $\omega_w = 0.325\frac{rad}{s}$ and $\phi = \phi_a = 5°$ at $t = 0$.

Where M_{FR_a} is indicated with a black arrow in figure 7.3. $M_{FR_{osc}}$ is expressed against time because it is dependent on the roll velocity. To include the $M_{FR_{osc}}$ in the RAO the amplitude of $M_{FR_{osc}}$ is determined per wave frequency. The $M_{FR_{osc}}$ shown in the RAO represents therefore the maximum influence of the Flettner rotor.

The constant component of M_{FR} is not included in the RAO because that moment places the vessel under an angle independent of time. That moment will be compensated by ballast tanks or other methods.

The RAO's of the vessel include 3% of the critical damping to present a realistic image of the vessel behavior. Because $M_{FR_{osc}}$ and M_B do not have a phase difference the natural frequency of the vessel is not expected to change because of the implementation of the Flettner rotor. Three other RAO's are determined, namely including 3% of the critical damping, including $M_{FR_{osc}}$ ans a combination of both which are displayed in figure 7.10. The influence of the damping properties are small but present. The peak of the RAO of the vessel is decreased by 4.6% after the implementation of the Flettner rotor. This can directly be related to the roll amplitude at the natural frequency for the same ζ_a. This is depicted in figure **??**. The bare and smooth hull used to determine 'RAO vessel' is not representative for the industry, therefore 3% B_c is included in the 'RAO vessel incl. 3% B_c' in figure 7.10.

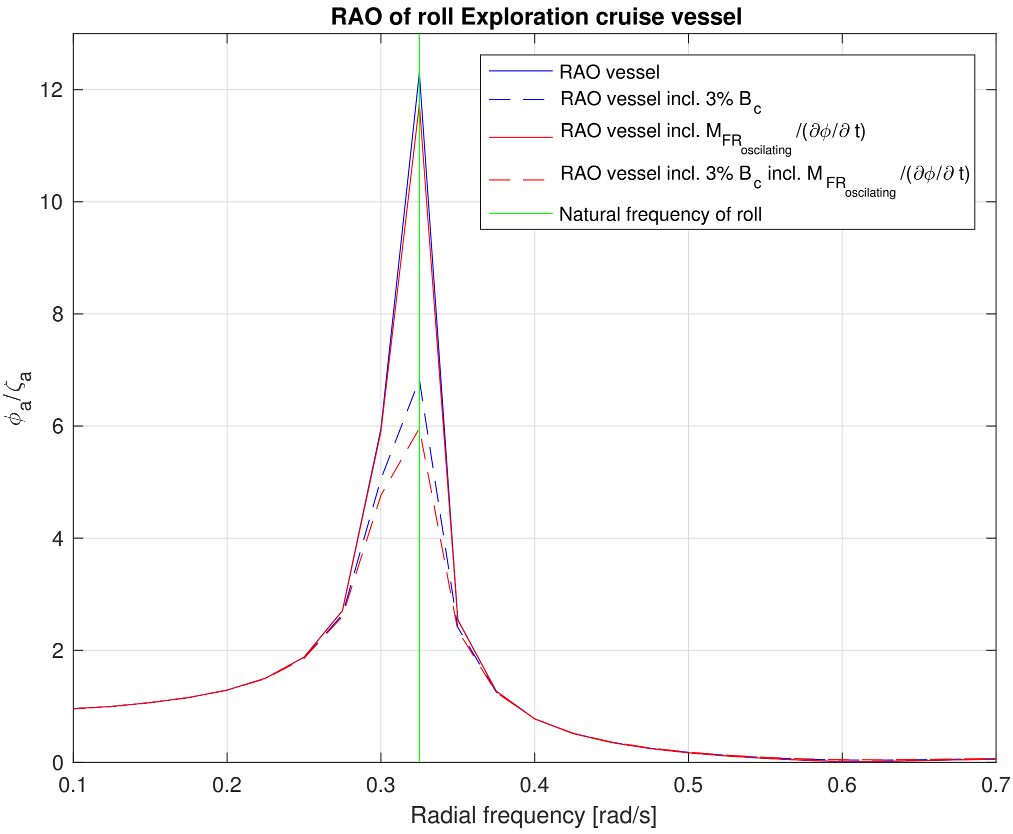

Figure 7.10: RAO of the Exploration cruise vessel incl. 3% critical damping and $M_{FR_{oscilating}}$.

The difference between the RAO vessel incl. 3% B_c with and without $M_{FR_{osc}}$ is larger than without 3% B_c. This is because the constant value of $M_{FR_{osc}}$ for ω_0 is larger compared to the RAO of the vessel incl. 3% B_c for ω_0. The RAO including 3% B_c is 12.71% larger than the RAO including both.

Quantification of damping properties

In the previous section is was concluded that the the oscillating part of the moment by the Flettner rotor can assist in the damping of the roll motion. This conclusion is reached for the condition that the roll motion is excited around the natural frequency of the vessel. To quantify the damping effect of the rotor the occurrence of this condition needs to be estimated and evaluated for other sea states. This is done by evaluating the RAO with respect to the sea state presented in section 2.3.1 on page 11. At the end of this section it will be clear how large the influence of the Flettner rotor is on the damping of the vessel for all wave frequencies.

The sea state will be expressed by a wave spectrum[2], namely the JONSWAP spectrum. The JONSWAP spectrum assumes that waves are never fully developed and is the most common spectrum used in the industry. The JONSWAP spectrum is displayed in figure 7.14 together with the RAO of the vessel.

---

[2] A wave spectrum represents the distribution of wave energy among different wave frequencies, corresponding to wavelengths, on the sea surface.

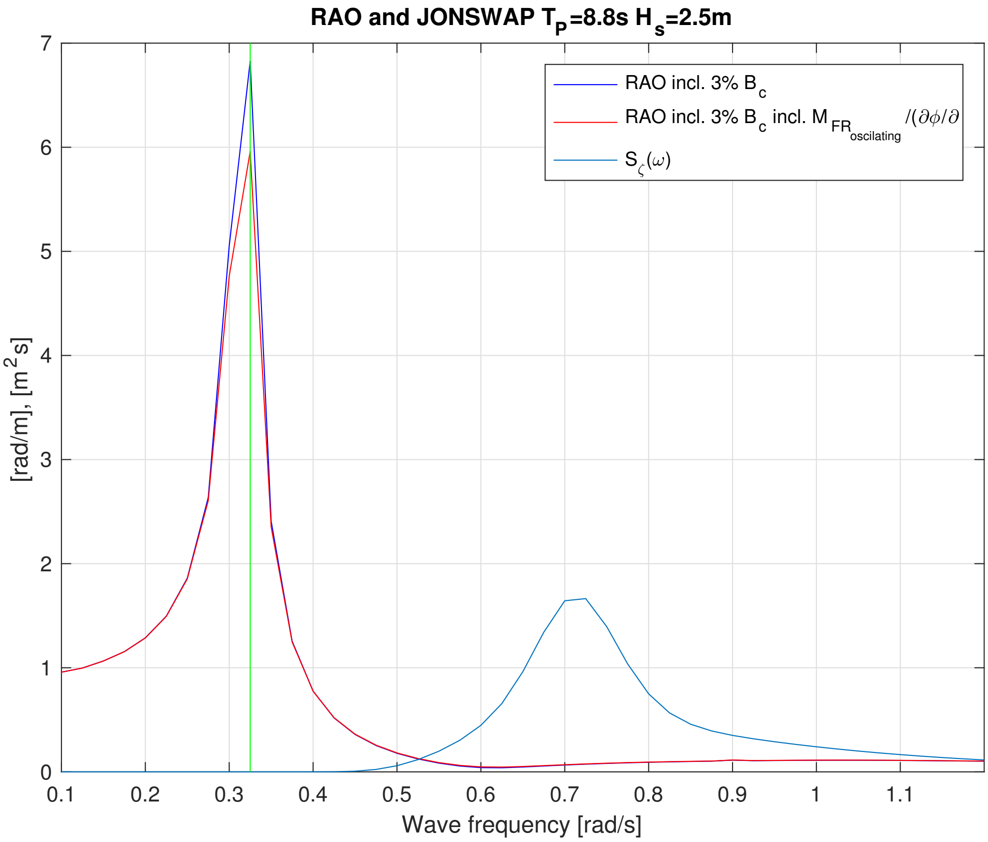

Figure 7.11: RAO of the Exploration cruise vessel incl. 3% critical damping and the JONSWAP spectrum of sea state.

The natural frequency of the vessel is located outside the wave spectrum to decrease the chance of resonance; $S_\zeta(\omega_0) = 3.25 \cdot 10^{-6}\ m^2 s$. This indicates that the probability of occurrence, of the conditions for which the damping by the Flettner rotor is optimal, are small. This is evaluated by determining the response spectrum of roll motion (S_ϕ), presented in equation 7.4 and figure 7.12.

$$S_\phi(\omega) = \left|\frac{\phi_a}{\zeta_a}(\omega)\right|^2 \cdot S_\zeta(\omega) \tag{7.4}$$

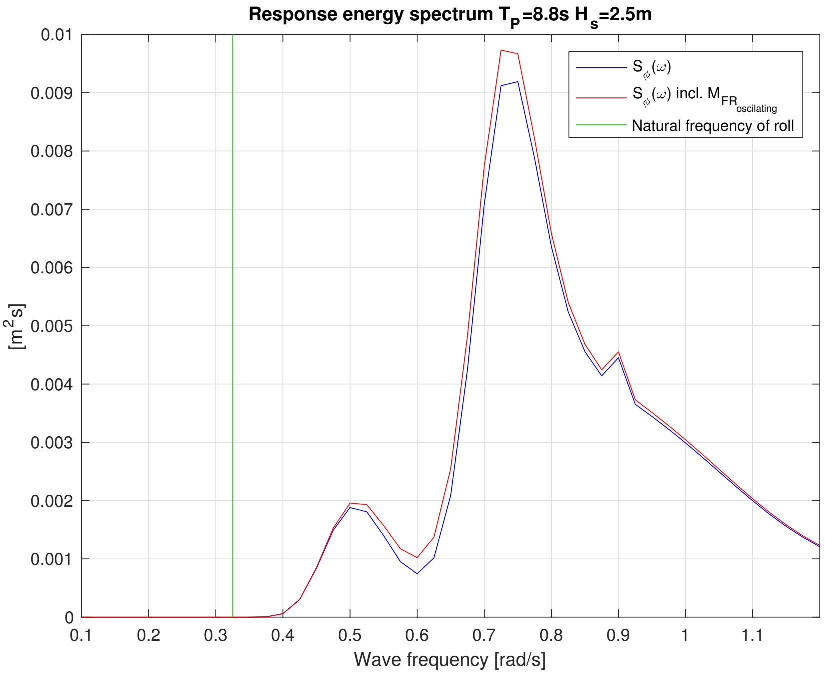

Figure 7.12: Response spectrum of the roll motion for the presented sea state with and without influence of M_{FR}.

The values of $S_\phi(\omega_0)$ are presented in table 7.1.

$S_\phi(\omega_0)$	$9.43 \cdot 10^{-10}$	$m^2 s$
$S_\phi(\omega_0)$ incl. $M_{FR_{oscillating}}$	$7.1848 \cdot 10^{-10}$	$m^2 s$

Table 7.1: Values at ω_0 of the response spectrum of the roll motion.

In figure 7.12 $S_\phi(\omega_0)$ including $M_{FR_{oscillating}}$ is larger than without $M_{FR_{oscillating}}$ for the higher wave frequencies. This is due to the RAO's, from $\omega_w = 0.4\frac{rad}{s}$ the RAO including $M_{FR_{oscillating}}$ is larger than the RAO without.

When the frequency of the roll motion increases the contribution of $M_{FR_{oscillating}}$ to the damping coefficient increases as well. In the RAO $M_{FR_{oscillating}}$ is included for its maximum values, namely its amplitude for each wave frequency. This causes $M_{FR_{oscillating}}$ to increase for increasing ω_w. The effect of the increasing damping coefficient because of the Flettner rotor is larger for the numerator (equation 7.5) in the RAO formula than for the denominator (equation 7.6). This is because the mass term is so large that it overshadows the increasing effect of the damping coefficient.

This effect is enlarged because the RAO's are squared and multiplied with the JONSWAP spectrum to determine the response energy spectrum. The JONSWAP spectrum has only larger positive values in the frequency range where the inertia terms of the RAO are dominant; the high frequency range.

$$e^{kT}\sqrt{\left(C_{44} - A_{44}\omega^2\right)^2 + \left(B_{44}\omega\right)^2} \tag{7.5}$$

$$e^{kT}\sqrt{\left(C_{44} - \left(A_{44} + M\right)\omega^2\right)^2 + \left(B_{44}\omega\right)^2} \tag{7.6}$$

To indicate the chance of a specific roll amplitude for both RAO's and the presented sea state a Rayleigh distribution is used to determine their probability density functions (f). The probability density function is determined following equation 7.7.

$$f\left(\phi_a\right) = \frac{\phi_a}{m_{0_\phi}} \exp\left(\frac{-\phi_a{}^2}{2m_{0_\phi}}\right) \tag{7.7}$$

With m_{0_ϕ} the zero order moment of the roll response spectrum. The probability density function $f\left(\phi_a\right)$ for the roll amplitude in the given sea state is presented in figure 7.13.

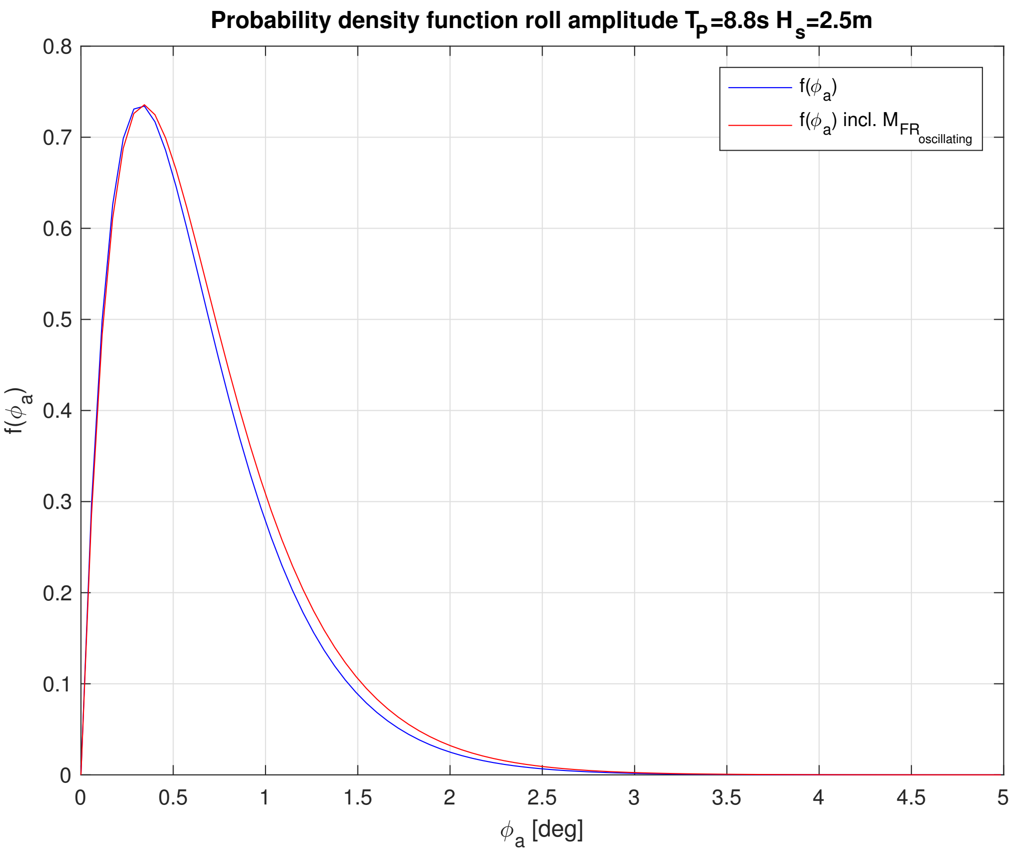

Figure 7.13: Probability density function $f\left(\phi_a\right)$ for the roll amplitude for the presented sea state $\left(T_p = 8.8s\ H_s = 2.5m\right)$.

Showing that the probability density function of the roll amplitude shifts to the right when $M_{FR_{oscillation}}$ is included in the equation of motion. Indicating that after the implementation of the Flettner rotor, for the chosen sea state, the chance of larger roll angles of the vessel increases. This is also shown back in the significant roll angle $\left(\phi_{a_s}\right)$ presented in table 7.2.

ϕ_{a_s}	1.6030°
ϕ_{a_s} incl. $M_{FR_{oscillating}}$	1.6440°

Table 7.2: Significant roll angles for $T_p = 8.8s\ H_s = 2.5$.

Around the natural frequency is the effect of $M_{FR_{oscillating}}$ the largest. The maximum influence of $M_{FR_{oscillating}}$ is evaluated by choosing a sea state with the peak period equal to the natural period. The corresponding wave height is 2.5m. This is a sea state that will probably never occur but does indicate the effect of the Flettner rotor on the damping around the natural frequency.

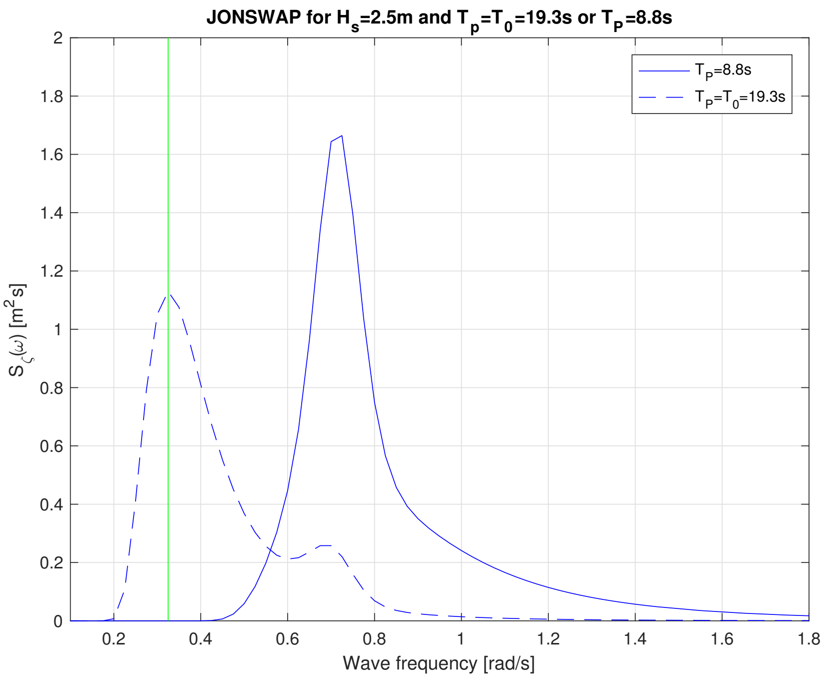

Figure 7.14: JONSWAP wave spectrum for $T_p = 8.8$ or T_0 and $H_s = 2.5m$ or $H_s = 2.5m$.

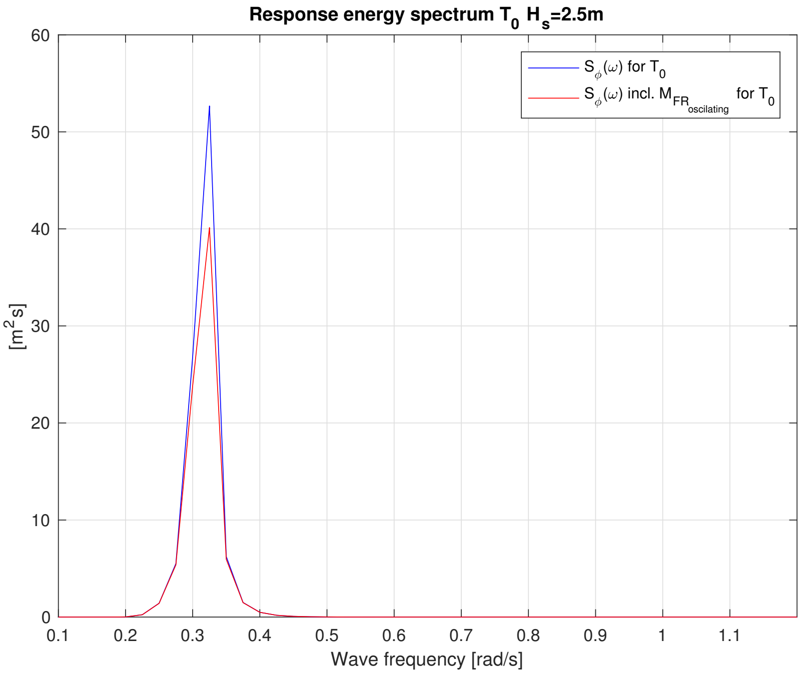

Figure 7.15: Response spectrum of the roll motion (T_0 and $H_s = 2.5m$) with and without influence of M_{FR}.

For this sea state the damping coefficient, of the equation of motion, dictates the response energy spectrum. Therefore the influence of $M_{FR_{oscillating}}$ increases on the spectrum as can be seen in figure 7.15 and in table 7.3.

ϕ_{a_s}	3.09°
ϕ_{a_s} incl. $M_{FR_{oscillating}}$	2.82°

Table 7.3: Significant roll angles for T_0 $H_s = 2.5m$.

Before presenting the conclusions for this section it is important to present the estimations that are made while calculating the moments and RAO's:

1. The roll frequency of the vessel is assumed to be the same as the wave frequency; neglecting phase differences and interaction between the vessel and the waves
2. The influence of $M_{FR_{oscilating}}(t)$ is assumed to be equal to its amplitude for each wave frequency
3. The used equation of motion is linear, neglecting non-linear damping components
4. A limited amount of wave frequencies are used to compose the RAO; more frequencies could result in deviating results

These estimations are made to provide an indication of the influence of the Flettner rotor on the roll motion in the available time span. Small variations in the results should therefore be evaluated with these estimations in mind.

Conclusion
The sailing and wind velocity cause the Flettner rotor to induce a constant heeling moment on the vessel. This heeling moment by the Flettner rotor can be compensated by, for example, ballast tanks. The placement of these tanks is determined to not cause problems for the arrangement of the cruise vessel.

The flow velocity around the Flettner rotor, created by the roll motion, causes the rotor to induce a moment that fluctuates in time. The amplitude of that moment is small compared to the effect of bilge keels but large enough to effect the damping of the vessel when the vessels rolls with its natural roll period; decreasing the significant roll angle by 0.27°. The chance that the vessel encounters a wave that will excite the vessel around it natural frequency is very small. For more probable sea states the Flettner rotor has a small negative contribution to the damping of the vessel; the significant roll angle varies only 0.04° based on the conditions considered in this thesis. The calculation methods used contain linearizations that render such small differences in the significant roll angle negligible.

Leading to the conclusion that the influence of the implementation of the Flettner rotor on the damping of the roll motion is negligible for roll frequencies higher than. When the vessel rolls around its natural frequency the Flettner rotor will assist in damping the vessel.

In this section the results of the Computational Fluid Dynamic (CFD) simulations will be presented and discussed with as goal to quantify the superstructure-rotor interaction. While performing the CFD simulations the drag crisis was observed for increasing spin ratios (SR). The drag crisis influences the load excited by the Flettner rotor and for that reason the scope was extended to include a flow evaluation for the simulated SR.

Before the results of the simulations are presented the way in which they will be presented is explained. This explanation consists out of the lay out of the images, terminology and the points on which the flow will be evaluated. This is done before the results are presented to improve readability.

When the presentation of the results is clear the simulations will be presented per simulation set up, summed up underneath.

1. Rotating rotor
    (a) $SR \sim 0$
    (b) $SR \sim 1$
    (c) $SR \sim 2$
    (d) $SR \sim 2.5$
2. Rotating rotor with object in wake

The results of the CFD simulations will be compared with each other and eventually with the rotor with an object in its wake.

The rotors will first be evaluated on their behavior during the settling period. With the settling period the time span is meant from $t \sim 0s$ until the flow is fully developed. During that period the behavior of the flow is explained based on the development of the flow coefficients. Thereafter the fully developed flow is described per SR, containing an evaluation of the three dimensional flow around the rotors.

At the end of the sections conclusions will be drawn on how the behavioral aspects of the flow influence the implementation of a Flettner rotor and the interaction between rotor and superstructure.

7.1.3. Presentation style of results

The rotors used in the simulations are expressed in their spin ratio (SR). In all the figures the flow coefficients will have their SR as subscript to show which rotational velocity they represent.

The flow coefficients are expressed in the non-dimensional time $t_{nond} = t \cdot \frac{U_\infty}{D}$, with t the time in s, U_∞ the undisturbed flow velocity in $\frac{m}{s}$ and D the diameter of the rotor in m. All the rotors rotate in counter clockwise direction except for the rotor with the superstructure in its wake.

Image lay out

The axis definition used to indicate the position of a figure in the total domain is shown in figure 7.16 and 7.17. In figure 7.17 the terminology used to indicate positions of flow phenomena is indicated.

Images like figure 7.17 show the top view of the three dimensional domain and include the eye of the rotor.

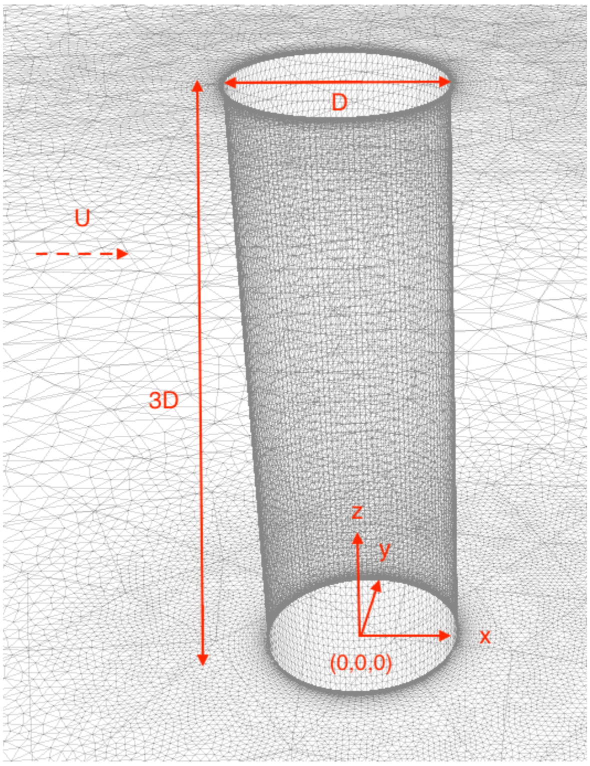

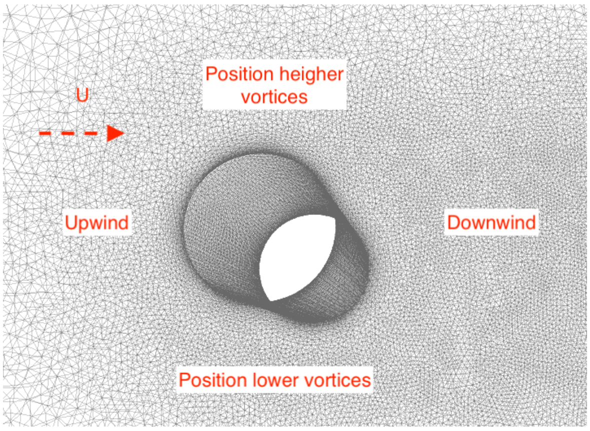

Figure 7.17: Axis definition rotor top view.

Figure 7.16: Axis definition rotor side view.

The legends of the figures are added in appendix J to improve readability.

The available visual data is saved every 0.05s for the non-rotating rotor ($SR \sim 0$) , for the rotating rotors ($SR \sim 1-2.5$) every 0.025s. This limits the moments in time for which visual results can be presented.

Terminology

Three units will be used to typify the flow around the rotor:

- Turbulent kinetic energy (TKE); the mean kinetic energy per unit mass associated with eddies and turbulence in the flow [$\frac{m^2}{s^2}$]
- Velocity; the flow velocity around the rotor [$\frac{m}{s}$]
- Pressure; the pressure in flow around the rotor [$\frac{N}{m^2}$]

Flow evaluation points

As stated in the introduction of this section a flow description around the rotor will be included in the results. In the next paragraphs the phenomena with which the flow is described and evaluated, will be explained.

The first phenomena is vortex shedding. The formation of vortexes behind rotors with different SR typify the flow characteristics and influence the behavior of the load excited by the rotor.

Vortex formation is induced by the increasing instability of a shear layer in the boundary layer of the rotor. Turbulence causes the instability of the shear layer. Local velocities dictate the Reynolds number and thus the level of turbulence, relating different rotational velocities of rotors to different flow phenomena around the rotors.

The transition point and stagnation point are two points in the boundary layer of the rotor which will be used to explain, for example, the formation of vortexes. The transition point indicates the point in the boundary layer where the flow goes from laminar to turbulent. The stagnation point of the flow indicates the point where local velocities go to zero.

The laminar sublayer close to the surface of the rotor also has velocities that are going to zero. This sublayer is however considered to be nonexistent in the evaluation of the flow behavior[3], because it is a side effect of the simulation method and does not exist in reality. The laminar sublayer will influence the magnitude of the flow coefficients, especially when shear stresses near the boundary should increase the drag coefficient. Therefore the sublayer will be considered when the flow coefficients are discussed.

The researches presented in chapter 3 indicate the necessity of three dimensional simulations to include the three dimensional viscous effects in the wake and on the rotor surface. To capture these effects the distribution of TKE is used and will be presented in images over the height of the rotor.

7.1.4. Settling period

To explain and compare the flow around the rotors for different SR the flow is evaluated at four moments in time, indicated in the flow coefficient plots in figure 7.18 and figure 7.19. The moments in time for which the flow is evaluated are $0.05s$, $0.2s$, $0.4s$ and $0.6s$.

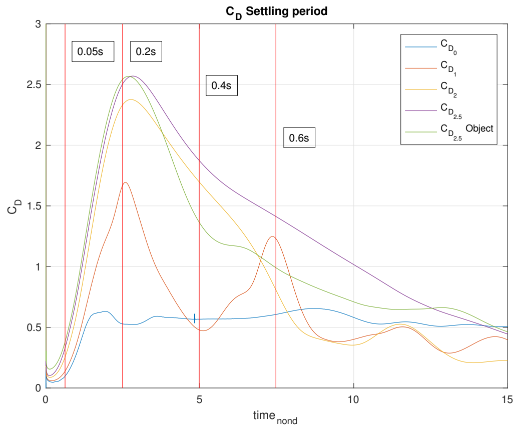

Figure 7.18: Drag coefficients for the four rotational rates expressed in the non-dimensional time.

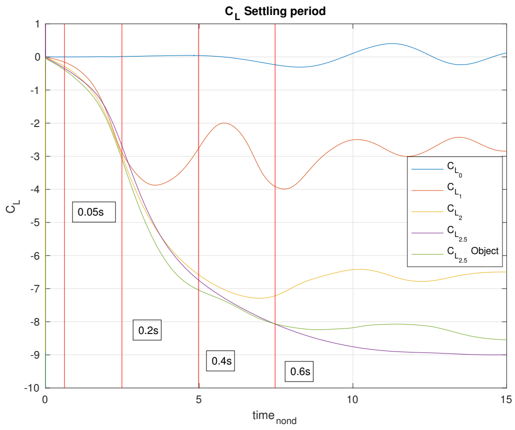

Figure 7.19: Lift coefficients for the four rotational rates expressed in the non-dimensional time.

---

[3] The laminar sublayer is a very thin layer close to the surface of the rotor caused by the no-slip condition. The level of turbulence outside the laminar sublayer, in the rest of boundary layer, will indicate the actual level of turbulence on the rotor surface.

The plots of the flow coefficients show that the settling time of all the rotational rates is nearly the same, around $t_{nond} = 20 \sim 1.6s$. The flow after $t_{nond} = 20$ is considered to be fully developed. The behavior of the flow around the rotors for the rotational rates is different during the settling period.

7.1.5. Spin ratio equal to 0

In this section the non-rotating rotor will be discussed representing a non-rotating Flettner rotor. This rotor can also be compared to the cylinder, representing the superstructure, in the simulation containing the rotor-superstructure interaction.

Settling period

In figures 7.99, 7.100, 7.101 and 7.102 on page 90 the flow velocity around a non-rotating rotor is shown for $t \sim 0.05s$, $0.2s$, $0.4s$ and $0.6s$. These images will be used to explain the behavior of the the flow coefficients during the settling period. The flow develops symmetrical around the x-axis because of the non rotational properties of the rotor.

Around $t \sim 0.05$ the drag coefficient starts to grows because the instabilities in the detaching shear layers are growing. The two shear layers collapse before $t \sim 0.2$ and the two vortexes move with the flow velocity further away from the rotor, decreasing the drag coefficient.

While growing in size the two vortexes interact with each other and move again closer to the rotor; increasing the drag coefficient. The velocity around the non-rotating rotor in the vertical direction is shown in figure 7.115 on page 91. It can be seen that the position of the two vortexes varies slightly in y-direction but that there are no large deviations. To confirm this the pressure distribution is plotted in figure 7.119 on page 92. The pressure distribution is shown around the rotor for $t \sim 0.4$.

The asymmetrical pressure distribution on the surface of the rotor shows the first stages of the development of the Karman vortex street. The three dimensional pressure distribution on the rotor surface is presented in figure 7.123 on page 93, showing the rotor in dark gray and the pressure of the flow around it in blue. This three dimensional representation confirms that there are no large variations in the xy-plane in vertical direction. To conclude that the behavior of the flow is constant over the height of the rotor the level of turbulence needs to be evaluated as well, which will be done in the next section.

The TKE around the rotor in the xy-plane is shown in figure 7.20, the vectors show the density of the TKE and thus in which direction the TKE changes. The width of the wake is nearly identical to the diameter of the rotor and is similar to the width of the wake shown at $t \sim 0.6$ shown in figure 7.102.

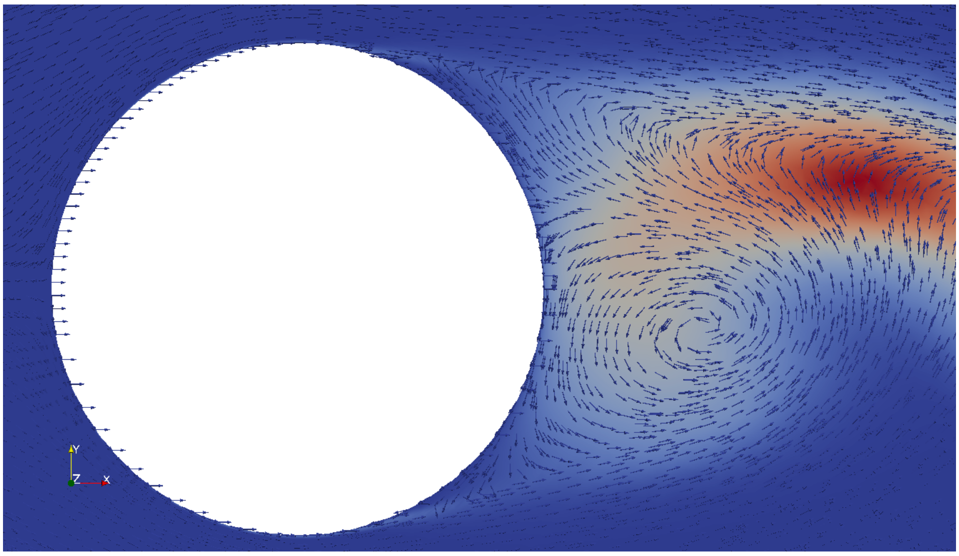

Figure 7.20: Cross-section of the flow around the rotor with the density of the TKE expressed in vector form (TKE $t = 10s$ $SR \sim 0$ $z = 2D$).

Around $t \sim 0.75s$ the first vortex detaches, developing an Karman vortex street. The St number, typifying the frequency with which vortexes are shed, is equal to $St \sim 0.28$.

Fully developed flow

The distribution of the turbulent kinetic energy over the height of the rotor is presented in figures 7.25, 7.21 and 7.22 for a fully developed flow. The three dimensional TKE is presented in $\frac{m^2}{s^2}$. The levels of TKE are displayed on the surfaces of the grid between the vertices, these surface can be seen in figure 7.17[4] By presenting these three dimensional images the behavior of the TKE can be evaluated over the height of the rotor. Corresponding to figures 7.115 and 7.123 the TKE seems to be evenly distributed over the height of the rotor. In figure 7.22 the cross-section of the wake is presented in the xy-plane. Here, again, a nearly even distribution of the lower values of the TKE is shown over the height of the rotor. The higher values of TKE are located in the middle of the wake and are not constant distributed over the height of the rotor.

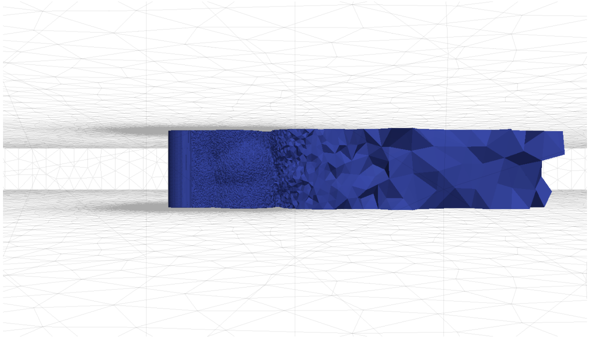

Figure 7.21: TKE $t = 10s$ $SR \sim 0$.

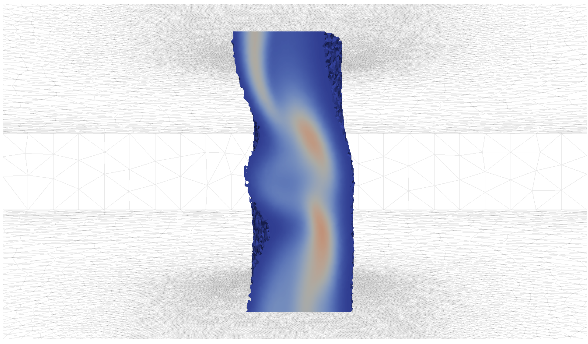

Figure 7.22: TKE $t = 10s$ $SR \sim 0$ $x = 1.5D$.

To show the behavior of the higher levels of TKE in the wake cross-sections are presented in the xy-plane in figures 7.23 and 7.24. In figure 7.25 the top-view is presented at the same moment in time. From these figures it can be seen that the intensity and orientation of the TKE in the wake does differ over the height of the rotor.

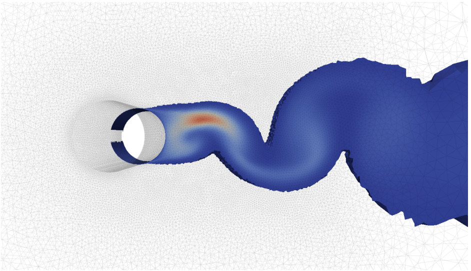

Figure 7.23: TKE $t = 10s$ $SR \sim 0$ $z = 1D$.

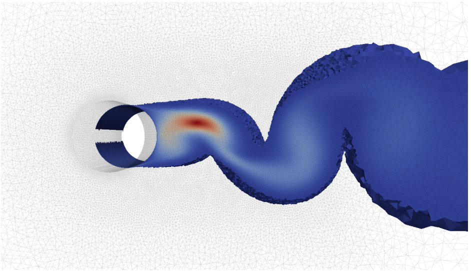

Figure 7.24: TKE $t = 10s$ $SR \sim 0$ $z = 2D$.

The highest levels of TKE are present in the wake behind the rotor and not in the shear layers in the boundary layer. The shear layer closest to the rotor surface is still laminar, containing no shear stresses induces by turbulence. The drag coefficient is totally defined by the turbulence in the wake.

---

[4] Showing the decrease in refinement outside of the refinement zone.

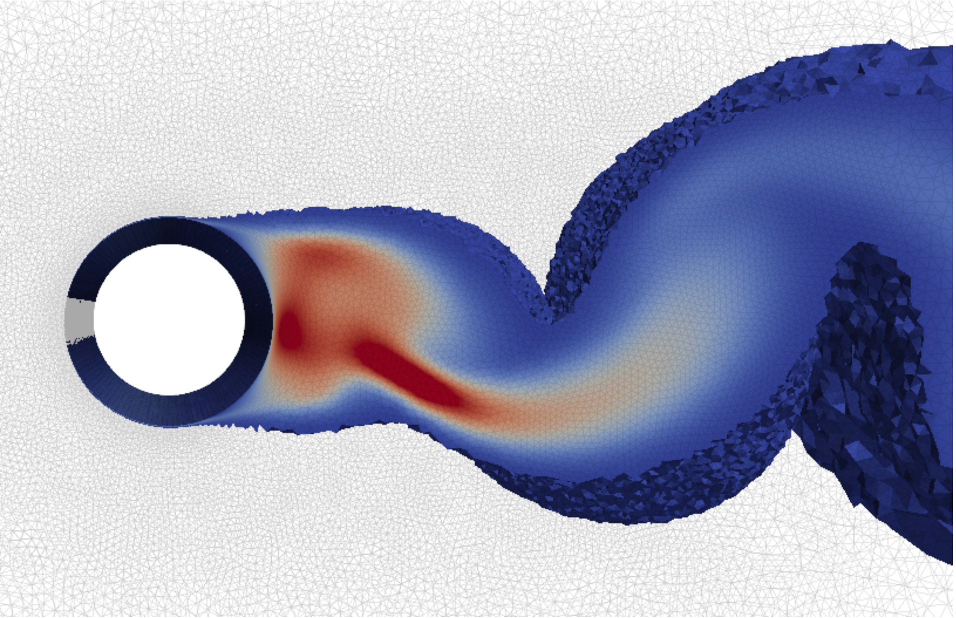

Figure 7.25: (TKE $t = 10s$ $SR \sim 0$).

Flow coefficients

The lift coefficient varies around zero as is expected of a non rotating rotor and the drag coefficient is determined to be equal to 0.6. The frequency with which the St is determined in section 7.1.5 is based on the frequency of the lift coefficient, representing the vortex shedding frequency. The frequency of the drag coefficient is twice that of the lift frequency, representing the alternating detaching shear layers.

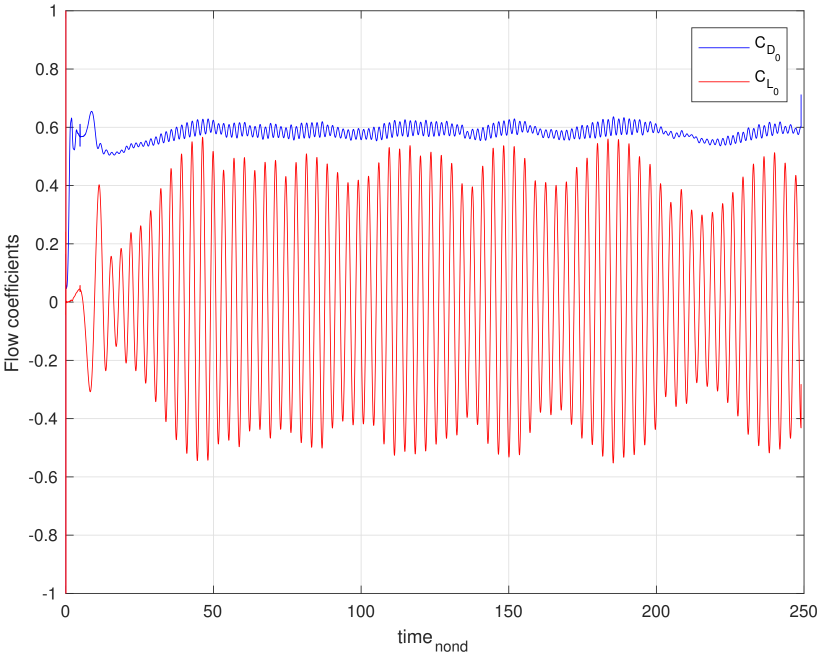

Figure 7.26: Flow coefficients of the rotor with a $SR \sim 0$ expressed in the non-dimensional time.

Concluding

A non-rotating rotor with flow conditions as described in chapter 2 will develop a Karman street by shedding vortexes with a fixed frequency. The first vortex is shed around $t \sim 0.9s$. The peak in the drag coefficient, caused by the shedding of that vortex, is small compared to the rotors with higher SR (figure 7.18).

The drag coefficient is fully determined by the turbulence in the wake and the alternating detachment of shear layers. The lift coefficient is defined by the alternating pressure distribution on the surface of the rotor because of the wake. The magnitude of total load excited by a non-rotating Flettner rotor will be dominated by drag for its magnitude, the frequency will be governed by the vortex shedding frequency.

The settling period of both flow coefficients for this SR develops smoothly, even though the undisturbed flow velocity does not increase with a ramp at the beginning of the simulation. When the Flettner rotor is implemented on the cruise vessel, changes in the apparent wind will therefore not induce peaks in the excited loads.

When the apparent wind is fully developed the wake behind the non-rotating Flettner rotor will contain high levels of turbulence that vary in direction over the height of the rotor. These high levels of turbulence are not found close to the surface of the rotor. The high levels of turbulence stretch over a length of 3 times the diameter of the rotor and have a width of approximately 1 diameter. Because the rotor does not rotate the wake, and thus the higher levels of turbulence, are located in the same direction as the apparent wind. When a superstructure is located in that area it will experience shear stresses because of the high turbulence levels in the flow and fluctuating loads over its height.

When a superstructure is placed in the wake of the rotor it may be beneficial to let the rotor rotate with a low rotational velocity to reduce the levels of turbulence in the wake.

7.1.6. Spin ratio equal to 1

The behavior of the flow around a rotor rotating with the same speed as the undisturbed flow velocity ($SR \sim 1$) will be evaluated in this section.

Settling period

In figures 7.103, 7.104, 7.105 and 7.106 on page 90 the flow around the rotor with a $SR \sim 1$ is shown. The flow will no longer be symmetrical around the x-axis because of the rotational velocity of the rotor. The velocity distribution in z-direction in the vortex shed at $t \sim 0.2$ is shown at $t \sim 0.4$ in figure 7.116. It appears that the velocity is uniform distributed with respect to the rotor height.

Similar to the rotor with a $SR \sim 0$, the shear layers are detaching around $t \sim 0.05$ for the rotor with a $SR \sim 1$. Resulting from the rotational speed the "lower" shear layer detaches slower than the "higher" shear layer and attaches to the "higher" detaching shear layer. Resulting in a vortex that is located higher and detaches faster than for a rotor with a $SR \sim 0$. The first peak in figure 7.18 is caused by the build up of turbulence near the rotor, before the vortex is shed. When the vortex is shed and moves away from the rotor, the drag coefficient decreases again. In the same way the third shear layer attaches to the fourth as is shown in figures 7.27, 7.28 and 7.29.

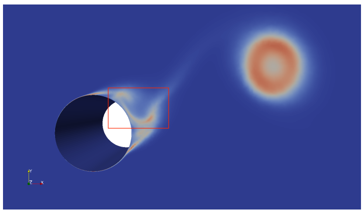

Figure 7.27: TKE $t = 0.375s$ $SR \sim 1$.

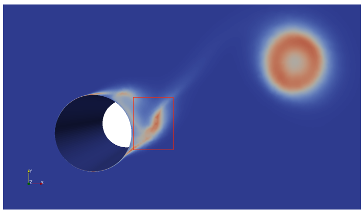

Figure 7.28: TKE $t = 0.4s$ $SR \sim 1$.

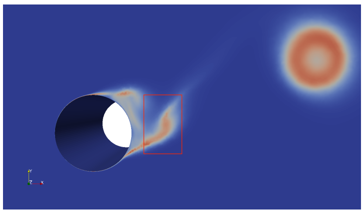

Figure 7.29: TKE $t = 0.425s$ $SR \sim 1$.

The vortex resulting out of those two shear layers is shed and another vortex starts to form in the same manner as the first vortex did. The vortexes resulting from the "higher" located detaching shear layer are of higher intensity causing the two peaks in the drag coefficient plot (figure 7.30). The vortexes resulting from the detachment of the "lower" shear layers have a lower turbulence level. They do not cause a peak for the drag coefficient but induce a local increase of the coefficient in between $t \sim 0.4$ and $t \sim 0.6$.

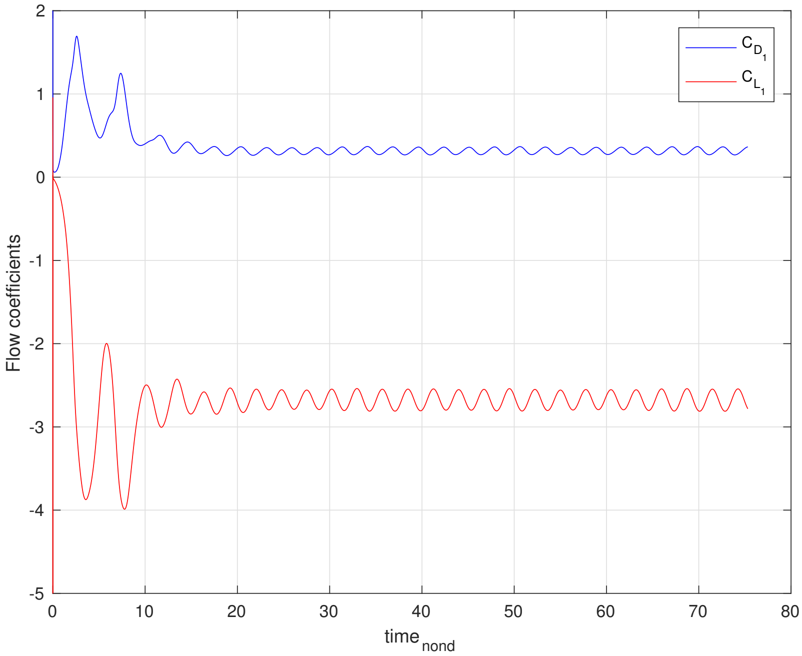

Figure 7.30: Flow coefficients of the rotor with a $SR \sim 1$ expressed in the non-dimensional time.

Fully developed flow and flow coefficients

For the fully developed flow the level of turbulence is equal for both the "higher" and "lower" detaching shear layers. As can be seen in figure 7.30, lift and drag coefficients are out of phase and have the same frequency. The frequency results in a $St \sim 0.36$ for the fully developed flow.

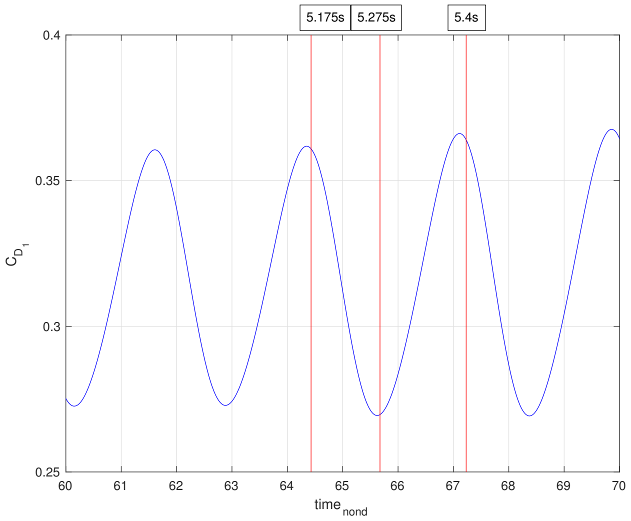

Figure 7.31: Drag coefficient for $SR \sim 1$ expressed in the non-dimensional time..

In figure 7.31 a vortex shedding period is presented of the fully developed flow around a rotor with a $SR \sim 1$. In figure 7.32 upto figure 7.37 the flow is visualized expressed in its TKE in three cross-sections.

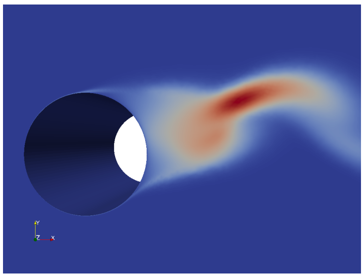

Figure 7.32: TKE $t = 5.175s$ $SR \sim 1$ ($z = 3D$).

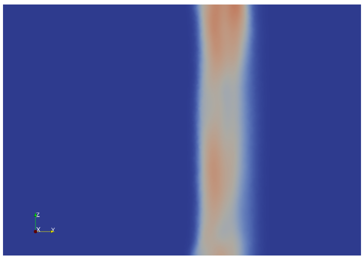

Figure 7.33: TKE $t = 5.175s$ $SR \sim 1$ ($x = D$).

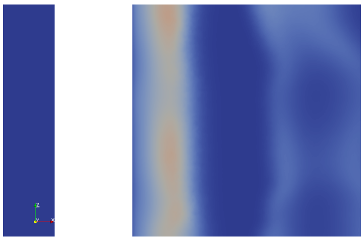

Figure 7.34: TKE $t = 5.175s$ $SR \sim 1$ ($y = 0$).

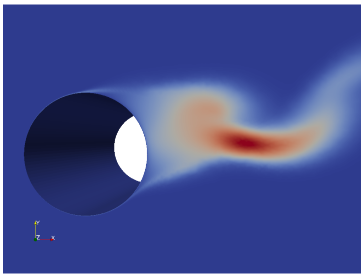

Figure 7.35: TKE $t = 5.275s$ $SR \sim 1$ ($z = 3D$).

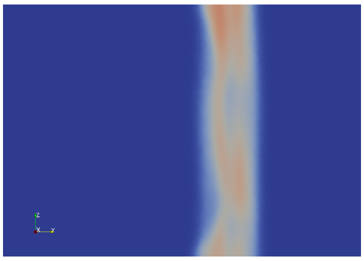

Figure 7.36: TKE $t = 5.275s$ $SR \sim 1$ ($x = D$).

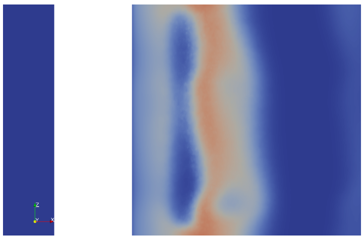

Figure 7.37: TKE $t = 5.275s$ $SR \sim 1$ ($y = 0$).

The transition points where the shear layer become unstable are no longer symmetrical in the x-axis because of the rotational velocity. They stay in the same place during a vortex shedding cycle, keeping the width of the wake constant. The TKE is maximal located away from the rotor decreasing to the surface of the rotor, indicating that the drag is fully dominated by the vortex shedding behavior. In figure 7.35 the stagnation point behind the rotor can be seen and the narrowing of the wake with respect to a rotor with a $SR \sim 0$.

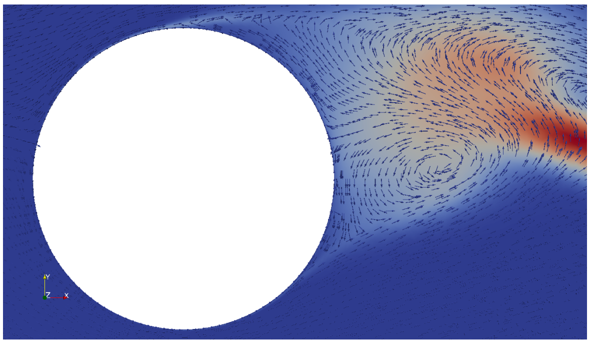

Figure 7.38: Cross-section of the flow around the rotor with the density of the TKE expressed in vector form (TKE $t = 5.275s$ $SR \sim 0$ $z = 2D$).

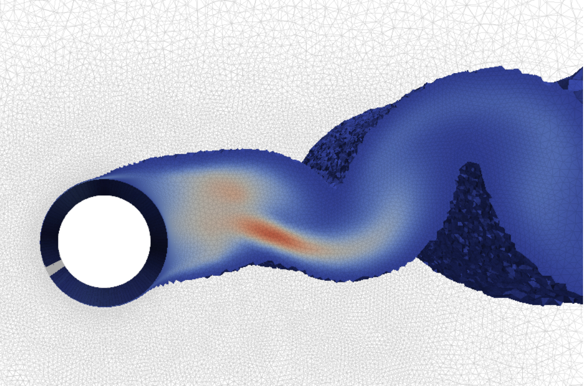

Figure 7.39: TKE $t = 5.275s$ $SR \sim 1$.

The boundary layer close to the surface of the rotor is laminar, containing no shear stresses that influence the drag on the rotor.

Figure 7.34 and figure 7.37 show that the intensity of the TKE only differs over the height of the rotor. The orientation of the intensity of the TKE in the wake does not differ like for a rotor with a $SR \sim 0$.

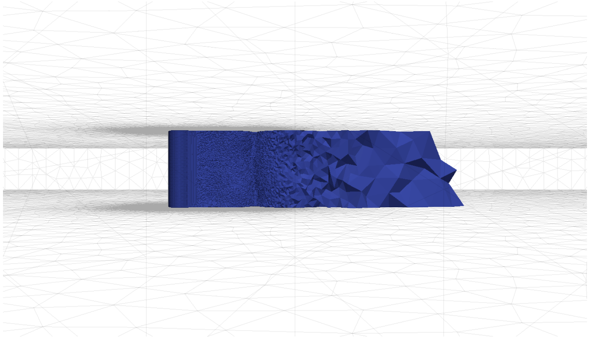

Figure 7.40: TKE $t = 5.275s$ $SR \sim 1$.

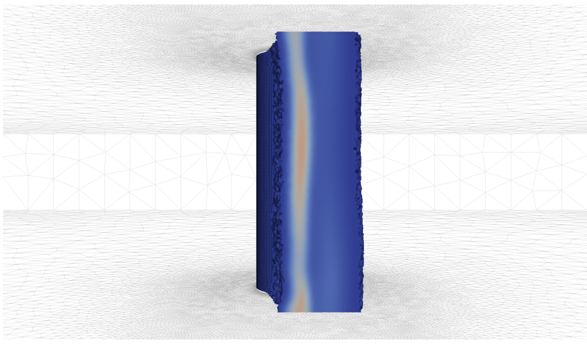

Figure 7.41: TKE $t = 5.275s$ $SR \sim 1$ $x = 1.5D$.

Figures 7.39, 7.40 and 7.41 confirm that the fluctuations in TKE are only in local intensity. The shape of the three dimensional TKE, shown in figure 7.39, 7.40 and 7.41, shows that the low values of TKE are nearly uniform distributed over the height of the rotor. The TKE on the surface of the rotor is nearly even distributed with respect to the rotor height.

Concluding

A Flettner rotor with a $SR \sim 1$ will periodically shed vortexes formed by the fusion of detaching shear layers. During the settling period the detaching shear layers at either side of the rotor deviate in magnitude, resulting in two peaks for the drag coefficient. Indicating that when the Flettner rotor is rotating changes in the apparent wind should occur smoothly to not induce peaks in the produced drag and changes in the direction of the total load.

The load excited by a Flettner rotor, with a SR equal to 1, will for its magnitude be dominated by the produced lift. Behind the rotor a vortex street is present resulting in a fluctuation of the excited load by the rotor. The frequency of that fluctuation is higher than for a non-rotating Flettner rotor but the amplitude is smaller.

The wake behind the Flettner rotor is not in line with the apparent wind direction because of the rotational velocity of the rotor. Compared to the Flettner rotor with a SR equal to 0 the wake becomes slimmer and the high levels of TKE in the wake decrease. The high levels of TKE do also not fluctuate in direction over the height of the rotor, they do fluctuate slightly in magnitude. The flow around a Flettner rotor with this rotational velocity is more stable than for a non-rotating Flettner rotor. When a superstructure is located behind the Flettner rotor it is beneficial to let the rotor rotate to control the direction and width of the wake and stabilize the higher levels of TKE over the height of the rotor.

When the cruise vessel is laying in a harbor the Flettner rotors are not rotating most of the time. Not considering induced passenger comfort by the Flettner rotor, like sound production and vibrations, it could be beneficial to let the rotor rotate. The excited loads could stabilize the vessel, when counteracted by ballast tanks, and the flow behind the rotor is more stable and controllable.

7.1.7. Spin ratio equal to 2

In this section the simulation of a Flettner rotor with a SR equal to 2 will be discussed.

Settling period

The asymmetry because of the rotational speed causes, for a rotor with a rotational speed of $SR \sim 2$, to initially shed a singular vortex. As can be seen in figure 7.109. After the initial vortex is shed a shear layer detaches around $t \sim 0.95s$, which is starting to develop around $t \sim 0.6s$, presented in figure 7.110.

Flow coefficients

The flow coefficients do no longer have a periodic behavior for the fully developed flow, as can be seen in figure 7.42. Vortex shedding is suppressed, this occurs when the unstable shear layer does not detach. The instability of the shear layer is what causes the shear layer to detach, instability increases according to the local Re of the flow. For higher SR the local velocity increases. This causes the transition point, where the shear layer becomes unstable, to move upstream on the rotor. A shear layer can reattach because the eddies in the shear layer cause the boundary layer and the external flow to mix.

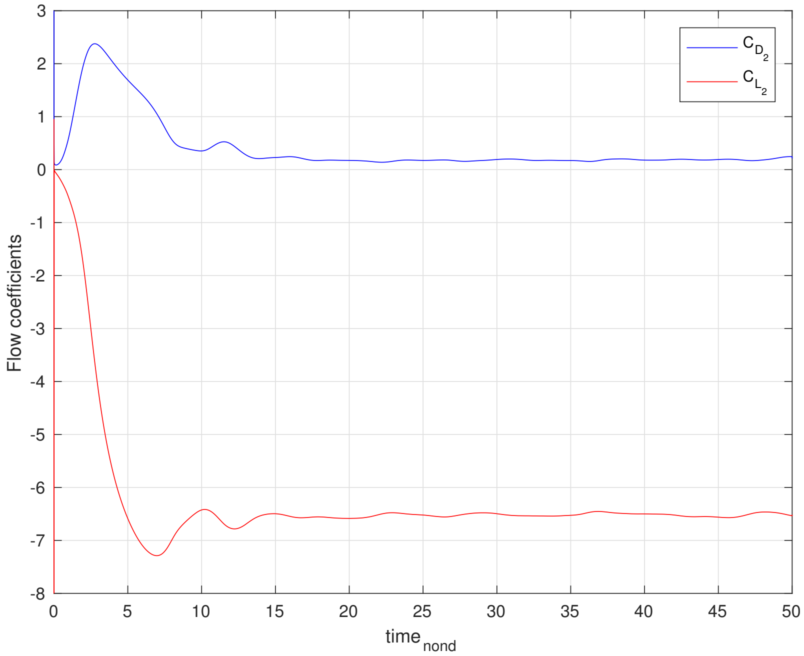

Figure 7.42: Flow coefficients of the rotor with a $SR \sim 2$ expressed in the non-dimensional time.

Fully developed flow

Figures 7.44 upto 7.52 show the development of the flow around the rotor upto $t = 4s$ shown in figure 7.43. A small instability in the flow is observed near the surface of the rotor in figure 7.43.

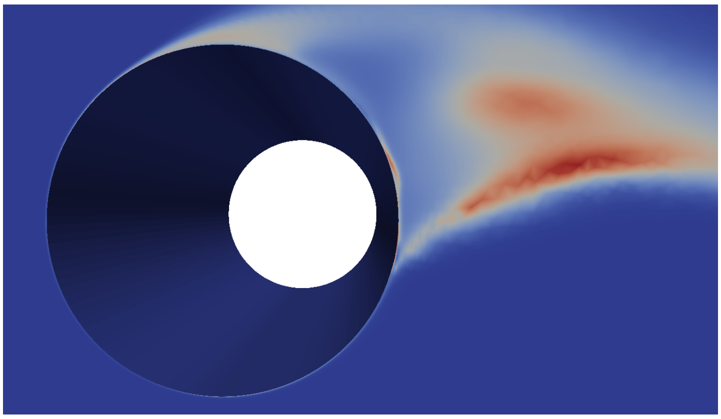

Figure 7.43: TKE $t = 4s$ $SR \sim 2$.

These instabilities do however not detach because of reattachment with the boundary layer. The shape of the wake, and the transition points, are stable for this SR. Local variation in the level of TKE are observed but they appear to come forth out of the change in TKE in vertical direction, rather than from changes in the horizontal plane. As can be seen in figure 7.42, the changes in the higher levels of TKE in the wake are not periodic in time and do not influence the behavior of the drag coefficient. Resulting in the smoother plot for the drag coefficient in figure 7.42. The higher levels of TKE are constant in direction over the height of the rotor but the lower levels of TKE are not. They fluctuate with periodic behavior over the rotor height, as is shown in figure 7.56.

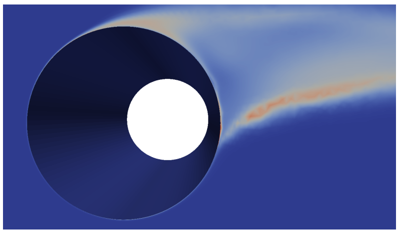

Figure 7.44: TKE $t = 3.55s$ $SR \sim 2$.

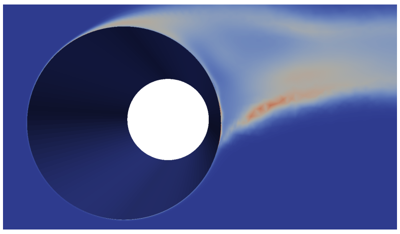

Figure 7.45: TKE $t = 3.60s$ $SR \sim 2$.

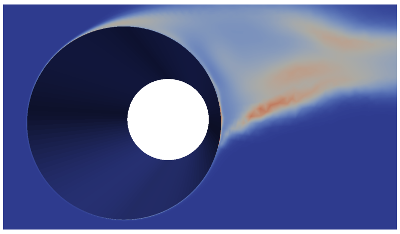

Figure 7.46: TKE $t = 3.65s$ $SR \sim 2$.

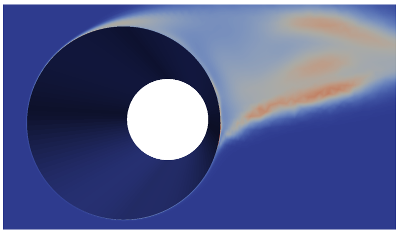

Figure 7.47: TKE $t = 3.70s$ $SR \sim 2$.

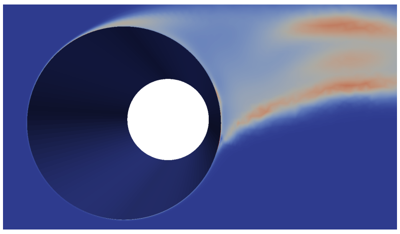

Figure 7.48: TKE $t = 3.75s$ $SR \sim 2$.

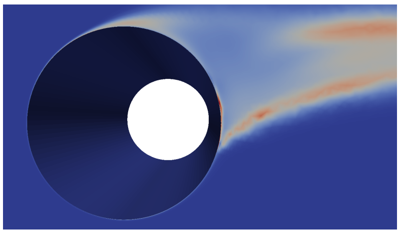

Figure 7.49: TKE $t = 3.80s$ $SR \sim 2$.

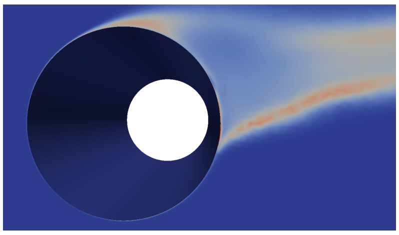

Figure 7.50: TKE $t = 3.85s$ $SR \sim 2$.

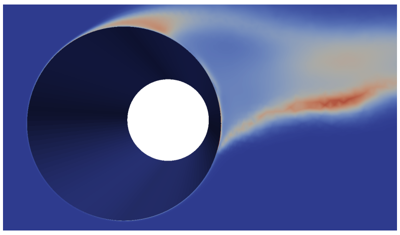

Figure 7.51: TKE $t = 3.90s$ $SR \sim 2$.

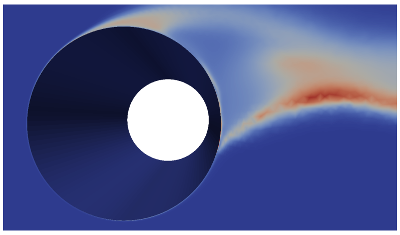

Figure 7.52: TKE $t = 3.95s$ $SR \sim 2$.

In figure 7.53 the three dimensional representation of the TKE is shown. A cross-section is made at $y = \frac{1}{2}D$, just above the rotor. The volume showing the TKE over the rotor height is clearly not evenly distributed. Equally is the intensity of the TKE not evenly distributed.

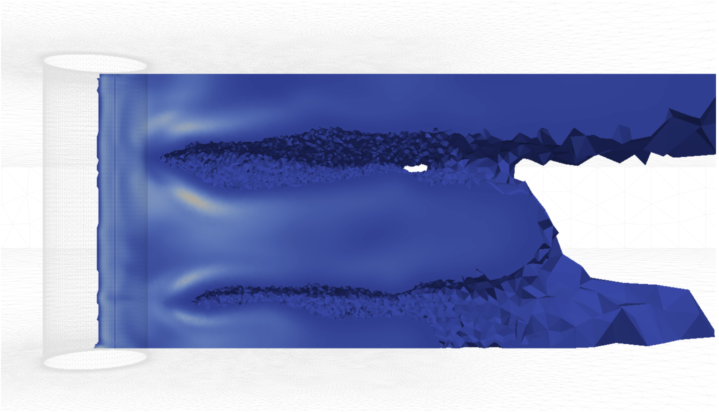

Figure 7.53: TKE $t = 4s$ $SR \sim 2$ $y = \frac{1}{2}D$.

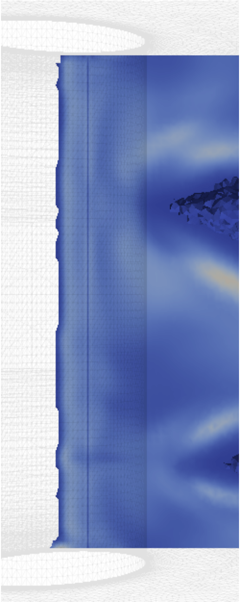

Figure 7.54: TKE $t = 4s$ $SR \sim 2$ $y = \frac{1}{2}D$.

From figure 7.44 to figure 7.52 it can be seen that the level of TKE near the surface is increasing. For $SR \sim 0$ & 1 the higher levels of TKE were located in the wake and was a laminar boundary layer observed. In figure 7.54 it can be seen that the levels of TKE are higher on the surface of the rotor; causing shear stresses.

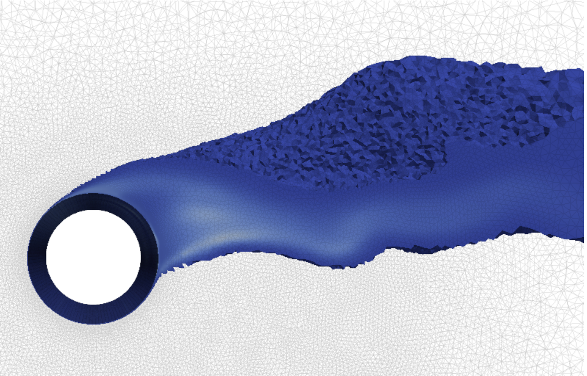

Figure 7.55: TKE $t = 4s$ $SR \sim 2$.

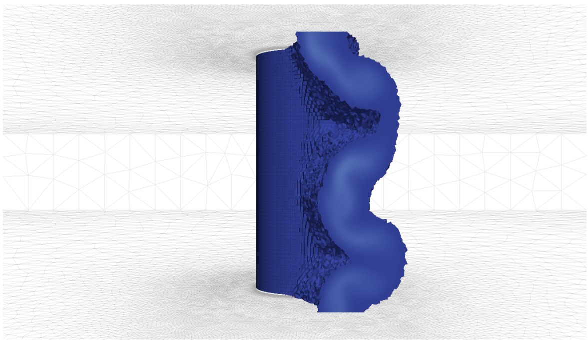

Figure 7.56: TKE $t = 4s$ $SR \sim 2$ $x = 1.5D$.

Concluding

A $SR \sim 2$ for a Flettner rotor results in suppressed vortex shedding and shear stress on the surface of the rotor. The intensity of the TKE in the wake is significantly reduced and the wake is slimmer, as are the transition points. The three dimensional effects of the TKE are large in vertical direction and a two dimensional simulation is not capable of determining a correct drag coefficient. The distribution of TKE along the rotor's height seem to show a whole period but this can not be concluded for sure without performing a CFD simulation for a higher rotor.

The rotating Flettner rotor shows a increasing unstable settling period w.r.t. increasing SR. For a SR equal to 2 the number of peaks, during the settling period, of the drag coefficient is reduced to one. The magnitude of the peak is however increased significantly. Confirming that for higher SR the apparent wind should deviate with a ramp to prevent a high impulse of the drag load on the rotor. The deviation of the apparent wind can only be controlled by slowly increasing or decreasing the sailing velocity. A sudden change in wind velocity can only be anticipated by reducing the rotational velocity of the rotor.

Because the higher levels of TKE are decreasing and moving more to the surface of the rotor, interaction with a superstructure becomes less significant. The superstructure will be located in a wake consisting mainly out of low levels of TKE that do fluctuate in direction over the height of the Flettner rotor. Their magnitude is however fairly constant and the wake is slimmer.

The suppressed vortex shedding reduces the vibrations on the Flettner rotor but increases the drag coefficient because of wall shear stresses. Those stresses are not captured in the laminar sublayers in the performed but the remaining boundary layer shows increasing levels of turbulence for increasing SR.

The magnitude of the load excited by the Flettner rotor is still dominated by the produced lift. The increasing lift indicates that the most optimal ratio between SR and excited load by the rotor is not reached for the SR equal to 2.

7.1.8. Spin ratio equal to 2.5

The SR equal to 2.5 is the highest SR simulated during this thesis.

Settling period

In figures 7.111, 7.112, 7.113 and 7.114 the settling period of the rotor with a $SR \sim 2.5$ is shown. The rotor with this SR only sheds one vortex around $t \sim 0.2s$. The separation point, where the flow separates from the boundary layer of the rotor, moves upstream on the rotor surface and the velocity differences are larger than for lower SR. The lower shear layer is not detaching in the same way as for $SR \sim 2$ around $t \sim 0.6s$. It immediately reattaches, the local velocities are high enough to increase the local turbulence to a level that it mixes the external flow and the boundary layer.

Flow coefficients

The flow coefficients for this rotational speed are very steady and show nearly no fluctuations, especially for the fully developed flow.

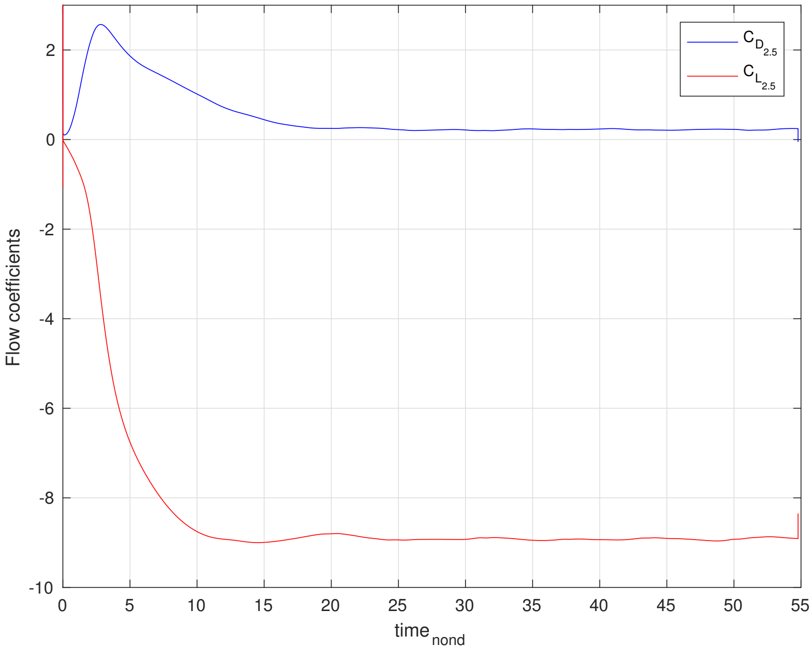

Figure 7.57: Flow coefficients of the rotor with a $SR \sim 2.5$ expressed in the non-dimensional time.

Fully developed flow

In figure 7.58 the TKE is shown of the flow around the rotor. The vectors show the direction of the change of TKE.

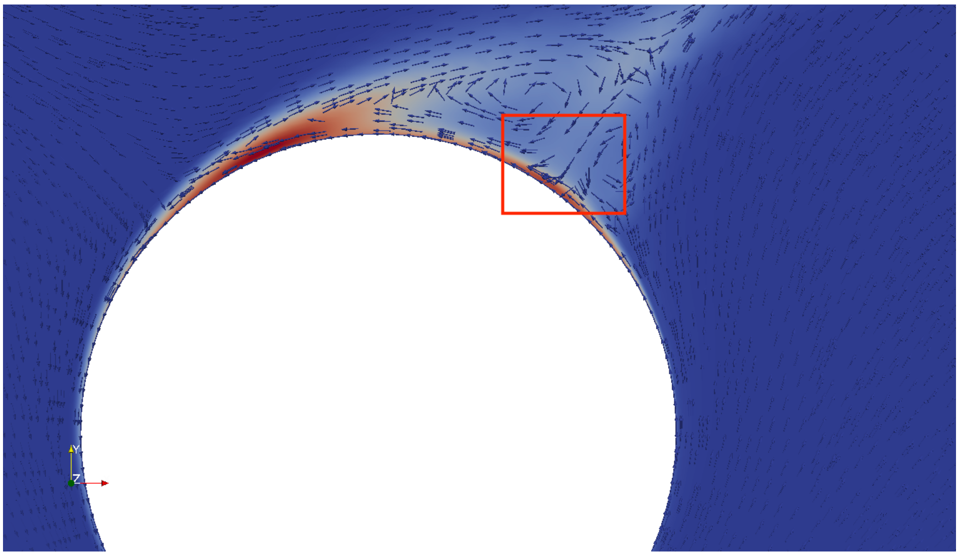

Figure 7.58: Cross-section of the flow around the rotor with the density of the TKE expressed in vector form (TKE $t = 3s$ $SR \sim 2.5$ $z = 2D$).

A clear stagnation point is shown where two shear layers are reattaching. Beside the stagnation point the high levels of TKE near the boundary of the rotor are shown, indicating a turbulent boundary layer at the top side of the rotor. The transition point where the boundary layer goes from laminar to turbulent has moved upstream from the separation point of the shear layer. This causes the reattachment of the shear layer and is the first stage of the drag crisis. A drag crisis is fully developed when the boundary layer around the rotor becomes fully turbulent.

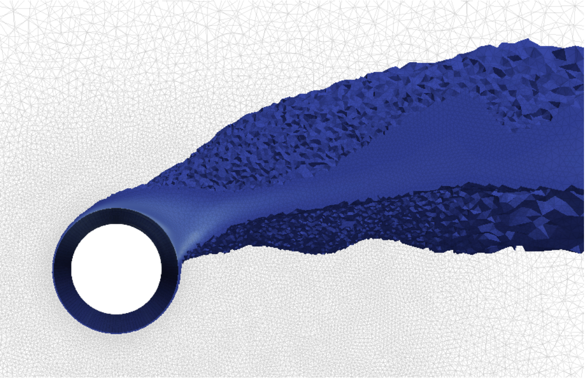

Figure 7.59: TKE $t = 4s$ $SR \sim 2.5$ $z = 3D$.

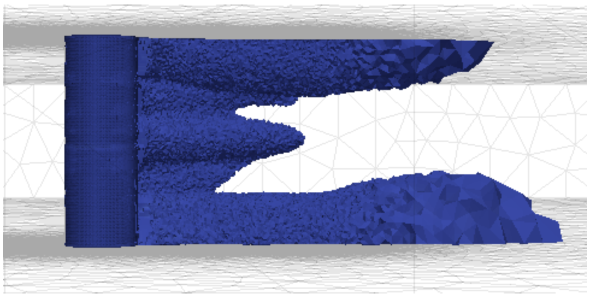

Figure 7.60: TKE $t = 4s$ $SR \sim 2.5$ $x = 3D$.

In figures 7.59 and 7.60 the turbulence around the rotor is shown to cover the whole surface of the rotor. Figure 7.59 shows a top-view of the whole rotor and the levels of TKE around it. Like with the lower SR the higher levels of TKE appear to be within in the wake and the wake is slimmer than for a $SR \sim 2$. In a similar way the upstream located separation point has moved further upstream.

The wake is varying in three dimensions and a periodic behavior is observed in the variation of TKE over the height of the rotor, shown in figure 7.60. The behavior of the TKE in figures 7.59 and 7.60 is represented by the lower values of TKE, represented by dark blue. The variation of the higher values of TKE can be seen in figure 7.61 showing a cross-section for $y = \frac{1}{2}D$ of figure 7.59.

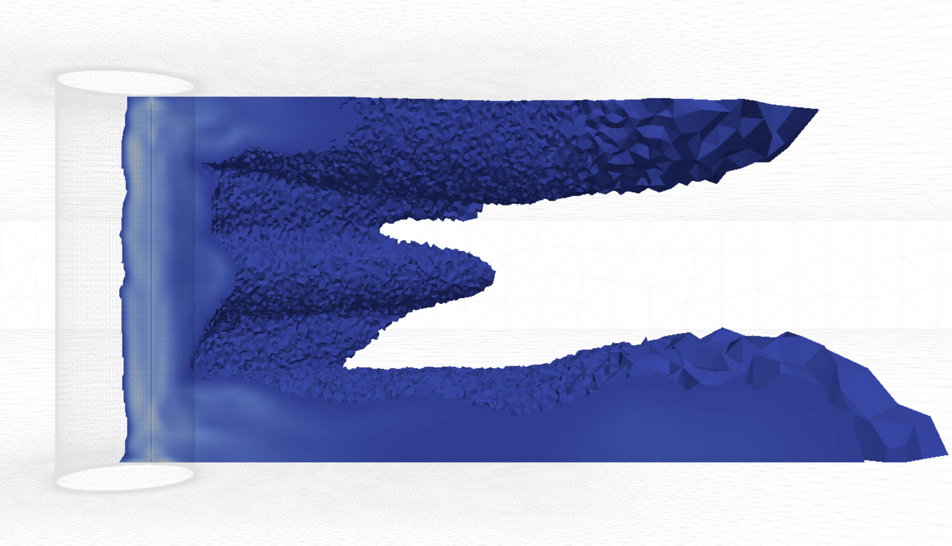

Figure 7.61: TKE $t = 4s$ $SR \sim 2.5$ $y = \frac{1}{2}D$.

The higher levels of TKE are clearly located near the rotor surface and do not show as much fluctuation over the rotor height as in figure 7.53, for a rotor with a $SR \sim 2$. The span of the whole wake is smaller than for lower SR.

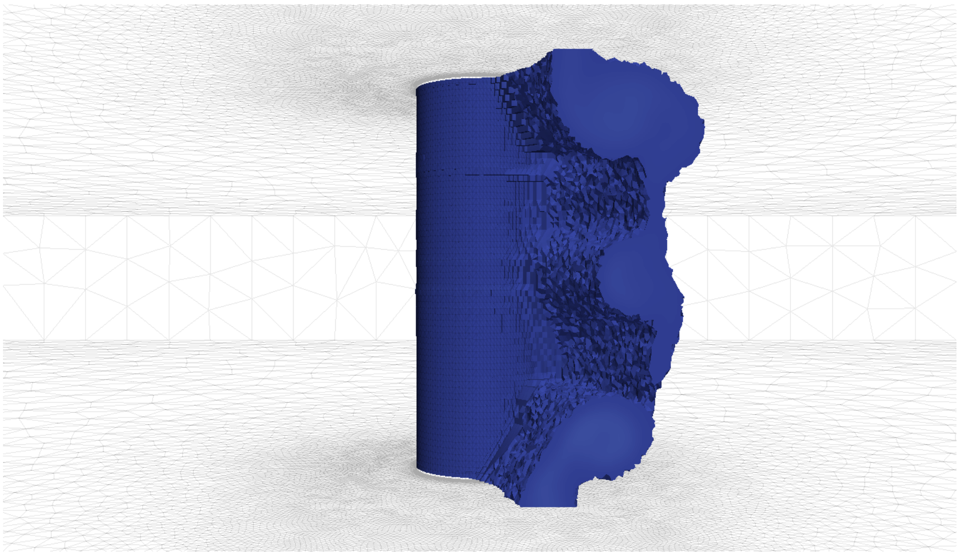

Figure 7.62: TKE $t = 4s$ $SR \sim 2.5$ $x = 1.5D$.

In figure 7.62 a cross-section of figure 7.59 is shown at $x = 1.5D$, showing the fluctuations of the TKE over the rotor height. The same fluctuations in TKE are observed as in figure 7.61, showing that only low values of TKE vary over the rotor height. The main angle of the wake with respect to the x-axis is larger than for a $SR \sim 2$.

Concluding

Only one vortex is shed during the settling period before the flow around the rotor becomes fully developed. The separation and transition point on the rotor surface move both upstream on the rotor surface, with the transition point located in front of the separation point. Indicating the drag crisis. The wake is slimmer and its contour constant in time. The higher levels of TKE concentrate closer to the rotor surface indicating, together with the reduction of the TKE in the wake, that the drag is dominated by shear stresses on the rotor surface. The three dimensional fluctuations of the TKE in the wake are pronounced even though the levels of intensity of the TKE are reduced.

A Flettner rotor experiencing this SR has a stable flow around it, meaning that the vortex shedding is completely suppressed and the wake consists only out lower levels of TKE. The drag coefficient increases slightly compared to the SR equal to 2 as a result of the drag crisis. The increase in drag for SR>2 is underestimated in the presented results because of the no-slip condition and the not included wall law. The drag coefficient will increase because of wall shear stresses and the levels of TKE in the wake are not expected to change. The direction and width of the wake can deviate when shear stresses and a wall law are included because the positions of the transition and stagnation points can differ. The change in the flow will not effect the rotor superstructure interaction because the interaction takes place far outside the boundary layer of the rotor.

The potential rotor-superstructure interaction appears to be decreasing for increasing SR because the wake increasingly consists out of lower levels of TKE. The lower levels of TKE vary over the height of the rotor (figure 7.62) but are constant in time. The levels of flow velocity and pressure around the rotor during the settling period are presented in figures 7.118, 7.122 and 7.126. Their maximum or minimum values are located near the boundary of the rotor and will not be present in the wake and thus influencing the rotor-superstructure interaction.

Even though the rotor-superstructure interaction decreases for increasing SR the simulation including the rotor and superstructure is simulated for a SR equal to 2.5. The contribution the Flettner rotor has as propulsion device is most optimal for this SR (out of the simulated SR). Therefore the rotor will experience this SR the most.

7.1.9. Comparison between the different spin ratio's

In this section the four rotors with different SR that are simulated will be compared and discussed.

Flow coefficients

Figure 7.63 shows the drag coefficients of the simulated rotors for increasing SR. The periodic vortex shedding behavior of the rotors with the two lowest SR can clearly be seen, together with the suppressed vortex shedding for the two highest SR. For increasing SR the stability of C_D increases as well.

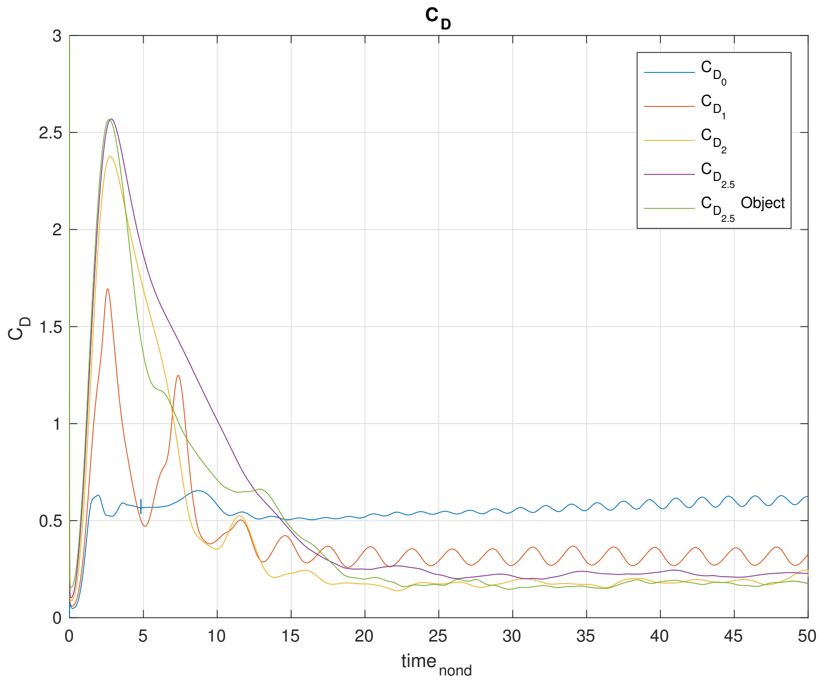

Figure 7.63: Drag coefficient for four SR's.

The converged values for the drag coefficients are presented in table 7.4.

C_{D_0}	0.6
C_{D_1}	0.31
C_{D_2}	0.18
$C_{D_{2.5}}$	0.22

Table 7.4: Drag coefficients for four spin ratios.

As discussed in the previous sections the drag coefficient is dictated by the levels of turbulence in the wake or the boundary layer. The shear stresses acting on the surface of the rotor are not captured in the flow coefficients because of the no-slip condition on the surface. The drag coefficient is therefore underestimated for SR equal to 2 and 2.5. In figures 7.71, 7.65, 7.66 and 7.67 the wake is shown in the xz-plane with for all figures the same legend for the TKE levels and the same scale.

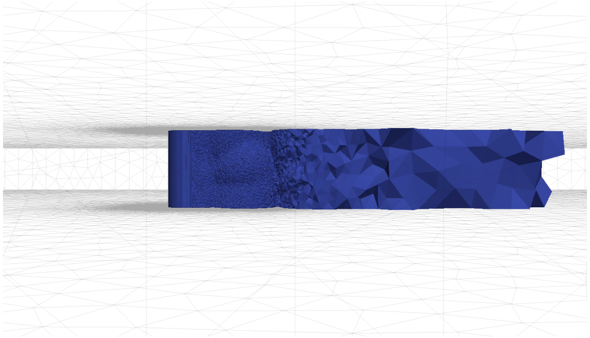

Figure 7.64: TKE $t = 4s$ $SR \sim 0$.

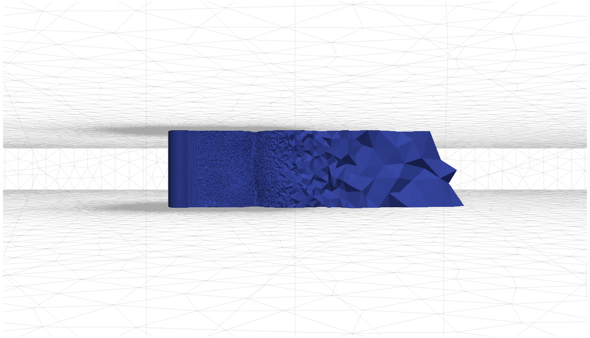

Figure 7.65: TKE $t = 4s$ $SR \sim 1$.

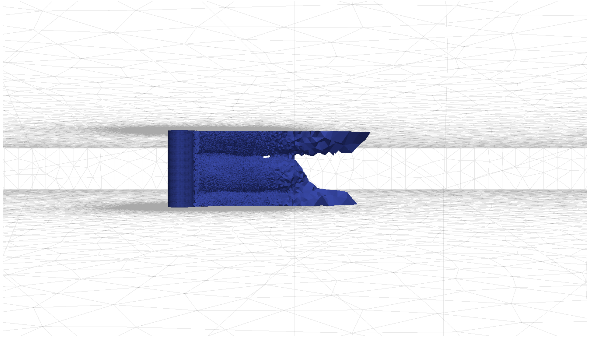

Figure 7.66: TKE $t = 4s$ $SR \sim 2$.

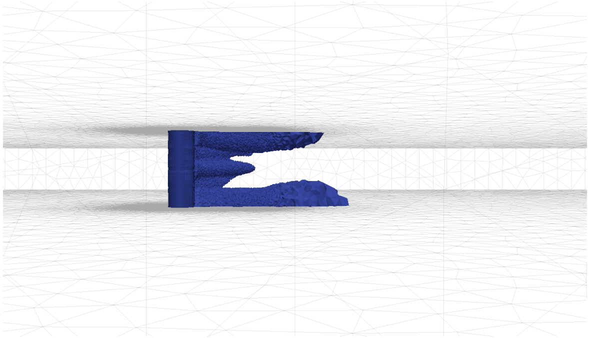

Figure 7.67: TKE $t = 4s$ $SR \sim 2.5$.

The span of the wake decreases for an increase in SR. The wake is larger for $SR \sim 0$ & 1 than it would have been for grids with a larger refinement zone. As can be seen by the coarse distribution of TKE, interpolated over the surfaces in between vertices, located upstream from the rotor.

A top-view of the TKE in the wake is shown in figures 7.68, 7.69, 7.70 and 7.71 showing a decrease of high TKE levels in the wake for increasing SR. For increasing SR's the C_D increases because the boundary layer becomes more turbulent; the transition point between a laminar and turbulent boundary layer moves upstream. The ratio between the rise in SR and the corresponding C_D reduces because of the suppressed vortex shedding; the drag crisis has occurred. The level of turbulence in the boundary layer starts to increase significantly for $SR \sim 2$ & 2.5, the separating shear layers stay close to the rotor together with an decreasing span width of the wake, indicating that the drag coefficient will start increasing again for higher SR because of wall shear stresses.

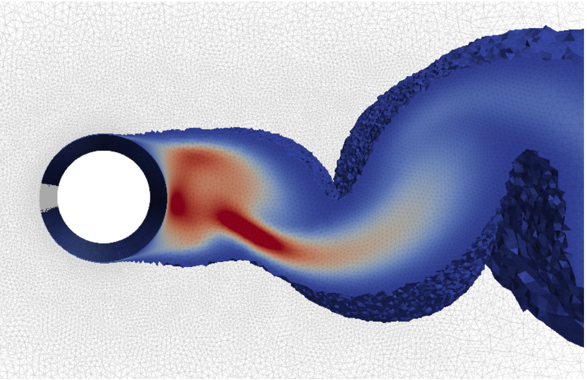

Figure 7.68: TKE $t = 4s$ $SR \sim 0$ $z = 3D$.

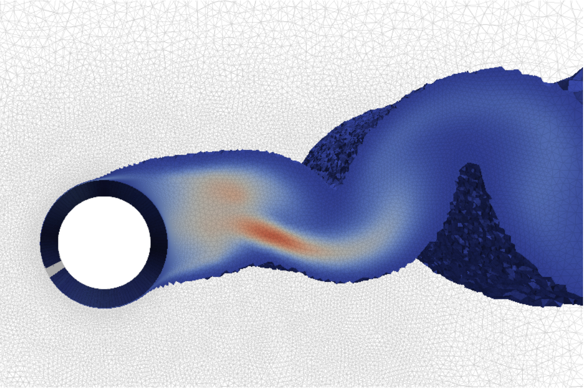

Figure 7.69: TKE $t = 4s$ $SR \sim 1$ $z = 3D$.

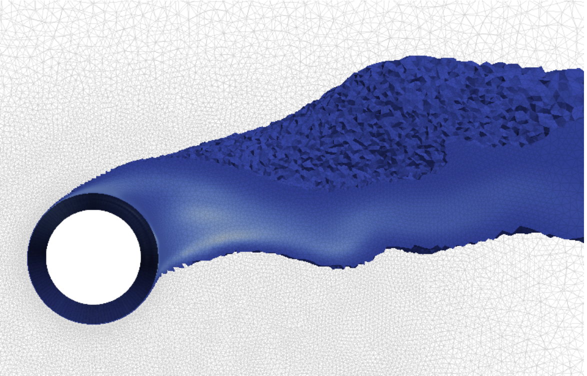

Figure 7.70: TKE $t = 4s$ $SR \sim 2$ $z = 3D$.

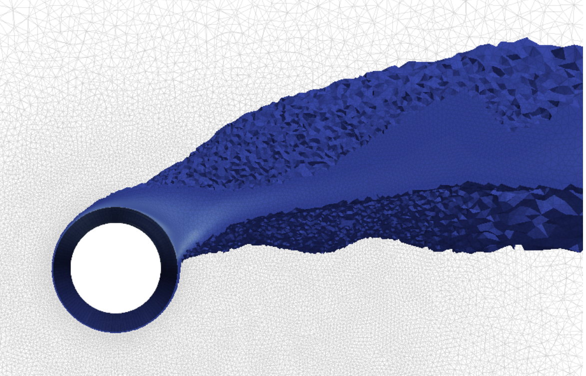

Figure 7.71: TKE $t = 4s$ $SR \sim 2.5$ $z = 3D$.

That the higher levels of TKE concentrate close to the surface of the rotor is also shown in the cross-sections in the yx-plane shown in figures 7.72, 7.73, 7.74 and 7.75

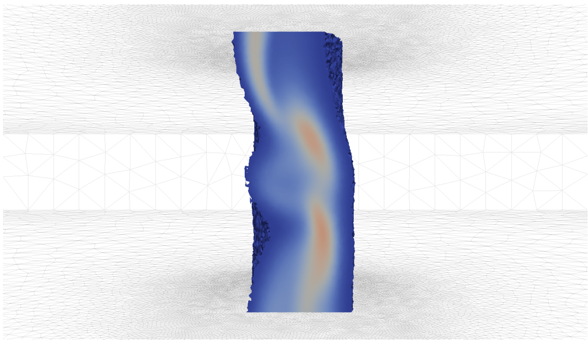

Figure 7.72: TKE $t = 10s$ $SR \sim 0$ $x = 1.5D$.

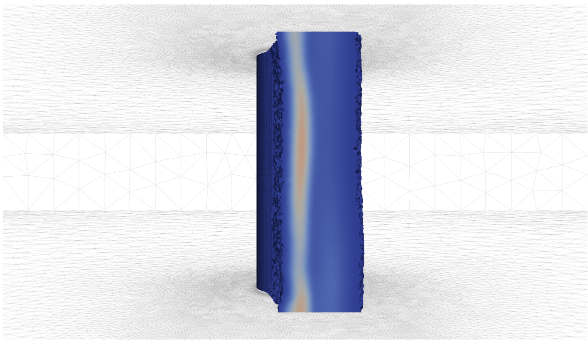

Figure 7.73: TKE $t = 4s$ $SR \sim 1$ $x = 1.5D$.

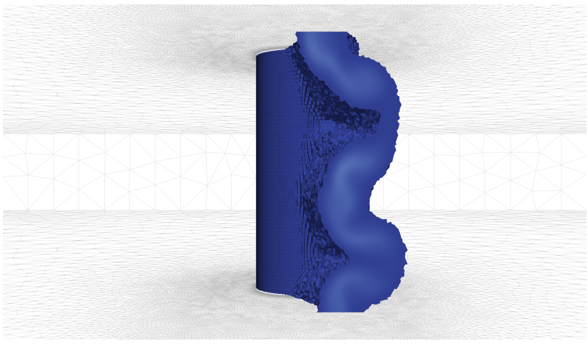

Figure 7.74: TKE $t = 4s$ $SR \sim 2$ $x = 1.5D$.

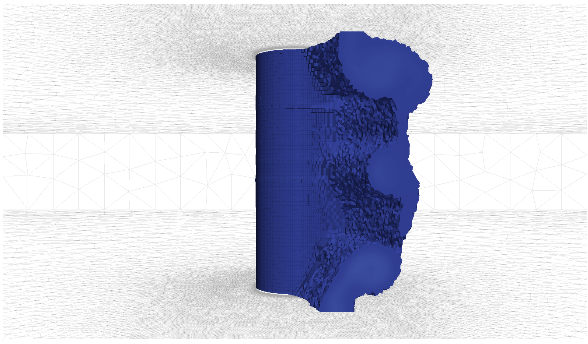

Figure 7.75: TKE $t = 4s$ $SR \sim 2.5$ $x = 1.5D$.

The increasing angle between the wake and the x-axis can be seen for increasing SR together with an decrease of high levels of TKE in the wake. The fluctuations of the magnitude of the TKE over the rotor height causes for each SR that it cannot be simulated using two dimensional CFD simulations. For the $SR \sim 0$ the higher levels of TKE differ in the wake in magnitude and direction over the height of the rotor. The SR showing the most two dimensional behavior is for a $SR \sim 1$, however the intensity of the TKE still differs over the rotor height. For $SR \sim 2$ & 2.5 the three dimensional effects are clear in vertical direction even though the magnitude of the TKE decreases in the wake.

The height of $3D\ m$ seems to capture the whole correlation length for all SR. To validate this statement a simulation should be performed with exact the same grid and solver settings but for a larger rotor height.

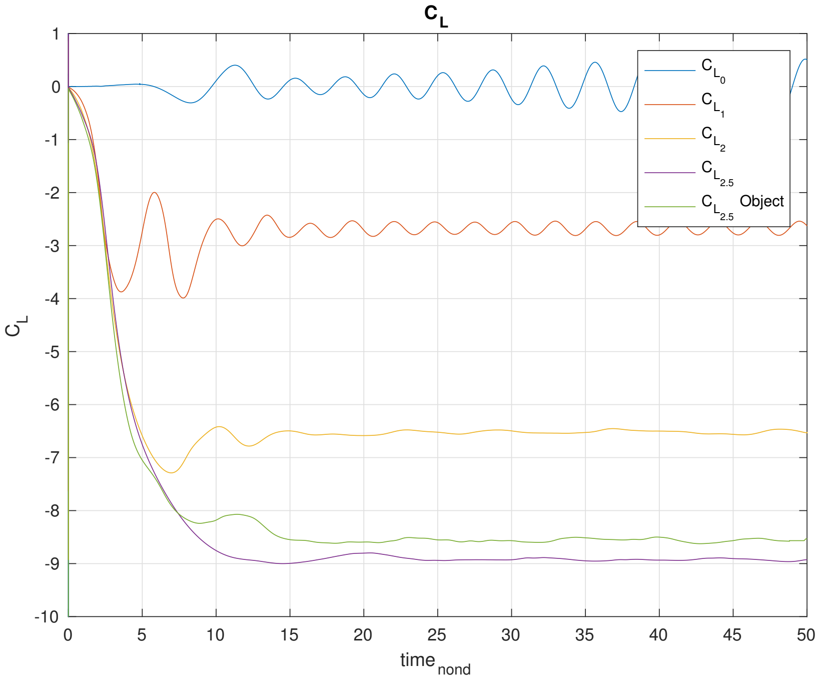

Figure 7.76: Lift coefficient for four SR's.

The lift coefficients for the four spin ratios are plotted in figure 7.76. The pressure fluctuations over the rotor height because of the vortex shedding and or detaching shear layers can be seen in the periodic behavior for $SR \sim 0$ & 1. The pressure distribution is uniform over the rotor height for $SR \sim 1$ & 2 & 2.5 as can be seen in figures 7.120, 7.124, 7.121, 7.125, 7.122 and 7.126. For the $SR \sim 0$ there are slight fluctuations in the pressure distribution over the height of the rotor as can be seen in figure 7.119 and 7.123.

The converged values for the lift coefficients are presented in table 7.5.

C_{L0}	0
C_{L1}	-2.68
C_{L2}	-6.52
$C_{L2.5}$	-8.92

Table 7.5: Lift coefficients for four spin ratios.

The ratios between the drag and lift coefficients are determined to evaluate the influence of the rotational speeds on the direction of the load excited by the Flettner rotor. The angles a, as shown in figure 7.77, are shown in table 7.6

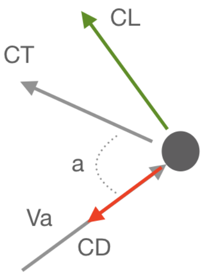

Figure 7.77: Direction of the coefficients for different SR.

Different SR's do not change the angle in which the load on the Flettner rotor acts. The influence the drag crisis has on the change of the load cannot be concluded because the change of the angle is not known without the drag crisis.

	a
C_{T_0}	0°
C_{T_0}	83.4°
C_{T_0}	88.42°
$C_{T_{2.5}}$	88.59°

Table 7.6: Lift coefficients for four spin ratios.

Concluding

For increasing SR the lift production by the Flettner rotor increases without signs of a saturation point, indicating that the most optimal SR, to use the Flettner rotor for propulsion purposes, is not reached. The drag production will increase for increasing SR after a SR equal to 2, the drag will increase more than displayed in figure 7.63 because of the laminar sublayer and the neglected wall roughness.

The interaction between the rotor and superstructure will decrease for increasing SR because of a reduction in TKE in the wake and its increasing independence of time.

7.1.10. Spin ratio equal to 2.5 including superstructure

The positioning of the cylinder in the wake of the rotor is determined considering the direction of the apparent wind w.r.t. the x-axis of the vessel. The rotor rotates in clockwise direction. When comparing the flow around the rotor with a $SR \sim 2.5$ the differences in rotational direction should be taken into account.

Settling period

The settling period does not change when a superstructure is placed in the wake of the rotor, it remains $t_{nond} = 20 \sim 1.6s$. The moments in time that were evaluated for the different rotational speeds ($t \sim 0.05s$, $0.2s$, $0.4s$) will also be discussed for the rotor with the superstructure in the wake. Images of the flow velocity around rotor and superstructure are presented in figure 7.79 upto figure 7.82.

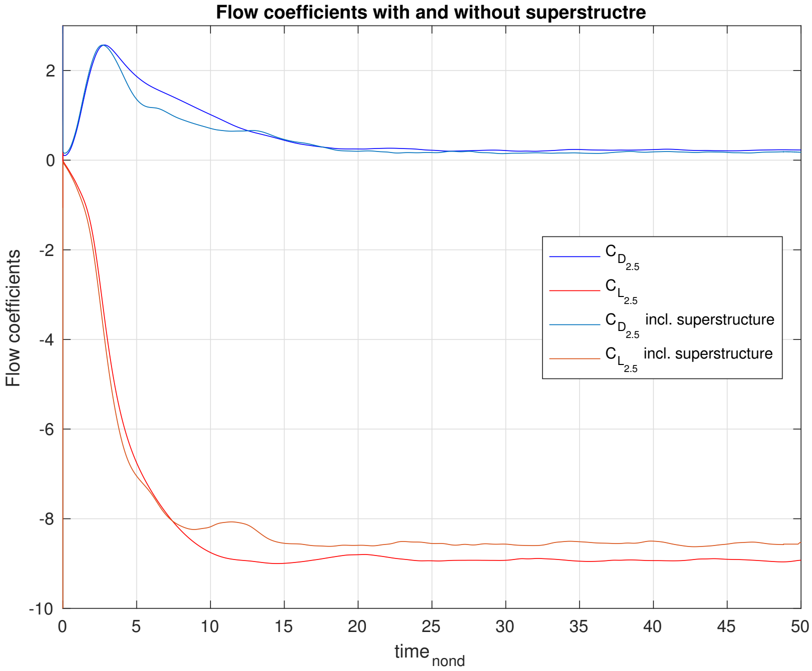

Figure 7.78: Lift and drag coefficient for a rotor with and without an object in the wake ($SR \sim 2.5$).

The superstructure in the wake has the same dimensions as the rotor and can therefore be compared to the rotor with a $SR \sim 0$. Until $t = 0.2s$ both the rotor and the superstructure do not seem to be effected by interaction between both. At $t = 0.4s$ the pressure corresponding to the shown velocities do influence the shedded vortex, by the rotor, and the separating shear layers of the superstructure. The rotor has an extra separating shear layer similar to a rotor with a $SR \sim 2$ around $t = 0.6s$, shown in figure 7.110 and figure 7.81. The detachment of the second shear layer occurs differently for a rotor with or without a superstructure in its wake as is seen in the drag coefficient in figure 7.78.

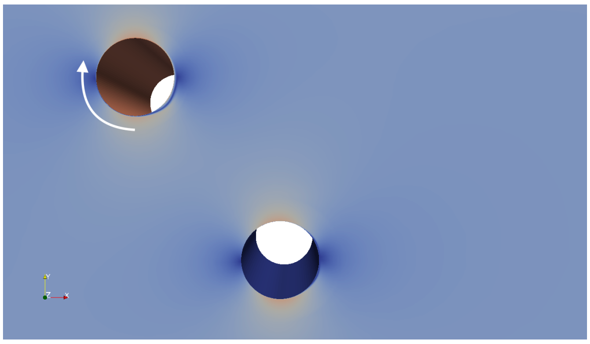

Figure 7.79: Velocity of the flow around rotor with superstructure in the wake $t = 0.05s$ $SR \sim 2.5$.

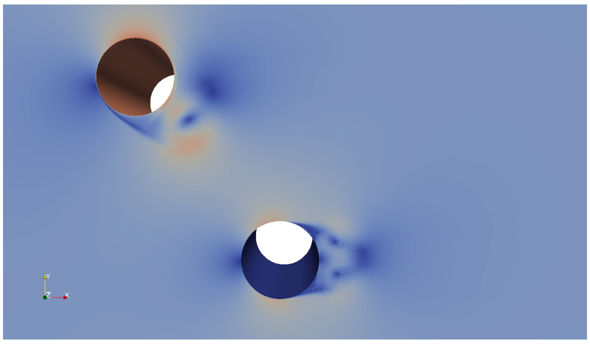

Figure 7.80: Velocity of the flow around rotor with superstructure in the wake $t = 0.2s$ $SR \sim 2.5$.

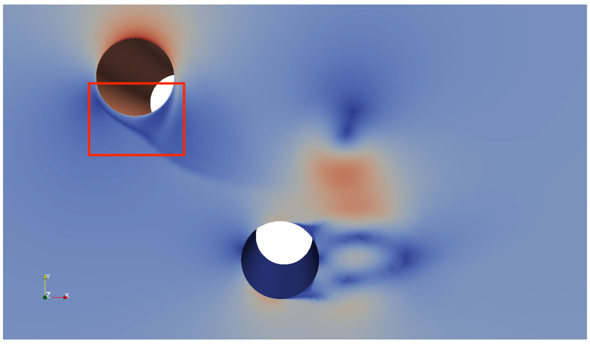

Figure 7.81: Velocity of the flow around rotor with superstructure in the wake $t = 0.4s$ $SR \sim 2.5$.

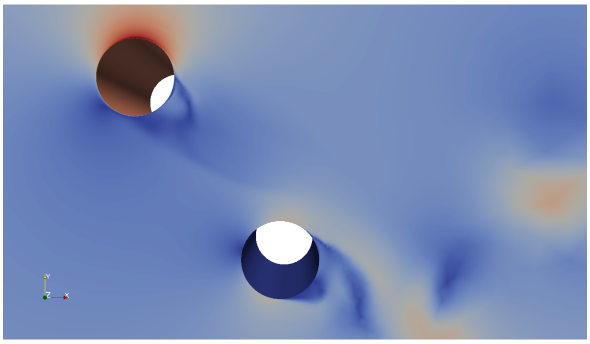

Figure 7.82: Velocity of the flow around rotor with superstructure in the wake $t = 0.6s$ $SR \sim 2.5$.

In figure 7.83 upto figure 7.86 the flow around a rotor with a $SR \sim$ with and without a superstructure in the wake are shown. These images serve to explain the slight increase in the drag coefficient and decrease in the absolute lift coefficient in figure 7.78 around $t = 1s$ or $t_{nond} = 12.4$.

The pressure distribution on the rotor with the superstructure in the wake, because of the superstructure, causes instabilities in the wake. Resulting in high levels of TKE near the rotor surface and an unevenly distributed flow velocity in the wake. That the pressure is influenced by the presence of the superstructure can be concluded out of the presence of the same irregularities in the wake in figure 7.84.

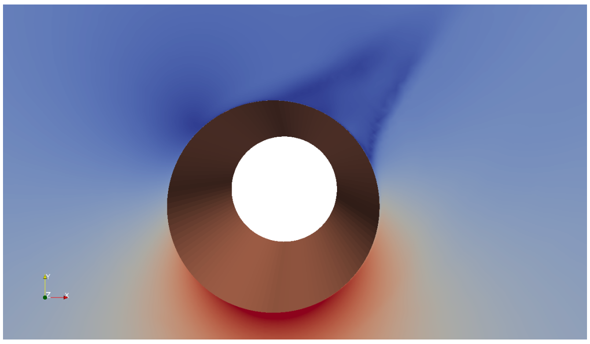

Figure 7.83: Velocity of the flow around rotor $t = 1s$ $SR \sim 2.5$.

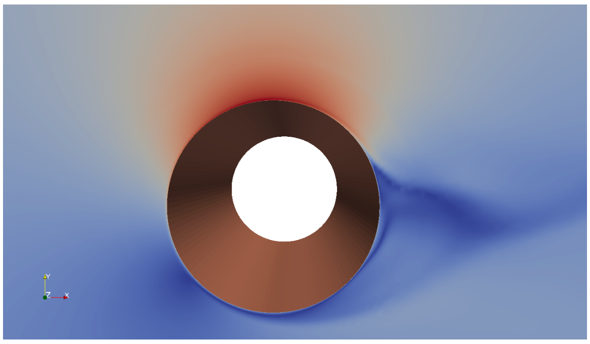

Figure 7.84: Velocity of the flow around rotor with superstructure in the wake $t = 1s$ $SR \sim 2.5$.

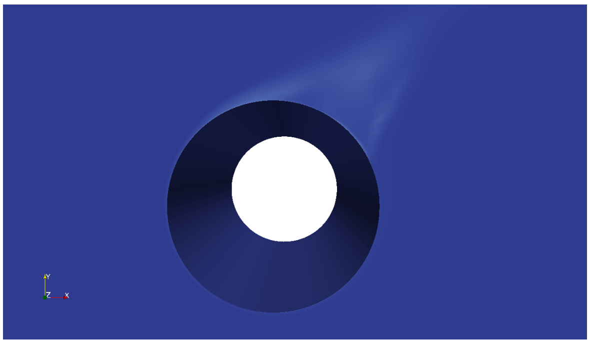

Figure 7.85: TKE of the flow around rotor $t = 1s$ $SR \sim 2.5$.

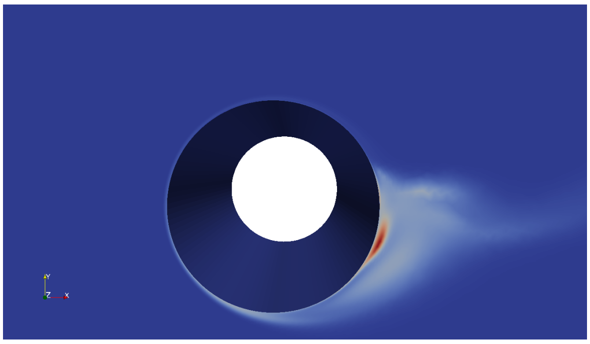

Figure 7.86: TKE of the flow around rotor with superstructure in the wake $t = 1s$ $SR \sim 2.5$.

The velocity and thus pressure are constant over the height of the rotor as can be seen in figure 7.87. In figure 7.88 the superstructure and the fluctuations in the flow velocity over its height are shown, similar to the fluctuations shown in figure 7.115.

Figure 7.87: Velocity over the rotor height with superstructure in the wake ($t = 0.6s$ $SR \sim 2.5$).

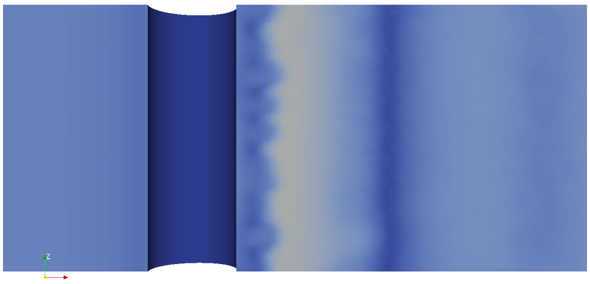

Figure 7.88: Velocity over the height of the superstructure in the wake of the rotor($t = 0.6s$ $SR \sim 2.5$).

Fully developed flow

To evaluate the turbulent behavior of the flow around the rotor and the superstructure, the TKE in the flow around both is displayed in the next figures.

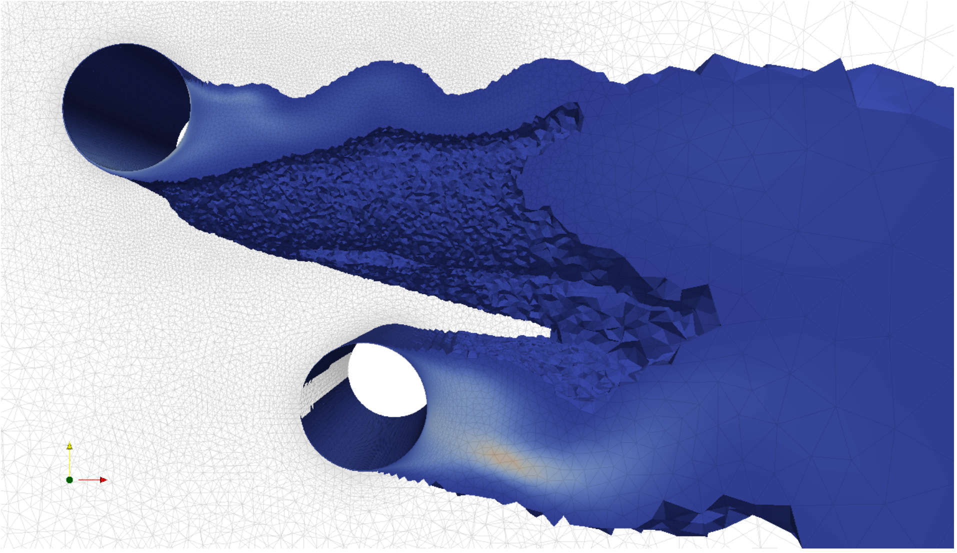

Figure 7.89: TKE of the flow around the rotor with a superstructure in the wake ($t = 4s$ $SR \sim 2.5$).

The differences in the distribution of the TKE is observed in the wake of the rotor and the superstructure. The shape of the wake behind the superstructure is still stable over the rotor height. The wake of the superstructure has rotated with respect to its x-axis. The direction of the wake of the rotor is located in its x-direction, influenced by the high pressure located above the superstructure.

The distribution of the TKE has not changed on the surface of the superstructure because of the presence of the rotor, except from the rotation of the wake influencing the position where no TKE is observed (figure 7.89). The turbulent properties of the boundary layer of the rotor are similar to the rotor without the superstructure in its wake.

In the next figures three cross sections are presented in the xz-plane, two in the xy-plane and one in the yz-plane, presenting the turbulent behavior of the flow in three dimensions around the rotor and superstructure. In figure 7.90 the location of the cross section presented in figure 7.91 is shown. The distribution of the higher and lower levels of TKE in the wake of the superstructure do not differ from the rotor with a $SR \sim 0$.

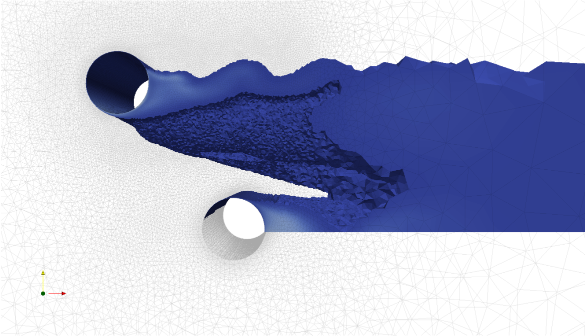

Figure 7.90: TKE of the flow around rotor with superstructure in the wake $t = 4s$ $SR \sim 2.5$.

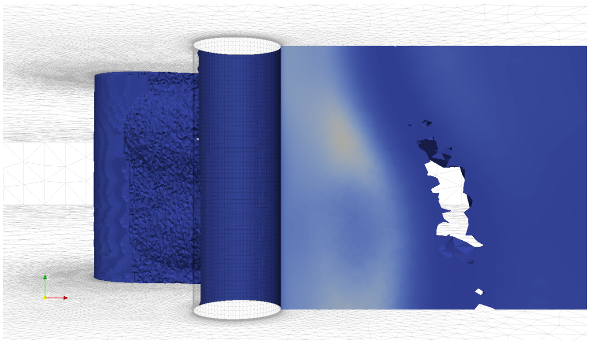

Figure 7.91: TKE of the flow around rotor with superstructure in the wake $t = 4s$ $SR \sim 2.5$ $y_{superstructure} = 0D$.

Figure 7.93 shows a similar distribution of the TKE in the wake and on the surface of the rotor as for a rotor without superstructure in its wake. The higher levels of TKE are located on the surface of the rotor or near the rotor in the wake. The wake displays large fluctuations along the height of the rotor.

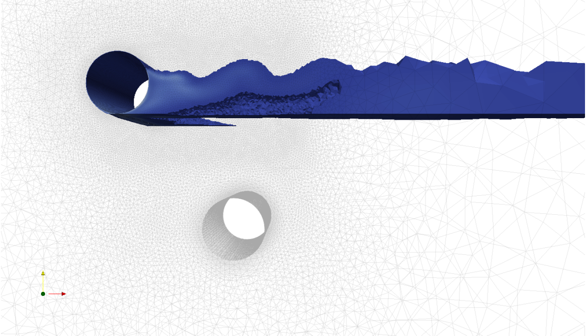

Figure 7.92: TKE of the flow around rotor with superstructure in the wake $t = 4s$ $SR \sim 2.5$.

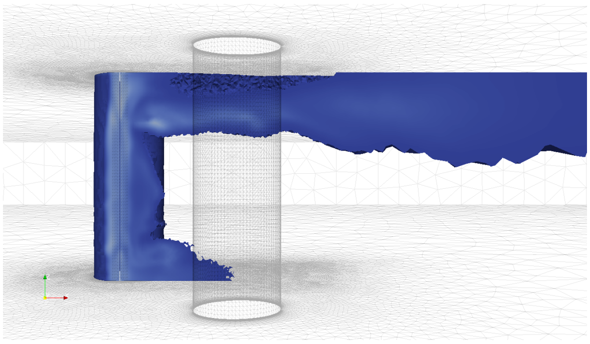

Figure 7.93: TKE of the flow around rotor with superstructure in the wake $t = 4s$ $SR \sim 2.5$ $y = -\frac{1}{2}D$.

Figure 7.95 shows that the wake by the rotor changes in direction in the xy-plane in the z-direction. Causing that only a fraction of the wake is captured in figure 7.95.

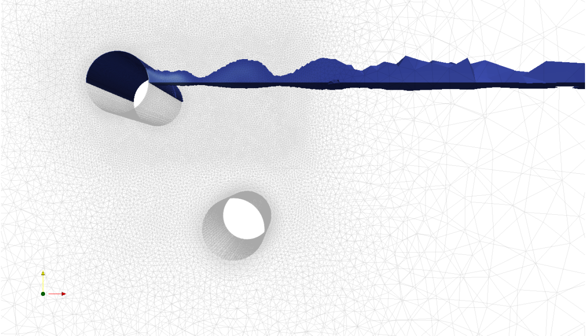

Figure 7.94: TKE of the flow around rotor with superstructure in the wake $t = 4s$ $SR \sim 2.5$.

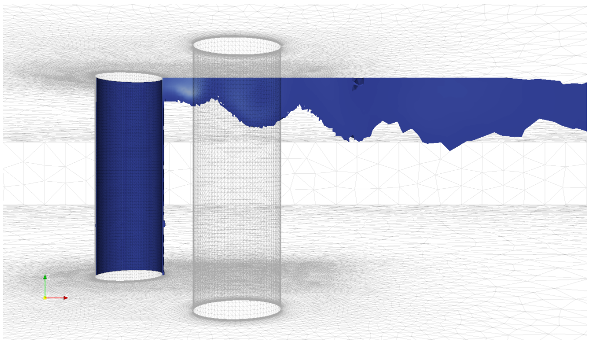

Figure 7.95: TKE of the flow around rotor with superstructure in the wake $t = 4s$ $SR \sim 2.5$ $y = 0D$.

The variation of the TKE observed in figure 7.95 can also be observed in figure 7.96. The wake of the rotor is influences in its direction by the pressure of the wake of the superstructure. The intensity levels of the TKE in the wake of the superstructure vary in the same way as in the wake of a rotor with a $SR \sim 0$.

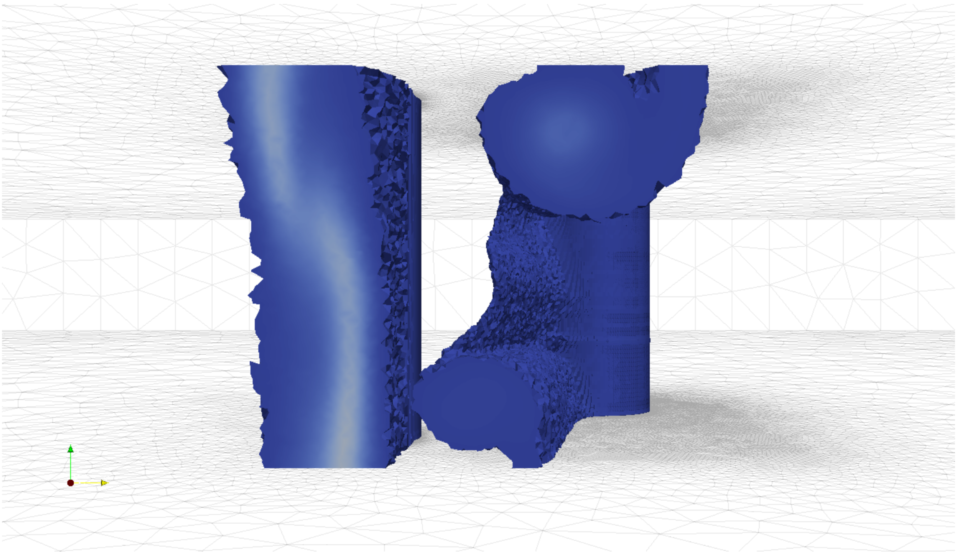

Figure 7.96: TKE of the flow around rotor with superstructure in the wake $t = 4s$ $SR \sim 2.5$ $x = 1\frac{1}{2}D$.

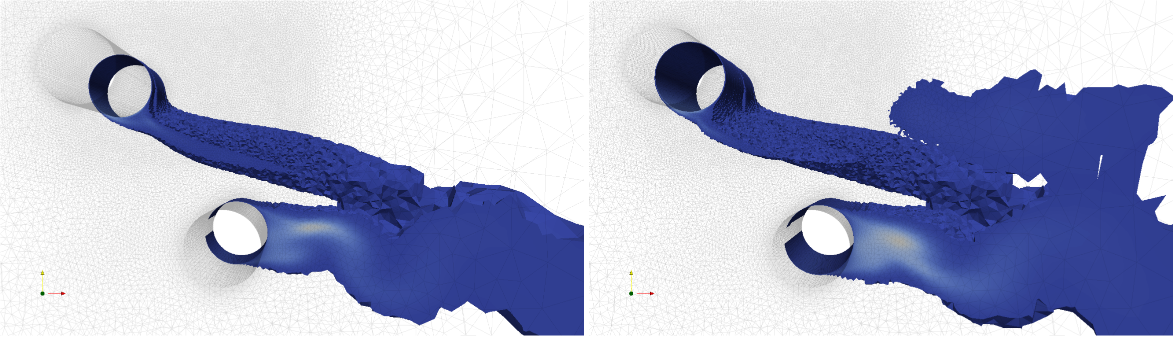

Figure 7.97: TKE of the flow around rotor with superstructure in the wake $t = 4s$ $SR \sim 2.5$ $z = D$.

Figure 7.98: TKE of the flow around rotor with superstructure in the wake $t = 4s$ $SR \sim 2.5$ $z = 2D$.

The interaction between the two wakes and their pressure differences seem to influence the direction of the wake but not the orientation of the higher intensity levels of TKE in them.

Concluding

The rotor with the superstructure in its wake has a settling period very similar to a rotor without a superstructure in its wake. There are however more instabilities in terms of pressure and TKE variations in the wake. Resulting from the interaction between the separating shear layers, of the superstructure, with the wake of the rotor.

The direction of the wake and its distribution over the height of the rotor are different from a rotor with a $SR \sim 2.5$. As displayed in figure 7.93 do only the lower values of TKE change because of the interaction with the superstructure. The higher levels of TKE are, like for a rotor with a $SR \sim 2.5$, still located on the surface of the rotor. In combination with the turbulent boundary layer has this as an result that the drag coefficient does not change significantly because of the rotor superstructure interaction. The suppressed vortex shedding remains after the superstructure is located in the wake of the rotor because of the turbulent boundary layer.

The pressure interaction between the superstructure and the wake occurs further away from the surface of the rotor; in the wake. The large pressure differences between the two objects in the flow causes the lift coefficient to decrease.

When a Flettner rotor is implemented on a cruise vessel close to a superstructure the influence of their interaction will only consist out of a lift reduction of the rotor. This is only valid for Flettner rotors with a SR larger than two; for SR where vortex shedding is suppressed. The vortex shedding is suppressed because the higher levels of TKE are located in the boundary layer of the rotor and no longer in the wake. That the higher levels of TKE are no longer present in the wake is also the reason that the drag produced by the Flettner rotor does not change when a superstructure is placed in its wake.

For SR lower than two the superstructure should not be placed closer than three times the diameter, of the rotor, close to the rotor. When the superstructure is located closer to the rotor than that the higher levels of TKE will interact with the superstructure and the flow coefficient will change.

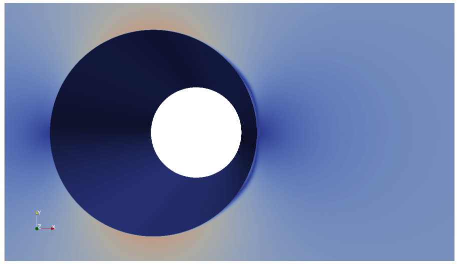

Figure 7.99: Velocity $SR \sim 0$ $t = 0.05s$.

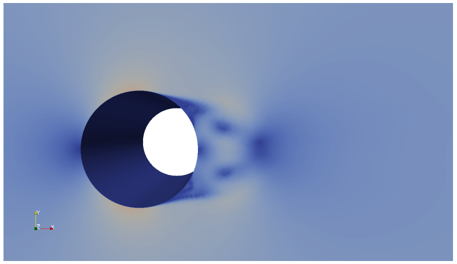

Figure 7.100: Velocity $SR \sim 0$ $t = 0.2s$.

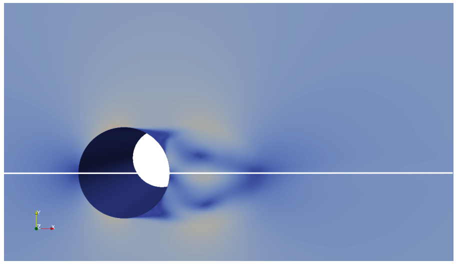

Figure 7.101: Velocity $SR \sim 0$ $t = 0.4s$.

Figure 7.102: Velocity $SR \sim 0$ $t = 0.6s$.

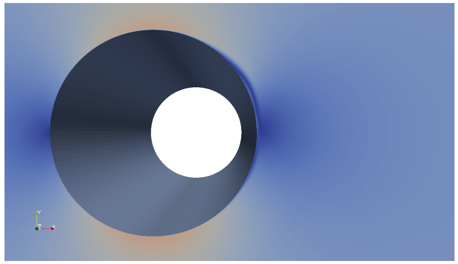

Figure 7.103: Velocity $SR \sim 1$ $t = 0.05s$.

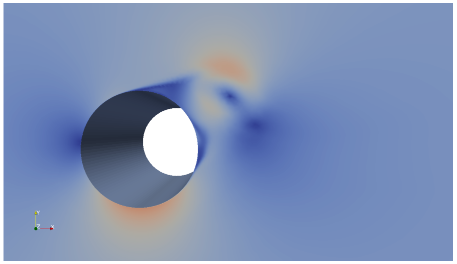

Figure 7.104: Velocity $SR \sim 1$ $t = 0.2s$.

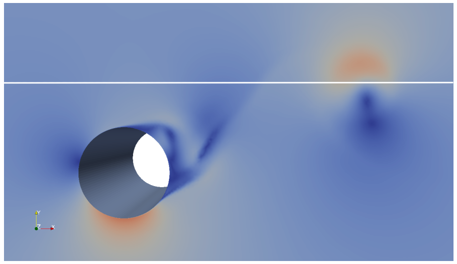

Figure 7.105: Velocity $SR \sim 1$ $t = 0.4s$.

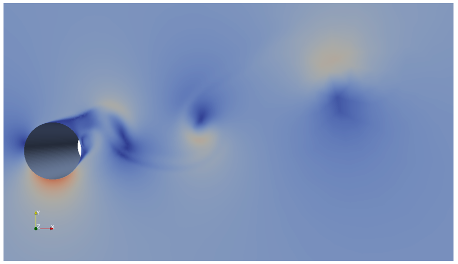

Figure 7.106: Velocity $SR \sim 1$ $t = 0.6s$.

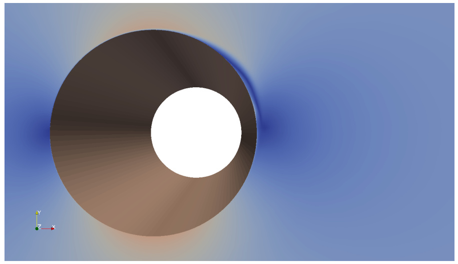

Figure 7.107: Velocity $SR \sim 2$ $t = 0.05s$.

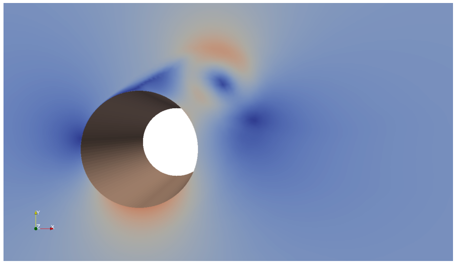

Figure 7.108: Velocity $SR \sim 2$ $t = 0.2s$.

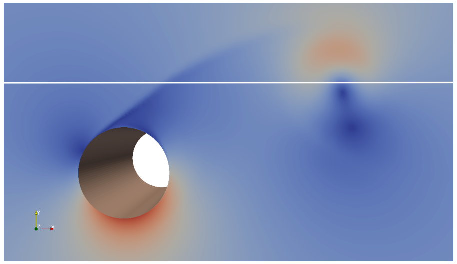

Figure 7.109: Velocity $SR \sim 2$ $t = 0.4s$.

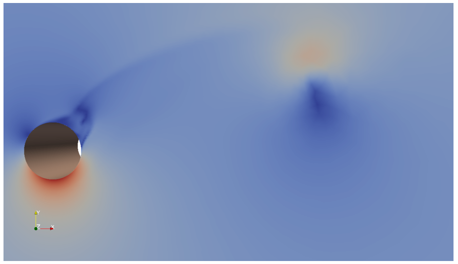

Figure 7.110: Velocity $SR \sim 2$ $t = 0.6s$.

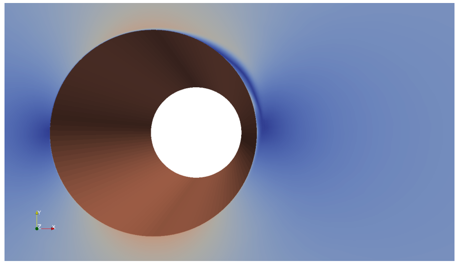

Figure 7.111: Velocity $SR \sim 2.5$ $t = 0.05s$.

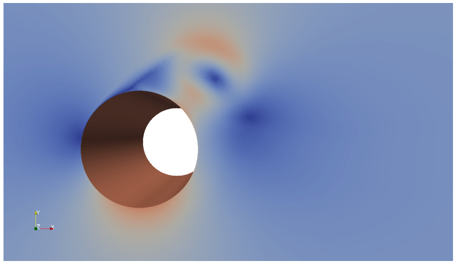

Figure 7.112: Velocity $SR \sim 2.5$ $t = 0.2s$.

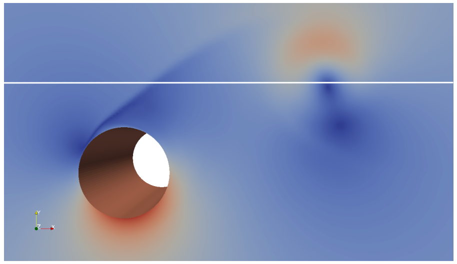

Figure 7.113: Velocity $SR \sim 2.5$ $t = 0.4s$.

Figure 7.114: Velocity $SR \sim 2.5$ $t = 0.6s$.

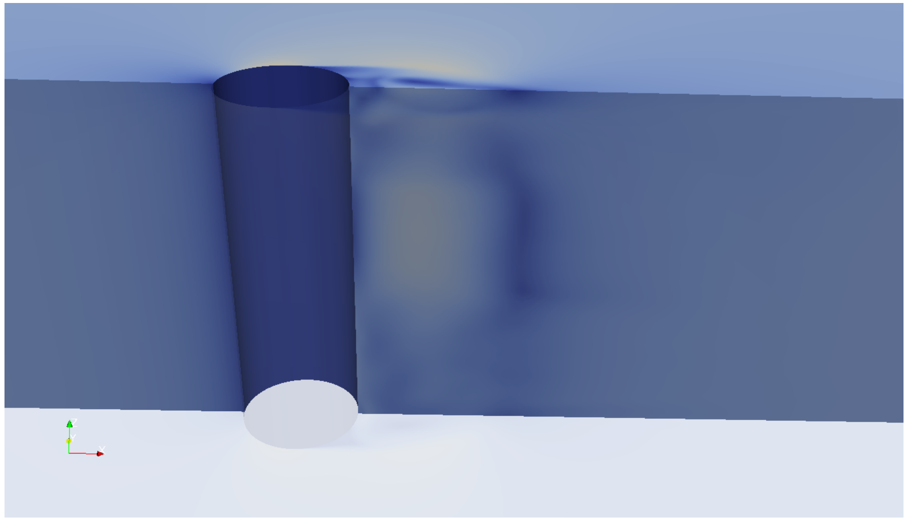

Figure 7.115: Velocity $SR \sim 0$ $t = 0.4s$.

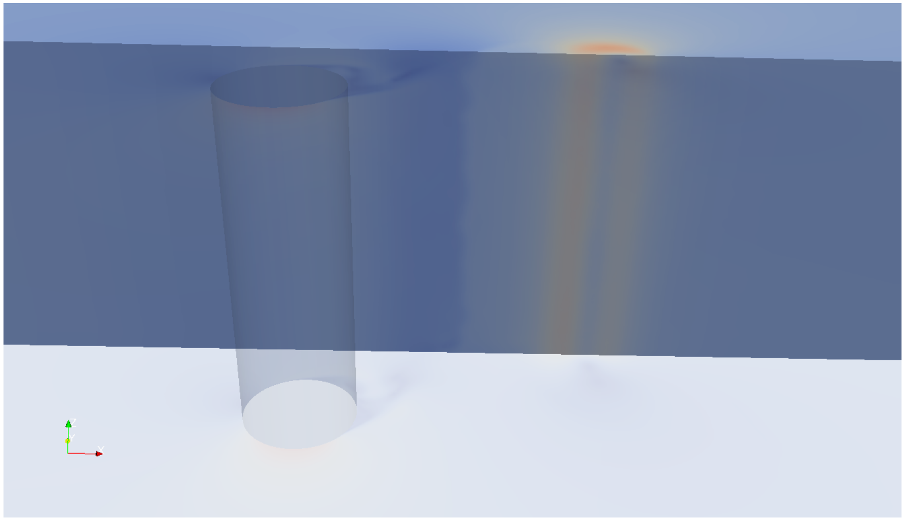

Figure 7.116: Velocity $SR \sim 1$ $t = 0.4s$.

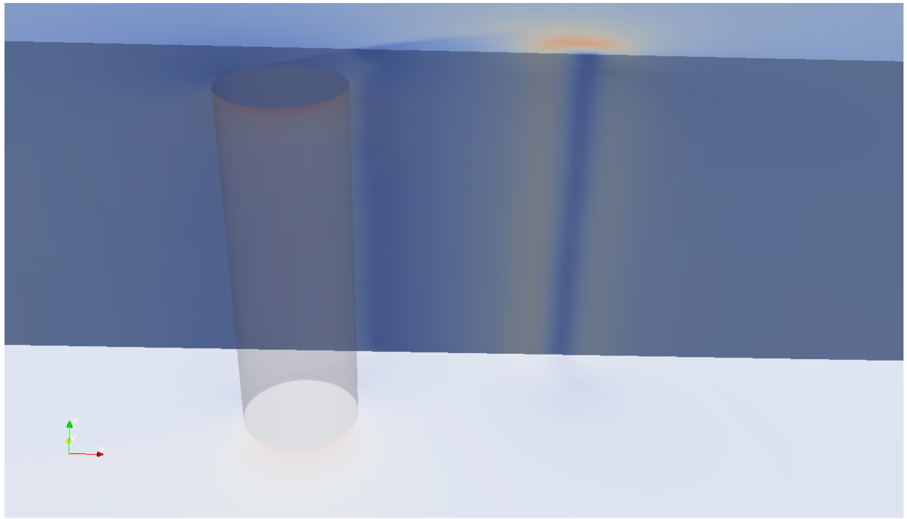

Figure 7.117: Velocity $SR \sim 2$ $t = 0.4s$.

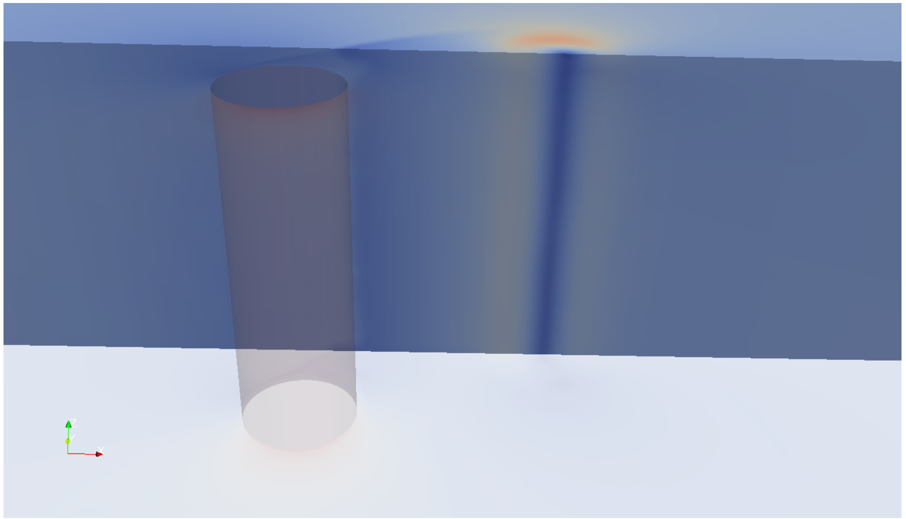

Figure 7.118: Velocity $SR \sim 2.5$ $t = 0.4s$.

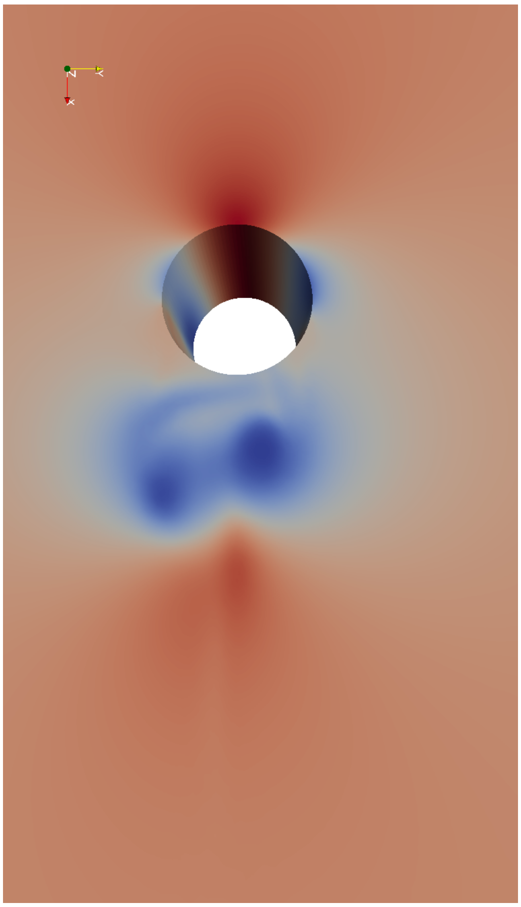

Figure 7.119: Pressure $SR \sim 0$ $t = 0.4s$.

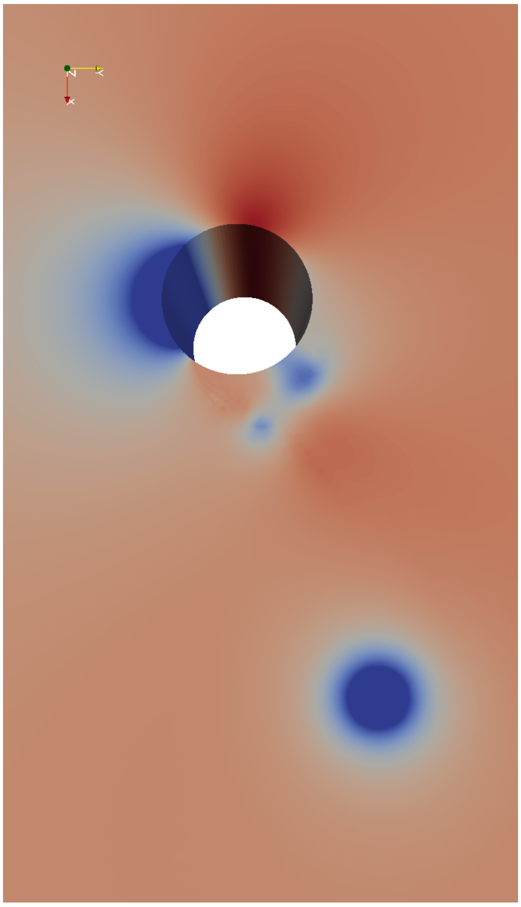

Figure 7.120: Pressure $SR \sim 1$ $t = 0.4s$.

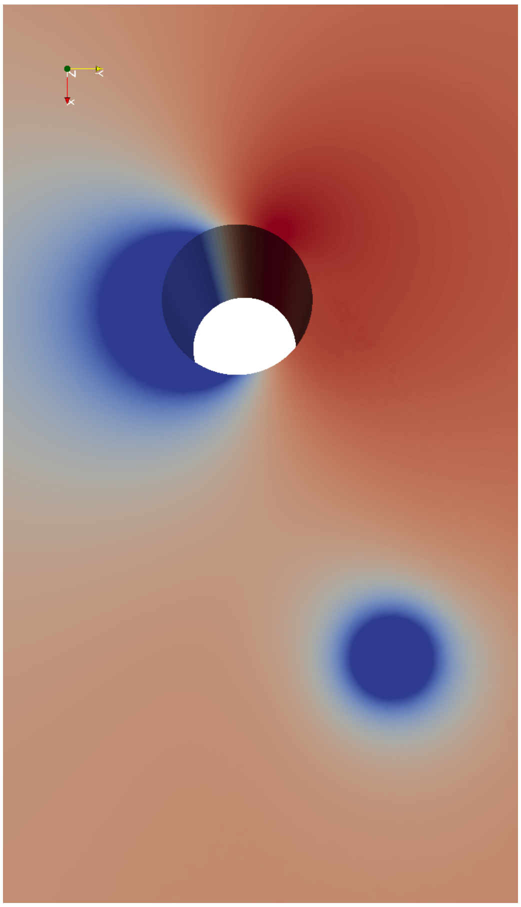

Figure 7.121: Pressure $SR \sim 2$ $t = 0.4s$.

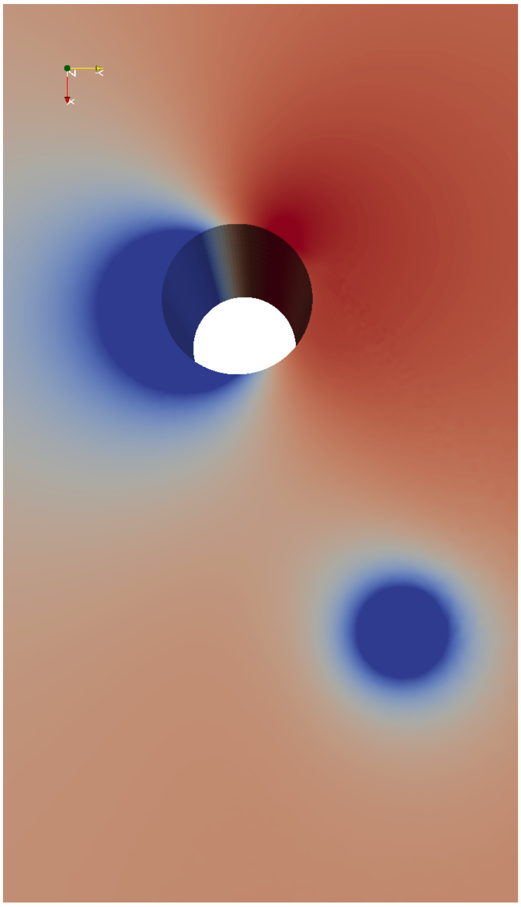

Figure 7.122: Pressure $SR \sim 2.5$ $t = 0.4s$.

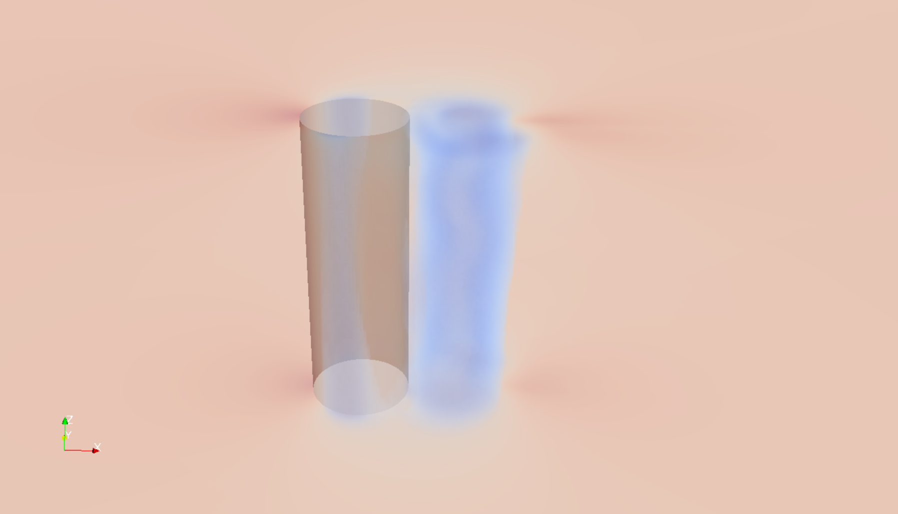

Figure 7.123: Pressure $SR \sim 0$ $t = 0.4s$.

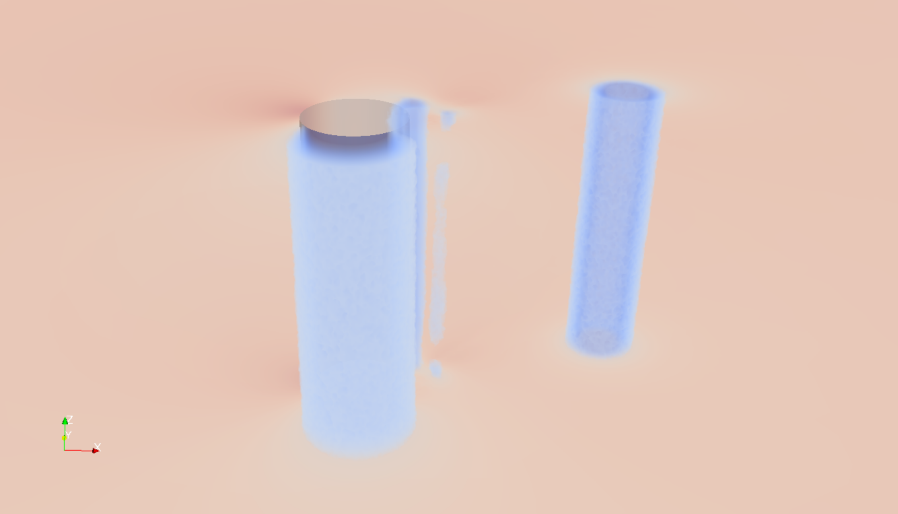

Figure 7.124: Pressure $SR \sim 1$ $t = 0.4s$.

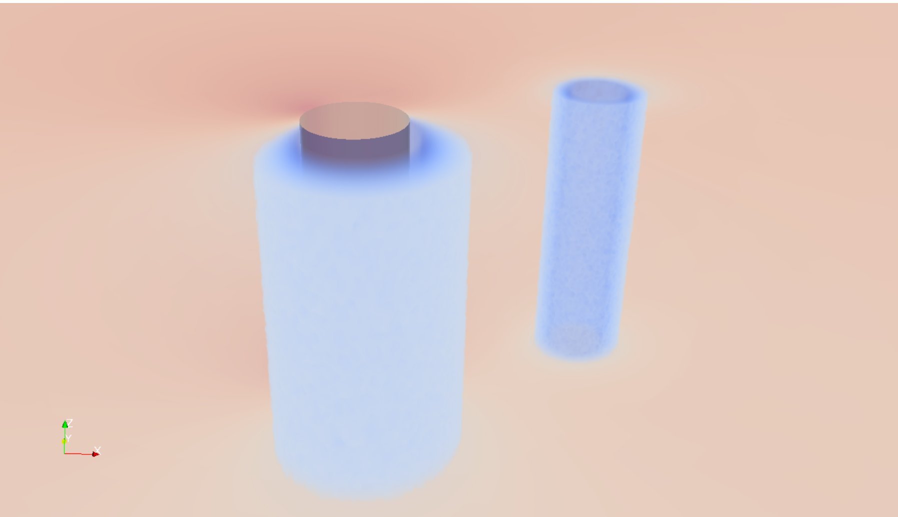

Figure 7.125: Pressure $SR \sim 2$ $t = 0.4s$.

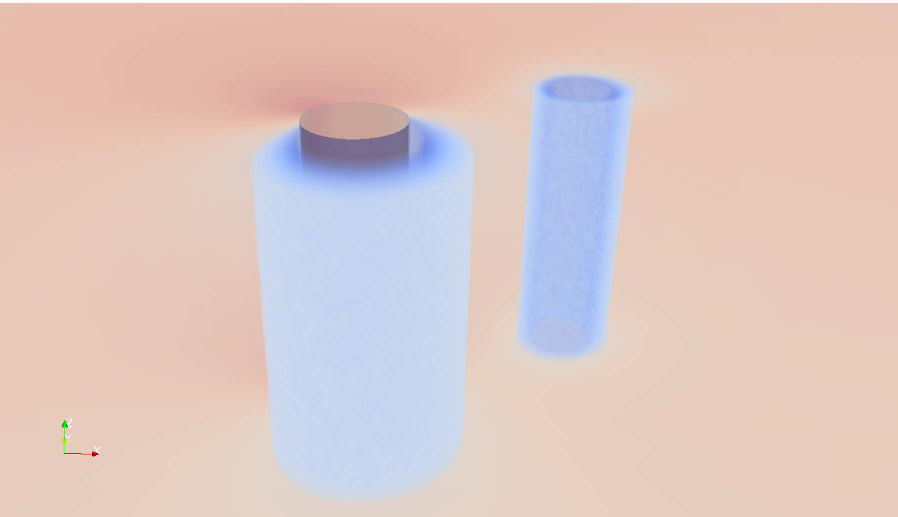

Figure 7.126: Pressure $SR \sim 2.5$ $t = 0.4s$.

8

Conclusion

In this conclusion the answer to the research question will be presented together with a brief discussion about the methods used to answer this question. The mean research question of this thesis is divided into two components which will be discussed here individually.

The first component of the research question is:

"What is the influence of the implementation of a Flettner rotor on an Exploration cruise vessel with respect to the roll motion?".

This question is answered by determining the external moment excited by the Flettner rotor and the RAO of the vessel in combination with two sea states.

The influence of the Flettner rotor on the roll motion of the cruise vessel consists of two components. The first component resulting from the Flettner rotor implementation is a constant heeling moment acting on the vessel. This constant heeling moment is only dependent on the wind and sailing velocity, and can be compensated by, for example, ballast tanks.

The second component is a fluctuating moment in time, induced by the Flettner rotor as a result of the roll velocity of the vessel. This moment is in phase with the roll velocity of the vessel and will assist in damping the roll motion for roll frequencies around the natural frequency. For the research conditions, the significant roll amplitude was reduced by 0.27° for the natural roll frequency after the implementation of the Flettner rotor. It is not likely that the cruise vessel will encounter a wave with a period of 19.3s (T_0), therefore the influence of the Flettner rotor is also evaluated for a more probable sea state. For a sea state with a wave period of 8.8s, the significant roll amplitude is increased by 0.04°. The calculation methods used contain linearizations that render such small differences in the significant roll angle negligible.

This leads to the following answer for the first part of the research question: The Flettner rotor will induce a constant heeling moment and contribution to the damping of the roll motion up to $\omega \approx 0.4 \frac{rad}{s}$.

The second part of the mean research question is presented in the thesis as:

"What is the influence of the implementation of a Flettner rotor on a Exploration cruise vessel with respect to the superstructure-rotor interaction?"

To answer this part of the research question, five CFD simulations were performed. Four for an increasing rotational velocity of the rotor and one containing the rotor with the highest rotational velocity, including a superstructure in its wake. An evaluation of the flow around the rotors with increasing rotational velocities was included in the results after the drag crisis was observed for the rotor. This was considered important enough for the implementation of a Flettner rotor to extend the scope. The simulations are verified by a grid independence study and validated using existing researches.

After the implementation of the Flettner rotor the superstructure interaction will be most significant for the lowest two rotational velocities of the rotor (SR~ 0&1). For those two rotational velocities, the higher levels of turbulent kinetic energy are located in the wake of the rotor and fluctuate in magnitude and direction over the height of the rotor. When the apparent wind is increasing in strength it may be beneficial to give the Flettner rotor a rotational velocity, even when it is not used for propulsion purposes. The wake and loads excited by the rotor then become more stable and controllable.

For the highest two rotational velocities (SR$\sim$ 2&2.5), the drag crisis was observed. This causes the higher levels of turbulent kinetic energy to relocate near the surface of the rotor. The drag produced by the Flettner rotor is thereby dominated by wall shear stresses instead of vortex formation. Vortex formation by the Flettner rotor is suppressed for these rotational velocities because of the drag crisis. The presence of the superstructure in the wake of the rotor for these higher rotational velocities is mainly seen back in the magnitude of the produced lift. The lift production decreases because the pressure distribution around the superstructure influences the wake of the rotor.

The second part of the research question can be answered by: When for spin ratio's lower than two the superstructure is located closer to the rotor than three times its diameter, interaction will occur. This interaction consists of fluctuating loads, in direction and magnitude, acting on the superstructure, a reduction in the produced lift and a change in produced drag. For spin ratio's larger than 2, the placement of the superstructure in that range near the rotor will only lead to a reduction in lift production.

9

Discussion and recommendations

This chapter will be divided into two parts; the first concerns the influence of the Flettner rotor on the roll motion. The second part concerns, the rotor-superstructure interaction. For each part the presented calculation methods and their results will be discussed followed by recommendations for further research.

9.1. Influence Flettner rotor on roll motion

To answer how the implementation of the Flettner rotor influences the roll motion of the vessel a few decisions were made, while setting up the calculation methods, that induce uncertainty. These decisions are presented underneath:

- The lift produced by the rotor is determined by using the Kutta Joukowski method; a linear method only delivering the lift produced by a rotating cylinder with the same dimensions as the rotor
- The used equation of motion is linear, neglecting non-linear damping components
- The roll frequency of the vessel is assumed to be the same as the wave frequency; neglecting phase differences and interaction between the vessel and the waves
- The influence of oscillating component of the moment excited by the Flettner rotor is assumed to be equal to its amplitude for each wave frequency
- A limited amount of wave frequencies is used to compose the RAO; more frequencies would result in more accurate results

The usage of the assumptions stated above is justified by the limited amount of time available for this part of the thesis. The results will not have a high level of precision, but they do give an indication of the influence of the Flettner rotor on the roll motion of the vessel. A more accurate way to determine the load and moment excited by the Flettner rotor, is by performing CFD simulations. The CFD simulations performed in this thesis are executed later in time, explaining why their values are not used. They could, in combination with the Morison equation, give an more accurate value of the excited moment by the Flettner rotor *without end-disk*.

From the results, it can be concluded that no further research is necessary into how the Flettner rotor influences the roll motion for the considered vessel and environmental conditions. A higher level of precision and more demanding calculations are not deemed necessary, when the environmental conditions change, for example, when sea states are considered that are highly non-linear. The current conclusions on Flettner rotor implementation cannot be used. The same applies to a change in the vessel properties. The combination of a very light vessel with a large Flettner rotor influences the damping properties of the rotor significantly.

9.2. Flettner rotor-superstructure interaction

To determine the rotor-superstructure interaction on the cruise vessel, CFD simulations were performed. In addition to the uncertainties presented in chapter 6, several assumptions in the creation of the simulations were made. Their influence on the results will be discussed in this section, together with recommendations for further research.

9.2.1. Simulation of the rotor surface

The simulation of the surface of the rotor influences the measured drag load significantly, as is mentioned repeatedly in this thesis. The two main recommendations concerning the simulation of the rotor surface are:

- Wall law usage
- Laminar sublayer consideration

The usage of a wall law will make the results of the simulations more representative for a real Flettner rotor. In addition it will give more insight in the behavior of the turbulent boundary layer when a drag crisis is occurring, presenting valuable information on the performance of the Flettner rotor. However, the magnitude of the interaction between the Flettner rotor and the superstructure is not expected to change because of wall law usage or measurements to decrease the effect of the laminar sublayer. For the most probable working conditions of the Flettner rotor, the higher levels of turbulence are not located in the wake and will not interact with the superstructure. The moment in time for which the drag crisis occurs will change because of the implementation of a wall law; it influences the position of the transition and separation points.

In general, the exact timing of the drag crisis would be an interesting subject for further research, because of its influence on the moment for which rotor-superstructure will occur and on the propulsive properties of the rotor.

9.2.2. Simulated grid

With regard to the used grid for the performed CFD simulations, two recommendations are given:

- Enlargement of the refinement zone
- Simulations for different heights of the rotor; to determine its correlation height

The refinement zone presented for the simulations is too small, as observed in chapter 7. This influences the rotor-superstructure interaction and makes the visual data less reliable. Only a small enlargement of the refinement zone is necessary.

The added value of three dimensional simulations is to capture the fluctuating behavior of the turbulent flow along the height of the rotor, influencing mainly the magnitude of the drag coefficient. When the correlation length of the turbulent fluctuations captured in the simulations is not equal to the rotor height, the added value of three dimensional simulations is reduced. Further research is therefore necessary to validate the right correlation height of the rotor for the solver settings used in this thesis.

9.2.3. Verification and validation

The verification and validation process of a simulation is nearly never finished. When other researches concerning simulations related and comparable to the simulations performed for this thesis are presented in the future, their results should be compared to the current thesis and evaluated to determine their validity.

Further verification concerning the used turbulence model and the chosen closure coefficients is recommended. Simulations with different turbulence models and solvers, like LES and Spalart Allmaras, should be performed, and their results should be compared to the current results to determine the uncertainty induced by the choice for the turbulence model.

A

HydroD input

Here the input data for HydroD is presented in table A.1.

k_{xx}	7.2
k_{yy}	28.34
k_{zz}	28.34
CoG_v	10
CoG_l	53
CoG_t	0

Table A.1: Input data for HydroD.

Since only the roll motion is researched the other angular displacements were set to zero as input values.

A.1. Settings

Here the settings for HydroD are presented.

- MAXIMUM NUMBER OF PANELS =15000
- MAXIMUM NUMBER OF SURFACE PANELS = 3000

(NOTE THAT THIS IS FOR THE BASIC PART OF THE MODEL)

- MAXIMUM NUMBER OF NODES IN THE MORISON MODEL = 5000
- MAXIMUM NUMBER OF ELEMENTS IN THE MORISON MODEL = 5000
- MAXIMUM NUMBER OF SUBELEMENTS IN THE MORISON MODEL WHEN DIFFRACTED WAVE IS USED IN THE MORISON'S EQUATION = 2000
- MAXIMUM NUMBER OF SUBELEMENTS ON ONE MORISON ELEMENT = 5
- MAXIMUM NUMBER OF SUPER ELEMENTS IN THE MORISON MODEL = 1
- MAXIMUM NUMBER OF PANELS COUPLED TO ONE SUBELEMENT = 99
- MAXIMUM NUMBER OF WAVE FREQUENCIES = 60
- MAXIMUM NUMBER OF WAVE HEADINGS = 36
- MAXIMUM NUMBER OF WAVE HEADINGS WHEN ONLY SOLVING THE RADIATION PROBLEM = 36
- MAXIMUM NUMBER OF OFFBODY POINTS = 2000
- MAXIMUM NUMBER OF SECTIONS FOR SECTIONAL LOADS = 25
- MAXIMUM NUMBER OF PHASE ANGLES = 14
- MAXIMUM NUMBER OF CURRENT PROFILES = 1
- MAXIMUM NUMBER OF LEVELS IN ONE CURRENT PROFILE = 30
- NUMBER OF BASIC PANELS GENERATED : 1571
- NUMBER OF PANELS FROM MODIFYING ELEMENTS AT THE STILL WATER LINE OR AT THE SEA BED : 139
- NUMBER OF PANELS FROM MODIFYING AND SPLITTING ELEMENTS AT THE STILL WATER LINE OR AT THE SEA BED : 14
- NUMBER OF ELEMENTS ENCOUNTERED IN THE GIVEN INPUT MODEL : 3394
- NUMBER OF DRY ELEMENTS WITH DEFINED HYDRO-PRESSURE : 1830

B

Wave properties for RAO determination

Here the waves that are used to determine the RAO of roll and the damping moments are presented.

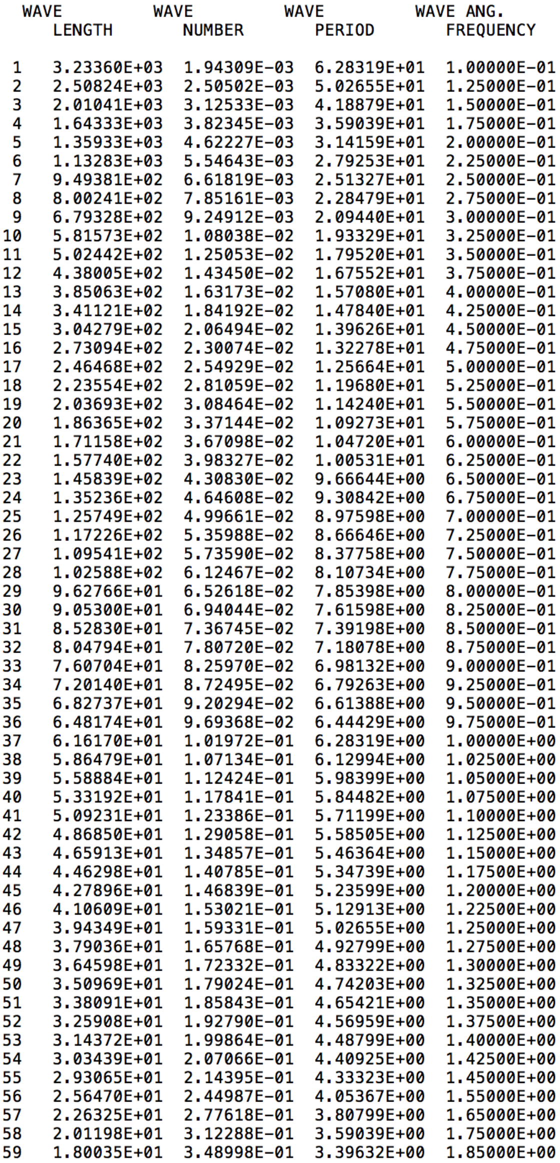

```
   WAVE          WAVE          WAVE          WAVE ANG.
     LENGTH        NUMBER        PERIOD        FREQUENCY

 1   3.23360E+03  1.94309E-03  6.28319E+01  1.00000E-01
 2   2.50824E+03  2.50502E-03  5.02655E+01  1.25000E-01
 3   2.01041E+03  3.12533E-03  4.18879E+01  1.50000E-01
 4   1.64333E+03  3.82345E-03  3.59039E+01  1.75000E-01
 5   1.35933E+03  4.62227E-03  3.14159E+01  2.00000E-01
 6   1.13283E+03  5.54643E-03  2.79253E+01  2.25000E-01
 7   9.49381E+02  6.61819E-03  2.51327E+01  2.50000E-01
 8   8.00241E+02  7.85161E-03  2.28479E+01  2.75000E-01
 9   6.79328E+02  9.24912E-03  2.09440E+01  3.00000E-01
10   5.81573E+02  1.08038E-02  1.93329E+01  3.25000E-01
11   5.02442E+02  1.25053E-02  1.79520E+01  3.50000E-01
12   4.38005E+02  1.43450E-02  1.67552E+01  3.75000E-01
13   3.85063E+02  1.63173E-02  1.57080E+01  4.00000E-01
14   3.41121E+02  1.84192E-02  1.47840E+01  4.25000E-01
15   3.04279E+02  2.06494E-02  1.39626E+01  4.50000E-01
16   2.73094E+02  2.30074E-02  1.32278E+01  4.75000E-01
17   2.46468E+02  2.54929E-02  1.25664E+01  5.00000E-01
18   2.23554E+02  2.81059E-02  1.19680E+01  5.25000E-01
19   2.03693E+02  3.08464E-02  1.14240E+01  5.50000E-01
20   1.86365E+02  3.37144E-02  1.09273E+01  5.75000E-01
21   1.71158E+02  3.67098E-02  1.04720E+01  6.00000E-01
22   1.57740E+02  3.98327E-02  1.00531E+01  6.25000E-01
23   1.45839E+02  4.30830E-02  9.66644E+00  6.50000E-01
24   1.35236E+02  4.64608E-02  9.30842E+00  6.75000E-01
25   1.25749E+02  4.99661E-02  8.97598E+00  7.00000E-01
26   1.17226E+02  5.35988E-02  8.66646E+00  7.25000E-01
27   1.09541E+02  5.73590E-02  8.37758E+00  7.50000E-01
28   1.02588E+02  6.12467E-02  8.10734E+00  7.75000E-01
29   9.62766E+01  6.52618E-02  7.85398E+00  8.00000E-01
30   9.05300E+01  6.94044E-02  7.61598E+00  8.25000E-01
31   8.52830E+01  7.36745E-02  7.39198E+00  8.50000E-01
32   8.04794E+01  7.80720E-02  7.18078E+00  8.75000E-01
33   7.60704E+01  8.25970E-02  6.98132E+00  9.00000E-01
34   7.20140E+01  8.72495E-02  6.79263E+00  9.25000E-01
35   6.82737E+01  9.20294E-02  6.61388E+00  9.50000E-01
36   6.48174E+01  9.69368E-02  6.44429E+00  9.75000E-01
37   6.16170E+01  1.01972E-01  6.28319E+00  1.00000E+00
38   5.86479E+01  1.07134E-01  6.12994E+00  1.02500E+00
39   5.58884E+01  1.12424E-01  5.98399E+00  1.05000E+00
40   5.33192E+01  1.17841E-01  5.84482E+00  1.07500E+00
41   5.09231E+01  1.23386E-01  5.71199E+00  1.10000E+00
42   4.86850E+01  1.29058E-01  5.58505E+00  1.12500E+00
43   4.65913E+01  1.34857E-01  5.46364E+00  1.15000E+00
44   4.46298E+01  1.40785E-01  5.34739E+00  1.17500E+00
45   4.27896E+01  1.46839E-01  5.23599E+00  1.20000E+00
46   4.10609E+01  1.53021E-01  5.12913E+00  1.22500E+00
47   3.94349E+01  1.59331E-01  5.02655E+00  1.25000E+00
48   3.79036E+01  1.65768E-01  4.92799E+00  1.27500E+00
49   3.64598E+01  1.72332E-01  4.83322E+00  1.30000E+00
50   3.50969E+01  1.79024E-01  4.74203E+00  1.32500E+00
51   3.38091E+01  1.85843E-01  4.65421E+00  1.35000E+00
52   3.25908E+01  1.92790E-01  4.56959E+00  1.37500E+00
53   3.14372E+01  1.99864E-01  4.48799E+00  1.40000E+00
54   3.03439E+01  2.07066E-01  4.40925E+00  1.42500E+00
55   2.93065E+01  2.14395E-01  4.33323E+00  1.45000E+00
56   2.56470E+01  2.44987E-01  4.05367E+00  1.55000E+00
57   2.26325E+01  2.77618E-01  3.80799E+00  1.65000E+00
58   2.01198E+01  3.12288E-01  3.59039E+00  1.75000E+00
59   1.80035E+01  3.48998E-01  3.39632E+00  1.85000E+00
```

Figure B.1: The waves used as input for HydroD, the RAO and damping moment calculations.

C

Drag crisis

The drag crisis origins from the unstable separated shear layer that starts to form when Re increases together with small vortices, resulting from the instability. The instability of the shear layer increases in strength with increasing Re and the transition point where the shear layer becomes unstable moves upstream [37]. The drag crisis is caused by this phenomena when the separation point of the shear layer is located upstream from the region where the flow is "traditional" unseparated [24]. The reattachment of the boundary can be seen in the second image in figure C.1. The shear layer reattaches because the eddies of the shear layer cause mixing of the boundary layer with the outer flow. Singh et al. [37] states that the transition of the boundary layer, and therefore the drag crisis, is dependent on the stability of the detached shear layer. In figure C.1 the first image depicts the sub-critical flow. Here the instability of the detached shear layer occurs when the shear layer is far away enough form the boundary layer of the rotor and does not reattach. At the critical Reynolds number the detached shear layer is earlier unstable and mixes with the boundary layer. Explained earlier in this section. The mixing of the shear layer and the boundary layer causes the boundary layer to become turbulent instead of laminar. This is shown in the second image of figure C.1. The reattached flow separates again and becomes unstable downstream of the cylinder causing the *drag crisis.* The point of detachment of the reattached shear layer moves upstream for increasing Re causing the entire boundary layer of the cylinder to be turbulent. Because the boundary layer is turbulent the skin friction (turbulent shear stresses) increases and the drag experienced by the rotor increases again.

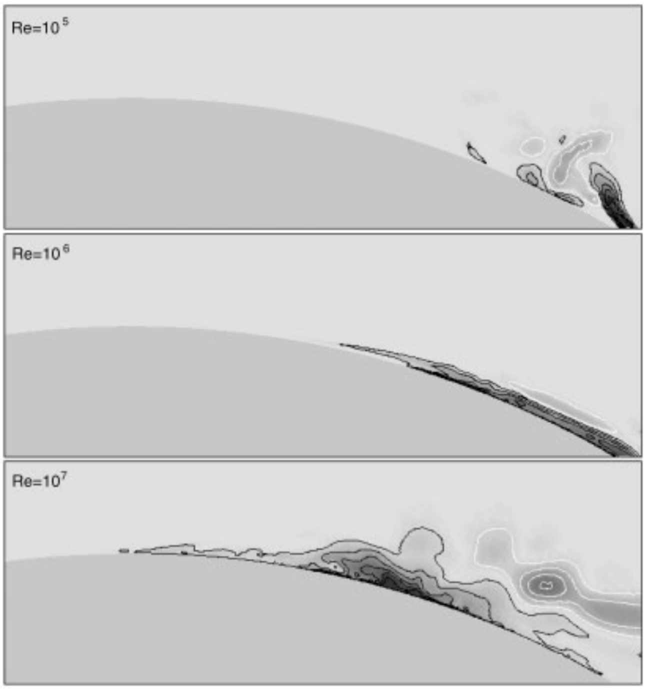

Figure C.1: Close up view of the flow around a cylinder at three Re, the flow is shown by the velocities (u'v') averaged over one shear layer cycle [37].

D

CFD simulation background

In this appendix the equations and principles that are used to set up the CFD simulations are explained.

D.1. Continues Navier Stokes equations

The continuous NS equations are shown in equations D.1 and D.2. Their full derivation will not be given but a explanation of what the components represent will be.

$$\nabla\cdot U=0 \tag{D.1}$$

U represents the velocity vector with as its three components the velocities in x-, y- and z-direction. Equation D.1 shows that the gradient of the velocities is equal to zero. Meaning that the flow is incompressible[1]. Which is equal to the divergence of the dynamic viscosity $\left(div\ \mu=0\right)$.

$$\frac{\partial\left(\rho U\right)}{\partial t}+\nabla\cdot\left(\left(\rho U\right)\otimes U\right)-\nabla\cdot\left(\mu\nabla U\right)+\nabla p-\rho g=0 \tag{D.2}$$

The first two components of equation D.2 represent the acceleration of a "flow particle". The last three components represent the forces acting on the particle. The forces that are considered are viscous forces, pressure forces and body forces. The viscous forces comprehend the stresses acting on the considered body in normal and tangential directions. The stresses are presented by a viscous stress tensor assumed proportional to a rate of strain tensor. The dynamic viscosity (μ) represents the proportionality in the NS equations. Which is clearer when the units of μ are given: $N\frac{s}{m^2}$. The shear stress $\left(\frac{N}{m^2}\right)$ per shear rate $\left(\frac{1}{s}\right)$.

$$\nabla\cdot U^{n+1}=0 \tag{D.3}$$

$$\frac{U^{n+1}-U^{n}}{\Delta t}+\left(U^{n}\cdot\nabla\right)U^{n}=-\frac{1}{\rho}p^{n+1}+\nu\Delta U^{n}+g \tag{D.4}$$

On a grid the continuous Navier Stokes equation can not be used. The formulation needs to be discrete (dependent on the time integration scheme): U^{n+1} becomes dependent on U^{n}. In equation D.4 $-\frac{1}{\rho}p^{n+1}$ is not solved in the previous step and can therefore be solved implicitly and explicitly. In the explicit solver U^{n+1} is dependent on $F\left(U^{n}\right)$ so based on the time step before. When dependent variables can be determined based on known quantities, a direct computation can be performed. In this direct computations the variables are defined with a set of equations and a iterative process can be used to determine the answer. Solving a equation in that way is called implicit. In other words; the implicit solver U^{n+1} is dependent on $F\left(U^{n+1}\right)$.equation is solves in the same time step.

D.1.1. Implicit solver

To solve the discreet NS equation implicitly the pressure component stays included in the equation even though it does not comply with the velocity components at U^{n+1}. There is a subcycle ($+\alpha$) added, where at $\alpha=0$ it becomes the original cycle. So for $\alpha=1$ $U^{n+1}=\tilde{U}$. There is no limitation to the time step so the time step becomes dependent on the time scale you want it to converge. The implicit scheme gives a second order

---

[1] Total net transport of mass is zero in the absence of mass sources

equation so it is more accurate than the explicit scheme but more likely to be unstable. Because of the larger time step that can be used. When using larger time steps the formulation needs to be verified thoroughly to maintaining to be realistic. The implicit scheme uses more computational time for each solution step compared to the explicit scheme.

D.1.2. Explicit solver

In the explicit solver the pressure component $\frac{\nabla p^{n+1}}{\rho}$ is not solved in the first step; because $n+1$ cannot be determined, there is no relation between $\nabla U^{n+1} = 0$ and $\frac{\nabla p^{n+1}}{\rho}$. To solve the first equation a prediction will be made and afterwards a correction will be performed. First the density advection is determined (D.5) where after the momentum equation is applied (D.6).

$$\frac{\tilde{\rho} - \rho}{\partial t} + \nabla \cdot \left(\rho U^n \right) = 0 \tag{D.5}$$

$$\frac{\widetilde{\rho U} - rhoU^n}{\partial t} + \nabla \cdot \left(\rho U^n \otimes U^n \right) = \nabla \cdot \left(\mu \nabla U^n \right) = 0 \tag{D.6}$$

Then the pressure can be updated (D.7) to project U^{n+1} (D.8).

$$\nabla \cdot \left(\frac{1}{\rho} \nabla \left(\partial t p^{n+1} \right) \right) = \nabla \cdot \left(\tilde{U} + \partial t g \right) \tag{D.7}$$

$$U^{n+1} = \tilde{U} - \partial t P \left(\frac{1}{\rho} \nabla p^{n+1} \right) \tag{D.8}$$

When the time step becomes too high the results will diverge.

E

Motion calculations

The linear equation of motion is shown in equation E.1.

$$I_{44}\ddot{\phi} + B_{44}\dot{\phi} + C_{44}\phi = M\left(\phi\right) \tag{E.1}$$

The inertia coefficient, damping coefficient and restoring coefficient are all independent of the roll angle. No external conditions are considered beside the exciting wave and wind. The nonlinear equation of motion, as presented by Taylan [41], is shown in equation E.2.

$$I\ddot{\phi} + B\left(\dot{\phi}\right) + C\left(\phi\right) = M\left(\phi\right) \tag{E.2}$$

The nonlinear terms are the damping moment and the restoring moment ($C\left(\phi\right)$); they are dependent on the roll velocity and angle. This equation can be rewritten in the form of equation E.3 where $\dot{\phi}$ is included so that the damping moment ($B\left(\phi\right)$) will always oppose the motion of the vessel.

$$\begin{aligned}\left(I_{xx} + \delta I_{xx}\right)\ddot{\phi} + B_1\dot{\phi} + B_2\dot{\phi}|\dot{\phi}| + \Delta\left(C_1\phi + C_3\phi^3 + C_5\phi^5\right) = \\ w_0^2\alpha_m I_{xx}\cos\left(w_0 t\right)\end{aligned} \tag{E.3}$$

For this equation the most important assumptions are [41]:

- The added mass moment of inertia is independent of the heel angle
- The displacement is considered constant
- Only the uncoupled roll motion is considered
- The damping term is considered quadratic
- The nonlinear terms are considered small

The maximum roll angle will result out of the equalibrium between the linear equation of motion and the external moment. When the maximum roll angle appears to be small then the nonlinear terms are considered small [22] [19] [41] [16]. The terms of the nonlinear equation of motion will be explained underneath. They represent the same as the terms of the linear equation of motion but include other effects and have different dependencies as shown in the following sections.

E.1. Inertia moment

The inertial moment consist out of the inertia and the added mass of the vessel, and is considered independent on the roll acceleration. The added mass is considered to not dissipate energy from the motion and to produce a standing wave system near the vessel [22].

E.2. Gyroscopic effect

Including the rotor, in the equation of motion, changes the inertial moment by adding mass to the inertial mass moment (I). There is another inertia related term that is added to the equation of motion; the gyroscopic effect $\left(L\left(\dot{\phi}\right)\right)$. This effect is dependent on the roll angular velocity ($\dot{\phi}$) and is caused by giving a rotational velocity to a already spinning object. Because it is dependent on the angular velocity of the roll motion the gyroscopic term will be superimposed in the nonlinear damping moment as a first order term. The direction of the excited load by the gyroscopic effect is directed perpendicular to the rotational velocity; the roll motion.

E.3. Nonlinear damping moment

The nonlinear damping moment is given by equation E.4, where the damping moment can be described as a dependency of the resistance of the body to the motion of the vessel. For small amplitudes of the roll motion the damping term may be considered a linear function; B_2 becomes zero. The damping coefficient is a function of the sailing speed, the frequency of the roll motion and the amplitude of the roll motion. The damping coefficient consists out of the following components:

- Wave making damping
- Skin friction damping
- Eddy-making damping
- Lift damping
- Bilge keel damping

The components that depend on the roll amplitude are considered nonlinear; the skin friction damping and the Eddy-making damping. In the Eddy-making damping the hull and the appendages are included.

$$B_{44}\dot{\phi} = B_1\dot{\phi} + B_2\dot{\phi}|\dot{\phi}| \tag{E.4}$$

The gyroscopic effect can also be superimposed in the damping moment, shown in E.5. The direction will be perpendicular to the applied motion; not influencing the roll motion. *The gyroscopic effect will not be included in the damping term in this research.*

$$B_{44}\dot{\phi} = B_1\dot{\phi} + B_2\dot{\phi}|\dot{\phi}| + L\dot{\phi} \tag{E.5}$$

E.4. Nonlinear restoring moment

The restoring moment is equal to the righting arm GZ multiplied with the displacement. The non-linearity of the restoring moments results in the polynomial that is fitted to the GZ curve. This is represented in equation E.6.

$$GZ = C_1\phi + C_3\phi^3 + C_5\phi^5 \tag{E.6}$$

The coefficients in equation E.6 are dependent on GM, the angle of vanishing stability and the area under the GZ curve [41]. This formulation can be used for a vessel in waves when the influence of the waves on the position of the center of buoyancy and the metacenter is included.

E.5. Linear or nonlinear equation of motion

The difference between the linear and non linear equation of motion is the dependency on the roll angle (ϕ_4). When the maximum roll angle is small enough the nonlinear terms become small enough to be neglected. The largest roll amplitude is expected at resonance; the critical condition for the roll amplitude. The roll angle at resonance is expected to be smaller than 10 deg. For that order of magnitude of roll angle the linear equation of motion can be used.

F

HydroD check

Here the calculations will be presented that were used to check the HydroD calculations.

Gerritsma [17] gives an estimation of the natural frequency F.1 and natural period F.2 for the roll motion. The interaction between the roll and other motions of the vessel are neglected.

$$\omega_{0\phi} = \sqrt{\frac{\rho g \nabla GM}{k_{xx}^2 \rho \nabla + m_{\phi\phi}}} \tag{F.1}$$

$$T_{0\phi} = 2\pi \sqrt{\frac{k_{xx}^2 \rho \nabla + m_{\phi\phi}}{\rho g \nabla GM}} \tag{F.2}$$

Gerritsma presents apparent transverse radius of gyration ($k_{\phi\phi}$) for passenger vessels with a value of $k_{\phi\phi} = 0.35B$ to $k_{\phi\phi} = 0.45B$. Using the apparent transverse radius of gyration the natural period can be determined with F.4 and following the natural frequency with F.3.

$$T_{0\phi} \approx \frac{2k_{\phi\phi}}{\sqrt{GM}} \tag{F.3}$$

$$\omega_{0\phi} \approx \frac{2\pi}{T_{0\phi}} \tag{F.4}$$

The value for GM is determined by $KM - CoG_v = 0.756\ m$. Resulting in $T_{0\phi} = 20\ s$ and $\omega_{0\phi} = 0.30\ \frac{rad}{s}$. The high value for the roll period will result in lower velocities around the rotor compared to higher roll periods, this will influence how the roll motion will change the direction of the lift and drag load excited by the rotor. For longer roll periods the influence by the roll motion will be less.

The natural frequency determined for the roll motion is given to the incoming beam wave for the vessel. By choosing this property the roll motion of the vessel is actually evaluated in still water. An estimation of the restoring coefficient ($c_{\phi\phi}$) is given by Journee et al. [22] as equation F.5.

$$c_{\phi\phi} = \rho g \nabla \cdot GM = 6.55e7\ \frac{N}{rad} \tag{F.5}$$

Ulstein has delivered the moment to change trim for a draught of 5 m as 154.3 $\frac{tm}{cm}$ which can be rewritten to $1.51e7\ \frac{N}{rad}$, which is of the same order of magnitude as the formulation given by Journee et al..

G

Solver input

Here the functions and input values for the solver used for the CFD simulations will be presented.

G.1. Functions

To dictate a rotational velocity to the vertices on the boundary of the cylinder two python scrips were written. The first function is created for a *SR* ~ 2:

```
#include <vector>
  #include <math.h>
  #include <fstream>
  #include <iostream>

  /*! Defined velocity of the wall during the time in each point.
  Input :
  @value t : represents the time value.
  @value x : represents the x-coordinate.
  @value y : represents the y-coordinate.
  @value z : represents the z-coordinate.
  Output :
  This function return the velocity of the wall,
  @value vx : velocity along Ox direction.
  @value vy : velocity along Oy direction.
  @value vz : velocity along Oz direction.

*/

using namespace std;
void exit_ananas(const int errorNumber,const string specificMsg, const int processID
    =-1);

void ufmvgboundary(const double t,const double x,const double y,
                   const double z,const double deltat,
                   vector< vector <double > >& array,
                   double& vx,double& vy,double& vz)
{
if (x-16.5<0.0) {
        vx = -24.9*sin(atan((y-20.5)/(x-16.5))+3.1415926535897);
        vy = 24.9*cos(atan((y-20.5)/(x-16.5))+3.1415926535897);
        vz = 0.0;
}
else{
        vx = -24.9*sin(atan((y-20.5)/(x-16.5)));
        vy = 24.9*cos(atan((y-20.5)/(x-16.5)));
        vz = 0.0;
```

```
} }
```

The second function is for a $SR \sim 2.5$, with an object in the wake:

```
#include <vector>
  #include <math.h>
  #include <fstream>
  #include <iostream>

  /*! Defined velocity of the wall during the time in each point.
  Input :
  @value t : represents the time value.
  @value x : represents the x-coordinate.
  @value y : represents the y-coordinate.
  @value z : represents the z-coordinate.
  Output :
  This function return the velocity of the wall,
  @value vx : velocity along Ox direction.
  @value vy : velocity along Oy direction.
  @value vz : velocity along Oz direction.

*/

using namespace std;
void exit_ananas(const int errorNumber,const string specificMsg, const int processID
    =-1);

void ufmvgboundary(const double t,const double x,const double y,
                   const double z,const double deltat,
                   vector< vector <double > >& array,
                   double& vx,double& vy,double& vz)
{
        vx = 31.13*(y-20.5)/0.5;
        vy = -31.13*(x-16.5)/0.5;
        vz = 0.0;
}
```

It can be seen that the first function rotates in a counterclockwise direction and the second in the clockwise direction. The second function is a simplified version of the first function. That the rotation is constant over the entire boundary of the cylinder can be seen in figure G.1.

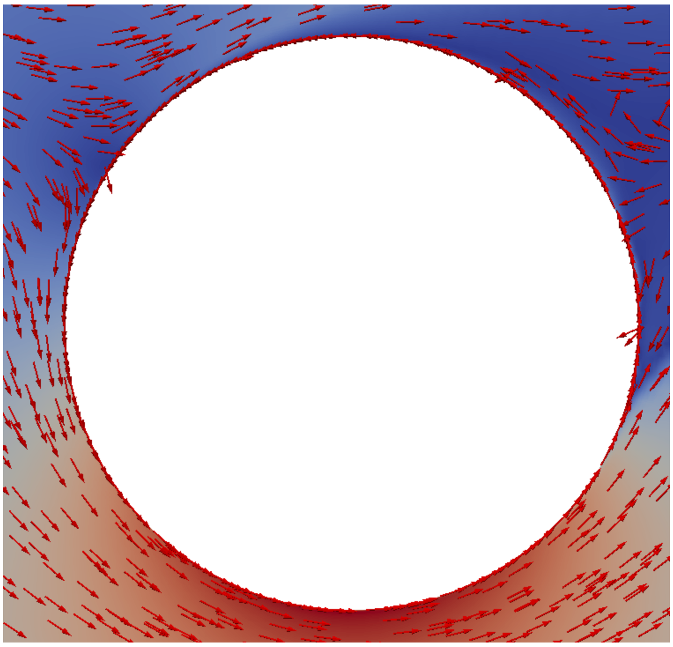

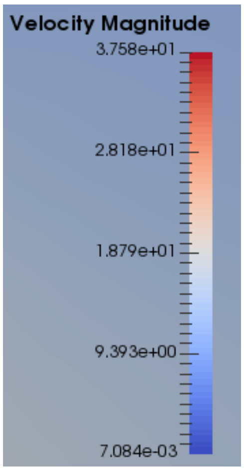

Figure G.2: Scale belonging to the flow in figure G.1, excluding the velocity vectors.

Figure G.1: Rotational direction for $SR \sim 2$; the red arrows show the scaled velocity vectors of selected nodes.

G.2. Boundary thickness

Here the excel (figure G.3) is presented in which the boundary layer thickness is presented and the number of layers.

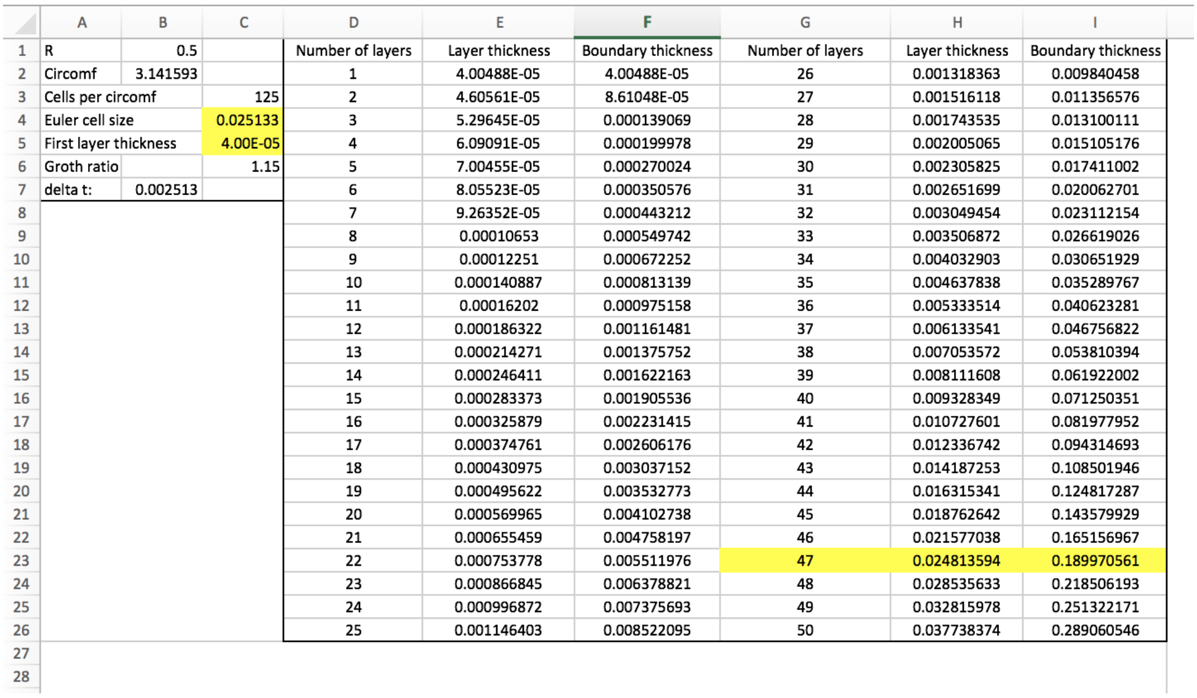

	A	B	C	D	E	F	G	H	I
1	R	0.5		Number of layers	Layer thickness	Boundary thickness	Number of layers	Layer thickness	Boundary thickness
2	Circomf	3.141593		1	4.00488E-05	4.00488E-05	26	0.001318363	0.009840458
3	Cells per circomf		125	2	4.60561E-05	8.61048E-05	27	0.001516118	0.011356576
4	Euler cell size		0.025133	3	5.29645E-05	0.000139069	28	0.001743535	0.013100111
5	First layer thickness		4.00E-05	4	6.09091E-05	0.000199978	29	0.002005065	0.015105176
6	Groth ratio		1.15	5	7.00455E-05	0.000270024	30	0.002305825	0.017411002
7	delta t:	0.002513		6	8.05523E-05	0.000350576	31	0.002651699	0.020062701
8				7	9.26352E-05	0.000443212	32	0.003049454	0.023112154
9				8	0.00010653	0.000549742	33	0.003506872	0.026619026
10				9	0.00012251	0.000672252	34	0.004032903	0.030651929
11				10	0.000140887	0.000813139	35	0.004637838	0.035289767
12				11	0.00016202	0.000975158	36	0.005333514	0.040623281
13				12	0.000186322	0.001161481	37	0.006133541	0.046756822
14				13	0.000214271	0.001375752	38	0.007053572	0.053810394
15				14	0.000246411	0.001622163	39	0.008111608	0.061922002
16				15	0.000283373	0.001905536	40	0.009328349	0.071250351
17				16	0.000325879	0.002231415	41	0.010727601	0.081977952
18				17	0.000374761	0.002606176	42	0.012336742	0.094314693
19				18	0.000430975	0.003037152	43	0.014187253	0.108501946
20				19	0.000495622	0.003532773	44	0.016315341	0.124817287
21				20	0.000569965	0.004102738	45	0.018762642	0.143579929
22				21	0.000655459	0.004758197	46	0.021577038	0.165156967
23				22	0.000753778	0.005511976	47	0.024813594	0.189970561
24				23	0.000866845	0.006378821	48	0.028535633	0.218506193
25				24	0.000996872	0.007375693	49	0.032815978	0.251322171
26				25	0.001146403	0.008522095	50	0.037738374	0.289060546
27									
28									

Figure G.3: Excel to determine boundary thickness and number of layers.

H

Matlab code

In this appendix the relevant Matlab code will be presented.

H.1. Loading CFD probe data and filtering

```
%close all
clc
clear all
close all
%% Cylinder and flow properties
rho = 1.225;                    % Density of air
D = 1;                          % Diameter
H = 3*D;                        % Heigth
A = D*H;                        % Surface perpendiculair to the flow direction
u = 12.45;                      % Vertical velocity

Kin_vis = 1.3878e-5;
Re = (u*D)/Kin_vis;

Figure = false;
Non_Rotating = true;
Rotating = false;
Filter = true;

%% Import data
if Non_Rotating
t1 = xlsread('P1.xlsx','A:A');
t1_nond = t1.*(u/D);
Drag1 = xlsread('P1.xlsx','B:B');
Lift1 = xlsread('P1.xlsx','C:C');
Cd1 = (2*Drag1)/(rho*u^2*A);
Cl1= (2*Lift1)/(rho*u^2*A);
T1 = sqrt(Drag1.^2+Lift1.^2);

t = xlsread('P2.xlsx','A:A');
t_nond = t.*(u/D);
Drag = xlsread('P2.xlsx','B:B');
Lift = xlsread('P2.xlsx','C:C');
Cd = (2*Drag)/(rho*u^2*A);
Cl= (2*Lift)/(rho*u^2*A);
T = sqrt(Drag.^2+Lift.^2);

t3 = xlsread('P3.xlsx','A:A');
```

```
t3_nond = t3.*(u/D);
Drag3 = xlsread('P3.xlsx','B:B');
Lift3 = xlsread('P3.xlsx','C:C');
Cd3 = (2*Drag3)/(rho*u^2*A);
Cl3= (2*Lift3)/(rho*u^2*A);
T3 = sqrt(Drag3.^2+Lift3.^2);
end
if Rotating
t_8 = xlsread('FOB7_8.4.xlsx','A:A');
t_8_nond = t_8.*(u/D);
Drag_8 = xlsread('FOB7_8.4.xlsx','B:B');
Lift_8 = xlsread('FOB7_8.4.xlsx','C:C');
Cd_8 = (2*Drag_8)/(rho*u^2*A);
Cl_8 = (2*Lift_8)/(rho*u^2*A);
T_8 = sqrt(Drag_8.^2+Lift_8.^2);

t_12 = xlsread('FOB7_12.45.xlsx','A:A');
t_12_nond = t_12.*(u/D);
Drag_12 = xlsread('FOB7_12.45.xlsx','B:B');
Lift_12 = xlsread('FOB7_12.45.xlsx','C:C');
Cd_12 = (2*Drag_12)/(rho*u^2*A);
Cl_12 = (2*Lift_12)/(rho*u^2*A);
T_12 = sqrt(Drag_12.^2+Lift_12.^2);

t_24 = xlsread('FOB7_24.9_new.xlsx','A:A');
t_24_nond = t_24.*(u/D);
Drag_24 = xlsread('FOB7_24.9_new.xlsx','B:B');
Lift_24 = xlsread('FOB7_24.9_new.xlsx','C:C');
Cd_24 = (2*Drag_24)/(rho*u^2*A);
Cl_24 = (2*Lift_24)/(rho*u^2*A);
T_24 = sqrt(Drag_24.^2+Lift_24.^2);

t_31 = xlsread('FOB7_31.13.xlsx','A:A');
t_31_nond = t_31.*(u/D);
Drag_31 = xlsread('FOB7_31.13.xlsx','B:B');
Lift_31 = xlsread('FOB7_31.13.xlsx','C:C');
Cd_31 = (2*Drag_31)/(rho*u^2*A);
Cl_31 = (2*Lift_31)/(rho*u^2*A);
T_31 = sqrt(Drag_31.^2+Lift_31.^2);

t_O = xlsread('FOB8_31.13.xlsx','A:A');
t_O_nond = t_O.*(u/D);
Drag_O = xlsread('FOB8_31.13.xlsx','B:B');
Lift_O = -1*xlsread('FOB8_31.13.xlsx','C:C');
Cd_O = (2*Drag_O)/(rho*u^2*A);
Cl_O = (2*Lift_O)/(rho*u^2*A);
T_O = sqrt(Drag_O.^2+Lift_O.^2);
end
%% Figure
if Figure
figure

plot(t_nond,Cd)
hold on
plot(t_12_nond,Cd_12)
hold on
```

```
plot(t_24_nond,Cd_24)
hold on
plot(t_31_nond,Cd_31)
hold on
plot(t_O_nond,Cd_O)
legend('Cd_0','Cd_{1}','Cd_{2}','Cd_{2.5}','Cd_{2.5} object')
ylim([0 3])
title('Cd')
xlabel('time_{nond}')
ylabel('Cd')
grid on
grid minor

figure

plot(t_nond,Cl)
hold on
plot(t_12_nond,Cl_12)
hold on
plot(t_24_nond,Cl_24)
hold on
plot(t_31_nond,Cl_31)
hold on
plot(t_O_nond,Cl_O)
legend('Cl_0','Cl_{1}','Cl_{2}','Cl_{2.5}','Cl_{2.5} object')
ylim([-10 1])
title('Cl')
xlabel('time_{nond}')
ylabel('Cl')
grid on
grid minor

figure

plot(t_nond,T)
hold on
plot(t_12_nond,T_12)
hold on
plot(t_24_nond,T_24)
hold on
plot(t_31_nond,T_31)
hold on
plot(t_O_nond,T_O)
legend('T_0','T_{1}','T_{2}','T_{2.5}','T_{2.5} object')
ylim([0 3000])
title('Total load')
xlabel('time_{nond}')
ylabel('T [N]')
grid on
grid minor
end

%% Filter
if Filter
    %tspan = 0.1365;
    tspan = 0.28*2;
```

```
    for i = 1:(length(t1)-1)
        diff(i) = t1(i+1)-t1(i);
    end
    M = mean(diff);
    step_size = round(tspan/M);
    step_num = round(length(t1)/step_size);
    t1fil = zeros(step_num,1);
    for i = 0 : (step_num-1)
        t1fil(i+1) = t1(1+step_size*i);
    end
    t1fil_nond = t1fil.*(u/D);
    Cd1fil = zeros(step_num,1);
    for i = 0 : (step_num-1)
        if step_size*(i+1)> length(Cd1)
           break
        end
        Cd1fil(i+1) = mean(Cd1((1+step_size*i):(step_size*(i+1)),1));
    end

    for i = 1:(length(t)-1)
        diff(i) = t(i+1)-t(i);
    end
    M = mean(diff);
    step_size = round(tspan/M);
    step_num = round(length(t)/step_size);
    tfil = zeros(step_num,1);
    for i = 0 : (step_num-1)
        tfil(i+1) = t(1+step_size*i);
    end
    tfil_nond = tfil.*(u/D);
    Cdfil = zeros(step_num,1);
    for i = 0 : (step_num-1)
        if step_size*(i+1)> length(Cd)
           break
        end
        Cdfil(i+1) = mean(Cd((1+step_size*i):(step_size*(i+1)),1));
    end

    for i = 1:(length(t3)-1)
        diff(i) = t3(i+1)-t3(i);
    end
    M = mean(diff);
    step_size = round(tspan/M);
    step_num = round(length(t3)/step_size);
    t3fil = zeros(step_num,1);
    for i = 0 : (step_num-1)
        t3fil(i+1) = t3(1+step_size*i);
    end
    t3fil_nond = t3fil.*(u/D);
    Cd3fil = zeros(step_num,1);
    for i = 0 : (step_num-1)
        if step_size*(i+1)> length(Cd3)
           break
        end
        Cd3fil(i+1) = mean(Cd3((1+step_size*i):(step_size*(i+1)),1));
    end
```

```
end
%%
figure
subplot(1,2,1)
plot(t1_nond,Cd1)
hold on
plot(t_nond,Cd)
hold on
plot(t3_nond,Cd3)
legend('Cd_1','Cd_2','Cd_3')
ylim([0 1])
xlim([0 250])
title('Cd for three grids with increasing refinement')
xlabel('time_{nond}')
ylabel('Cd')
grid on
grid minor

subplot(1,2,2)
plot(t1fil_nond,Cd1fil)
hold on
plot(tfil_nond,Cdfil)
hold on
plot(t3fil_nond,Cd3fil)
legend('Cd_1','Cd_2','Cd_3')
ylim([0 1])
xlim([0 250])
title('Filtered Cd for three grids with increasing refinement')
xlabel('time_{nond}')
ylabel('Filtered Cd')
grid on
grid minor
```

H.2. Richardson extrapolation

```
clc
clear all

N1 = 80;
D = 1;
r = 1.5;
Cd = [0.59 0.6 0.62];
p = log((Cd(length(Cd))-Cd(length(Cd)-1))/(Cd(length(Cd)-1)-Cd(length(Cd)-2)))/log(r);
Fs = 1.25;
h = zeros(size(Cd));
h(1) = (4*pi*D)/N1;
for i = 2 : length(Cd)
    h(i) = h(1)/(r^(i-1));
end
for i = 1 : length(Cd)
    H(i) = 1/(h(i)^2);
end
Cd0 = (H(1)*Cd(1)+H(2)*Cd(2)-2*H(3)*Cd(3))/(H(1)+H(2)-2*H(3));
Cd0 = ones(size(Cd))*Cd0;
```

```
for i = 1 : length(Cd)
    E(i) = Cd(i)-Cd0(i);
end

for i = 1 : (length(Cd)-1)
    epsilon(i) = (Cd(i)-Cd(i+1))/Cd(i+1);
end

K = Fs/(r^p-1);
for i = 1 : (length(Cd)-1)
    GCI(i) = K*abs(epsilon(i));
end

if abs(GCI(length(Cd)-1)-(r^p)*GCI(length(Cd)-2)) < 0.0015
    msgbox( 'Richardson extrapolation converged' );
else
    msgbox( 'Richardson extrapolation failed to converge' );
end

figure
plot(Cd)
hold on
plot(Cd0)
grid on
grid minor
ylim([0 1])
xlabel('Normalized grid spacing')
ylabel('Cd')
title('Convergence rate of three grids w.r.t. their Richardson Extrapolation')
legend('Cd values of three grids','Richardson Extrapolation')
```

I

Wind tunnel tests proposal

The wind tunnel tests, discussed here, do not include the roll motion of the vessel and the flow velocity changes around the rotor that follow from it. The tests serve to validate the CFD simulations.

The researches already performed on rotating rotors are validated and verified with results from other researches or experimental set ups. The papers that were found and that were validated with wind tunnel tests compared 2D CFD models with the wind tunnel tests without compromising for the dimensional differences. The conditions in which the rotor will be tested are important because they will quantify the level of validation. The validation occurs for the:

1. Lift and drag coefficients
2. St number
3. Velocity flow field development around and on the rotor

The following conditions are set for the wind tunnel tests. They correspond to the settings for the CFD settings and assure the right scaling.

1. Same Reynolds number, spin ratio and aspect ratio; scaling requirements
2. Laminar, uniform incoming flow; ensuring equal environmental conditions and eliminating wall effects of the tunnel
3. Dimensional equality; or compensation for that matter
4. Measurements for the balance of the model; to map the natural frequencies of the model

The rotor will be rotating in a high Reynolds number range, when the Reynolds number is to be maintained the incoming wind in the wind tunnel should be very high. For example: for a rotor with a aspect ratio of 6 and a diameter of 3 meter with an incoming wind speed of 7 m/s the wind in the tunnel should be 70 m/s, for a model scale of 1:10. There exist options to increase the Reynolds number to make the experiments more realistic. For example, the roughness of the model can be changed to increase the Re of the flow around the rotor. The scaling of the rotational speed of the model with respect to the incoming velocity results in a impossible high rpm for the model. When the wind velocity in the wind tunnel can be reduced also the rpm of the model can be reduced according to the spin ratio. Because of the expected stable behavior of the wake, at higher SR, the chance of interference between the walls of the tunnel and the model decreases. This increases the limit of the incoming flow velocity of the tunnel.

How the model will be located in the wind tunnel is important to acquire a as realistic as possible model test. If the model is placed on a flat surface the interaction of the table and the model will influence the flow around the rotor. The boundary layer of the table can be excluded by lacing the model on a non-rotating cylinder with a diameter significantly smaller than the diameter of the rotating rotor. In the supporting cylinder the electric motor that drives the rotor can be placed.

The loads measured from the model will be compared to the numerically determined loads whereby the numerical calculations can be verified. Probes can be placed in front of the cylinder in the incoming wind flow to ensure the laminar and constant profile. The wake could be depicted by PIV methods, but this is not necessary for this Reynolds number range.

One important question can be answered by performing wind tunnel tests. The assumption that the simulation cylinder has an infinite length can be *verified*. Also the chosen height of the cylinder in the simulations can be evaluated using the PIV methods. In figure **??** the proposed set ups of the wind tunnel tests are presented. The set ups are discussed from left to right:

1. The rotor is located on a smaller cylinder containing the electric motor to make the model rotate
2. Half of the rotor can be simulated with a varying cylinder height to determine the height for which the cylinder can be considered infinite long
3. The top plate is hung by the ceiling so that it does not rotate with the rotor; the end plate effects of the rotor can then be evaluated

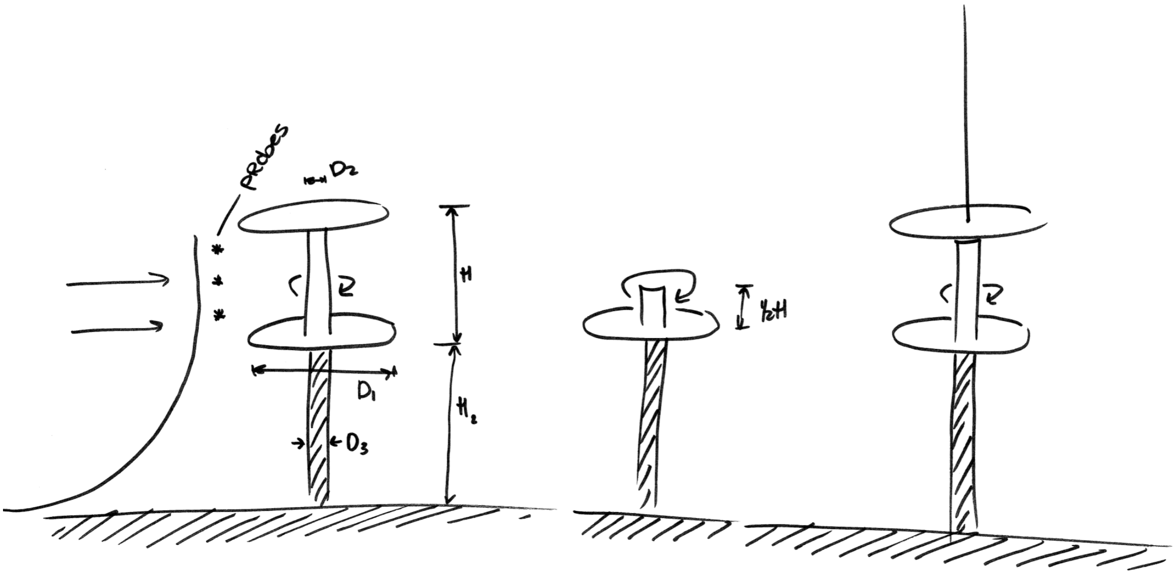

Figure I.1: Set up of the different models for the wind tunnel tests.

J
Legends

In this appendix the legends are presented that correspond to the figures in chapter 7.

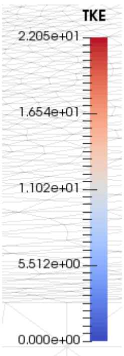

Figure J.1: Legend belonging to figure 7.21 upto 7.25, figure 7.39, figure 7.40, figure 7.41, figure 7.53 upto figure 7.56,figure 7.59 upto figure 7.62, figure 7.71 upto figure 7.75 and figure 7.89 upto figure 7.98 representing the Turbulent Kinetic Energy (TKE) in $\frac{m^2}{s^2}$.

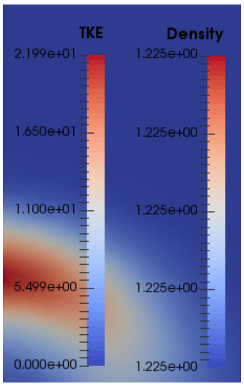

Figure J.2: Legend belonging to figure 7.20, figure 7.38 and figure 7.58 representing the Turbulent Kinetic Energy (TKE) in $\frac{m^2}{s^2}$ and its density.

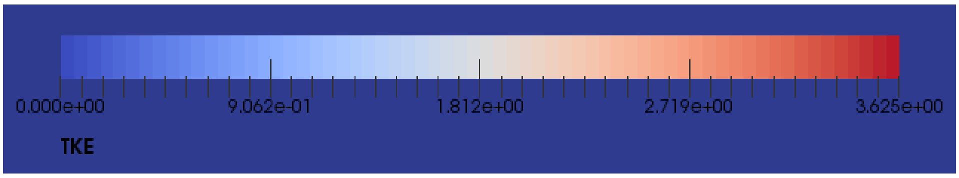

Figure J.3: Legend belonging to figure 7.27 upto 7.29 representing the Turbulent Kinetic Energy (TKE) in $\frac{m^2}{s^2}$.

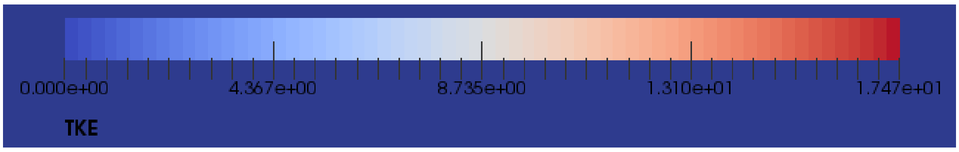

Figure J.4: Legend belonging to figure 7.32 upto 7.37 representing the Turbulent Kinetic Energy (TKE) in $\frac{m^2}{s^2}$.

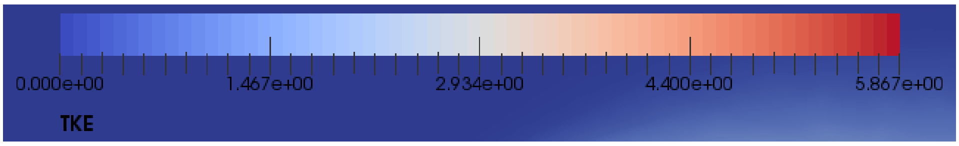

Figure J.5: Legend belonging to figure 7.43 upto 7.52 representing the Turbulent Kinetic Energy (TKE) in $\frac{m^2}{s^2}$.

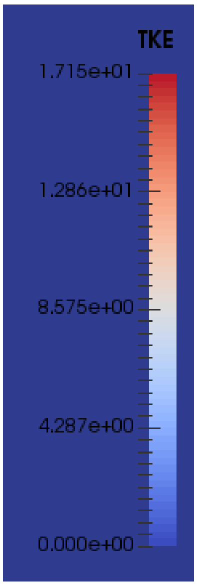

Figure J.6: Legend belonging to figure 7.85 upto 7.86 representing the Turbulent Kinetic Energy (TKE) in $\frac{m^2}{s^2}$.

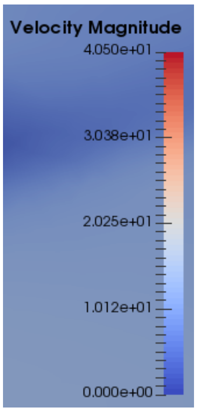

Figure J.7: Legend belonging to figure 7.79 upto 7.84, figure 7.87 and figure 7.88 representing the flow velocity in $\frac{m}{s}$.

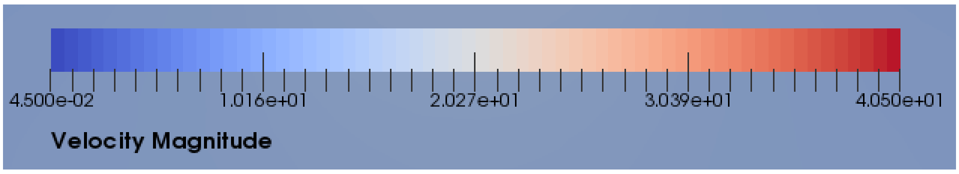

Figure J.8: Legend belonging to figure 7.99 upto 7.118 representing the flow velocity in $\frac{m}{s}$.

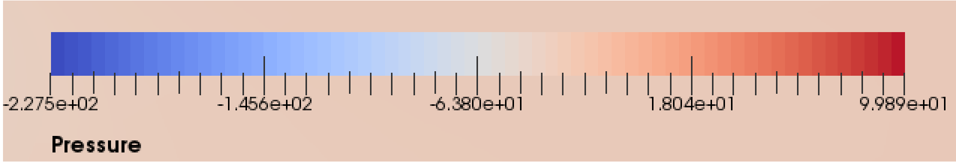

Figure J.9: Legend belonging to figure 7.119 upto 7.126 representing the Pressure in $\frac{N}{m^2}$.

Bibliography

[1] Cruise market watch. `http://www.cruisemarketwatch.com/growth/`, 01 2017.

[2] C. Badalamenti and S. A. Prince, editors. *The effects of endplates on a rotating cylinder in crossflow*, 2008. AIAA-7063.

[3] J Boussinesq. Essai sur la theorie des eaux courantes. *Memoires presentes par divers savants a l'Academie des Sciences*, 23(1):1–680, 1877.

[4] M. Breuer. A challenging test case for large eddy simulation: high reynolds number circular cylinder flow. *International Journal of Heat and Fluid Flow*, (21):648–654, 200.

[5] P. Catalano, M. Wang, G. Iaccarino, and P. Moin. Numerical simulation of the flow around a circular cylinder at high reynolds numbers. *International Journal of Heat and Fluid Flow*, (24):463–469, 2003.

[6] I.B. Celik, P.J. Ghia, U. Roache, H. Freitas, H. Coleman, and E. Raad. Procedure for estimation and reporting of uncertainty due to discretization in cfd applications. *Journal of Fluids Engineering*, 2008.

[7] Enercon Wind Company. Enercon e-ship 1: a wind-hybrid commercial cargo ship. *Proceedings of the 4th Conference on Ship Efficiency*, September 2013.

[8] R. Cosner, W. L. Oberkampf, C.L. Rumsey, C. Rahaim, and T. Shih. Aiaa committee on standards for computational fluid dynamics: status and plans. *AIAA journal*, 2006.

[9] Tim Craft, Nick Johnson, and Brian Launder. Back to the future? a re-examination of the aerodynamics of flettner-thom rotors for maritime propulsion. *Springer Science+Business Media Dordrecht 2013*, 2012.

[10] T.J. Craft, N.Z. Ince, and B.E. Launder. Recent developments in second-moment closure for buouancy-affected flows. *Dynamic Armos. Oceans*, 23:99–114, 1996.

[11] A. De Marco, S. Mancini, and C. Pensa. Preliminary analysis for marine application of flettner rotors. *Yildiz Technical University*, 2014.

[12] A. De Marco, S. Mancini, C. Pensa, G. Calise, and F. De Luca. Flettner rotor concept for marine applications: A systematic study. *International Journal of Rotating Machinery*, Volume 2016(3458750):12, 2016.

[13] *Motion control of a cruise ship by using active stabilizing fins*, volume 225, Seoul, Republic of Korea, 2011. Department of Naval Architecture and Ocean Engineering, Seoul National University, IMechE.

[14] *SESAM User Manual Wadam*. Det Norske Veritas, 8.1 edition, 01 2917.

[15] DNV. Environmental conditions and environmental loads. *DNV-RP-C205l*, 2010.

[16] J. Gerritsma. *Scheepsbewegingen, sturen en manoeuvreren*. TU Delft, Werktuigboukunde en Maritieme Techniek sectie Scheepshydromechanica, 1979.

[17] J. Gerritsma. *Golven*. TU Delft, Werktuigboukunde en Maritieme Techniek sectie Scheepshydromechanica, 1979.

[18] M. Greco. Correlation length of vortex shedding, lecure 10 notes. PowerPoint, 2013.

[19] R. A. Ibrahim and I. M. Grace. Modeling of ship roll dynamics and its coupling with heave and pitch. *Mathematical Problems in Engineering*, 2010.

[20] Y. Ikeda, Y. Himeno, and N. Tanaka. Ship roll damping-frictional component and normal pressure on bilge keel. *Journal of the Kansai Society of Naval Architects*, 161, 1976.

[21] N.D. Johnson. High-reynolds-number flow past a rotating cylinder with and without thom discs. Master's thesis, Faculty of Engineering & Physical Sciences, The University of Manchester, 2011.

[22] J.M.J. Journee and W.W. Massie. *Offshore Hydromechanics*. Delft University of Technology, Delft, Netherlands, 2001.

[23] S.J. Karabelas. Large-eddy simulation of turbulent flow past a rotating cylinder. *International Journal of Heat and Fluid Flow*, 31:518–527, 2010.

[24] S.J. Karabelas, B.C. Koumroglou, C.D. Argyropoulos, and N.C. Markatos. High reynolds number turbulent flow past a rotating cylinder. *Computational Fluid Dynamics Unit, School of Chemical Engineering, National Technical University of Athens*, 2012.

[25] Kern E. Kenyon. On the magnus effect. *Natural Science*, 8:49–52, Feb 2016.

[26] A.N. Kolmogorov. The local structure of turbulence in incompressible viscous fluids at ver large reynolds numbers. *Doklady*, 30:2299–393, 1941.

[27] L. Larsson. *Ship Resistance and Flow*. Society of Naval Architects and Marine Engineers, 2011.

[28] J. Latham, K. Bower, T. Choularton, H. Coe, P. Connelly, G. Cooper, T. Craft, J. Foster, A. Gadian, L. Galbraith, H. Lacovides, D. Johnston, B. Launder, B. Leslie, J. Meyer, A. Neukermans, B. Ormond, B. Parkes, P. Rasch, J. Rush, S. Salter, T. Stevenson, H. Wang, Q. Wang, and R. Wood. Marine could brightening. *Philosophical Transactions of the Royal Society A Mathematical Physical and Engineering Sciences*, September 2012.

[29] K. C. Morisseau. Marine application of magnus effect devices. *Navel Engineers Journal*, vol. 97(no. 1):pp. 51–57, 1985.

[30] F. Moukalled, L. Mangani, and M. Darwish. *The Finite Volume Method in Computational Fluid Dynamics*. Springer International Publishing Switserland, 2016.

[31] C. Moussaed, M. V. Salvetti, S. Wornom, B. Koobus, and A. Dervieux. Simulation of the flow past a circular cylinder in the supercritical regimne by blending rans and variational-multiscale les models. *Journal of Fluid and Structures*, 2014.

[32] D. Nelissen, M. Traut, J. Kohler, W. Mao, J. Faber, and S. Ahdour. Figting the windbreak. *The Naval Architect*, May 2017.

[33] G. V. Papaioannou, D. K. Yue, M. S. Triantafyllou, and G. E. Karniadakis. Three dimensionality effects in flow around two tandem cylinders. *Journal of Fluid Mechanics*, pages 558:387–413, 2006.

[34] D. R. Pearson. The use of flettner rotors in efficient ship design. *Influence of EEDI on Ship Design*, September 2014.

[35] L. Prandtl. The magnus effect and wind-powered ships. *Naturwissenschaften*, vol 13:pp. 1787–1806, 1925.

[36] P.J. Roache. *Verification and validation in computational science and engineering*. Hermosa Publishers, 1998.

[37] S. P. Singh and S. Mittal. Flow past a cylinder: shear layer instability and drag crisis. *International Journal of Numerical Methods Fluids*, (47):75–98, 2005.

[38] S. Speares. Everything's gone green. *The Naval Architect*, pages 60–61, May 2017.

[39] F. Stern, R.V. Wilson, H.W. Coleman, and E.G. Paterson. Comprehensive approach to verification and validation of cfd simulations - part1: Methodology and proceduers. *ASME J. Fluids Eng*, Vol. 123(No. 4): pp. 793–802, 2001.

[40] T.F. Sun, D.X. Gu, Z.F. adn He, and L.L. Zhang. Fluctuating pressure on two circular cylinders at high reynolds numbers. *Hounal of Wind Engineering and Industrial Aerodynamics*, 41-44:577–588, 1992.

[41] Metin Taylan. Nonlinear roll motion of ships in beam waves. *Bull. Tech. Univ. Instanbul*, 49:459–479, 1996.

[42] A. Thom. Effects of disc on the air forces on a rotating cylinder. *Aeronautical Research Committee*, Reports & Memoranda(1623), 1934.

[43] Ulstein. Cruise. `https://ulstein.com/ship-design/cruise`, 2017.

[44] F. M. White. *Viscous Fluid Flow.* McGraw-Hill, 3 edition, 2006.

[45] C.H.K. Williamson. Vortex dynamics in the cylinder wake. *Annual Review of the Fluid Mechanics*, 28: 477–539, 1996.

[46] W. Zhang, R.E. Bensow, M. Golubev, and V. Chernoray. Flow past a rotating finite length cylinder: numerical and experimental study. Technical report, Chalmers University of Technology, 2016.